國立臺灣大學電機資訊學院光電工程學研究所

碩士論文

Graduate Institute of Photonics and Optoelectronics

College of Electrical Engineering and Computer Science

National Taiwan University

Master Thesis

利用三維等效侷域量子位能模型分析合金擾動和應力對深紫外光發光二極體的影響

The optimization and analysis of UVC-LEDs by considering strain-induced deformation potential and random alloy fluctuation with the localization landscape model

張雨倢

Yu-Chieh Chang

指導教授: 吳育任 博士

Advisor: Yuh-Renn Wu Ph.D.

中華民國 112 年 8 月

August, 2023

doi:10.6342/NTU202303083

doi:10.6342/NTU202303083

Acknowledgements

在我的求學路上，我是幸運的，受到了許多的幫助，其中包含了: 老師們的無私奉獻，讓學生能站在巨人們的肩膀上不至於被無涯的學海給衝倒，雖然有了更高的起點，但望不盡的風景讓我對前人的貢獻感到敬畏，而不自滿; 同儕們的幫助使我心存感激，也勉勵自己做個溫暖的人，同儕們討論及分享學習資訊，得以共同學習一同進步，使我在學習路上不孤單; 家人們的支持使我在迷茫時，有個錨點而不迷失自我。

在我碩士求學期間，我最感謝的是吳育任教授，即便教授因為接了許多計畫及接任所長而十分繁忙，但仍然願意每周撥空給學生們去詢問研究上的問題及關心學生們的研究近況，也因為與教授有許多溝通及討論的機會，所以研究得以順利進行，並且在交談的過程及思路的發想都是值得學生去學習的。其中印象深刻的是: 教授鼓勵及願意支助學生們參與研討會的心，在給予學生機會歷練及增廣見聞的同時，也能拓展知識的深廣度。

最後，感謝科技部計畫編號 109-2627-H-028-004-, 108-2628-E-002-010-MY3, 110-2923-E-002-002-, 111-2923-E-002-009-, 111-2221-E-002-075; 新國科會計畫編號 112-2923-E-002-002-; 中山科學研究院計畫編號 NCSIST-ACOM-111-6712002 經費的支持薪資以及研究支出。

doi:10.6342/NTU202303083

摘要

此研究使用了包含應力變形的等效侷域量子位能模型。此模型是藉由省略 k·p 方法中的非矩陣對角位置貢獻，來減少計算所需時間，並達到在等效侷域量子位能模型中，考慮 k·p 方法中應力對不同價帶造成的影響之目的，因此可分別解出不同價帶的位能。此模型藉由價帶與不同導帶間的自發放光來算出橫向電場極化光、橫向磁場極化光及其極化比。本文藉由比較極化比之結果及趨勢說明: 在使用應力變形的等效侷域量子位能模型後，由於多能帶位置已取得，且模擬上的極化比趨勢相近。因此，傳統上拿來計算多能帶位置及波函數的 k·p 方法可以被省略。包含應力變形的等效侷域量子位能模型在省略 k·p 方法之下計算出的極化比可被快速估計且模擬結果具有可信度。所以，本研究在優化結構時是在省略 k·p 方法計算下，使用包含應力變形的等效侷域量子位能模型。此外，在此研究的模擬結構下每步疊代可以省略大約 47 小時的時間。

在多量子井結構之深紫外線發光二極體的模擬上，由於高鋁情況下，氮化鋁鎵的電洞活化能高，在深紫外線發光波段，高鋁材料摻雜後的低電洞注入和高阻抗下注入的電洞流低，都將是導致內部量子效率下降的重要因素。此外，在低電洞注入下的高電子溢流情況也將使得內部量子效率進一步下降，因此本研究藉由 3D 模擬來優化量子能障結構及 p 型氮化鋁鎵來改善電洞注入以期達到降低電子溢流情形，並分析隨機合金擾動及應力造成的能帶變形如何對載子阻擋能力造成影響。

doi:10.6342/NTU202303083

關鍵字：深紫外光發光二極體、等效侷域量子位能模型、磊晶層優化、應力變形、三維、隨機合金擾動

doi:10.6342/NTU202303083

Abstract

This study uses the strain-induced deform potential localization landscape(LL) model to do the simulation. To consider the strain effects, we applied the stain-induced deformation potential shift from the k·p equations into the LL model and solved different valence band states separately. It ignores the influences of the off-diagonal term in the k·p model and tries to accelerate the calculation of device results. With the model, the multi-band position corresponding to the different states will be obtained. According to the spontaneous light emission from the electron and the hole in different states, the transverse electronic (TM) polarized light, transverse magnetic (TE) polarized light, and the polarization ratio (PR) will be calculated. The comparison of the polarization ratio between the modified LL model and the k·p model shows a similar trend, which can be used to estimate the polarization ratio quickly. We only need to use the modified LL model for the optimized structures to obtain the final results. In addition, after removing the k·p method calculation, the calculation time will save around 47 hours per iteration under the simulation

doi:10.6342/NTU202303083

structure of this work.

For the UVC multiple quantum well simulation, due to the high activation energy in AlGaN with high Al, the low activated hole density and high resistance of hole current in the p-type AlGaN layer is a critical reason for the low internal quantum efficiency in UVC-LEDs. The severe electron carrier overflow under the low hole injection will further reduce the internal quantum efficiency. Hence, this study tries to reduce the electron carrier overflow by optimizing the structure of quantum barriers and the p-AlGaN layer with the 3D simulation method considering Al random alloy fluctuation. Then, the influence of random alloy fluctuation and the strain-induced band structure deformation will be analyzed and the optimized structure to improve the carrier-blocking ability will be discussed in this paper.

Keywords: UVC-LEDs, localization landscape model, Optimized epitaxial layer, strain deformation, 3D, Random alloy fluctuation

doi:10.6342/NTU202303083

Contents

doi:10.6342/NTU202303083

doi:10.6342/NTU202303083

doi:10.6342/NTU202303083

doi:10.6342/NTU202303083

List of Figures

doi:10.6342/NTU202303083

doi:10.6342/NTU202303083

doi:10.6342/NTU202303083

doi:10.6342/NTU202303083

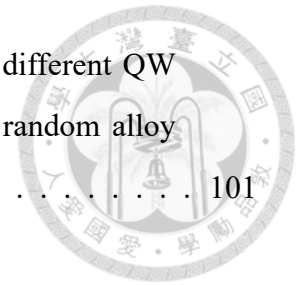

doi:10.6342/NTU202303083

doi:10.6342/NTU202303083

List of Tables

doi:10.6342/NTU202303083

doi:10.6342/NTU202303083

Chapter 1 Introduction

1.1 Motivation

The study of group III-nitride-based ultraviolet light-emitting diode (UV-LEDs) is a popular field. To save energy and achieve high power density, the efficiency needs to be improved.[2] The adjustable wide band gap leads to the wide application in the AlGaN material. For traditional mercury lamps, the Hg atoms are the critical factor for the emission of UV wavelength by the collision of an accelerated electron and Hg atoms. It is important to note that incorrectly dealing with mercury will cause environmental pollution and many toxic effects on the human body.[3, 4] On the other hand, UV-LEDs are more environmentally friendly in UV emission wavelength than the traditional mercury lamp. However, due to the high-cost price and the low external quantum efficiency (EQE) problem, the traditional mercury lamp remains mainstream in the current market.

For III-nitride-based UV-LEDs, the adjustable emission wavelength from 400 nm to 200 nm allows engineers to design different wavelengths UV-LEDs for different applications. The UV-LEDs can be sorted into UVC, UVB, and UVA by the emission wavelength. The emission wavelengths in 100 nm to 280 nm, 280 nm to 315 nm, and 315 nm to 400 nm are UVC, UVB, and UVA, respectively. There have some applications in different emission wavelengths of UV-LEDs shown below. In UVC-LEDs, Water or air purifica-

doi:10.6342/NTU202303083

tion products, which kill bacteria, microbes, and viruses, have been an important factor, especially during the Covid-19 pandemic. In UVB-LEDs, Phototherapy in medicine can help people to treat some of the skin diseases induced by the immune system. Some studies [5, 6] show that UVB light is the critical factor for the plant to produce secondary metabolites, which have related to lowering some of the diseases happening. Therefore, by controlling the UVB light-emitting to the plant, the growth of shape and secondary metabolites could be manipulated. On the other hand, the UVB-light has plant growth lighting ability. In UVA-LEDs, UV curing of material is an essential step in some of the processes. Gas sensing products could detect harmful gas concentrations in the environment and alteration. Furthermore, UV light can be the absorption light source for the fluorescence material to excite the fluorescence emission. The absorption spectrum peak of O_3, SO_2, and NO_2 is around 255 nm, 285 nm, and 404 nm, and the gas sensing of UV-LEDs is well-applied in O_3, SO_2, and NO_2. [3, 4, 7, 8]

In the emission wavelength of 100 nm to 280 nm, the UV-LEDs can be called UVC-LEDs. As we mentioned above, water purification is the application of UVC-LEDs, due to the bacteria, microbes, and viruses will be killed by the bond of DNA or RNA breaking after absorbing the UVC light. Also, the UVC-LEDs with 220 nm to 230 nm are becoming important because they are less harmful to the human skin.[8] This work will focus on 225 nm and 253 nm multiple quantum well (MQW) UVC-LEDs. Additionally, to improve the electron carrier blocking ability in UVC-LEDs, we will optimize the design by changing the composition in the quantum barrier (QB) and electron blocking layer (EBL), then analyzing their performance.

doi:10.6342/NTU202303083

1.2 The issue of low quantum efficiency in UVC-LEDs

This section will talk about the low quantum efficiency problems in UVC-LEDs by the impact factor of external quantum efficiency (EQE), which include the light extraction efficiency (LEE) and the internal quantum efficiency (IQE). Their relation is in Eq. (1.1).

$$\mathrm{EQE} = \mathrm{IQE} \times \mathrm{LEE} \tag{1.1}$$

The IQE in AlGaN-based MQW UVC-LEDs is low due to the problem of hole injection and electron overflow. Then, the issue of the low hole carrier injection and the electron carrier overflow in AlGaN-based UVC-LEDs will introduce afterward.

The high ionization energy of the Mg acceptor in the AlGaN layer leads to low hole density and high sheet resistance in the p-AlGaN layer, especially in the UVC emission range.[2, 9] However, the activation energy for high Al alloy is quite large, so generating the hole carrier in the p-AlGaN layer is hard. Furthermore, due to the high resistivity and the activation energy in the p-AlGaN layer, the electron carrier will accumulate and cause the current crowding effect. Finally, they will induce the joule heating effect and the un-uniform extraction light.[10] Furthermore, the element's lifetime will decrease. There are some studies about the improvement of hole carrier injection, such as improved hole carrier injection by the tunneling junction design between the GaN-cap and QB layer. Still, the operating voltage under 20 (mA) will increase enormously.[11] The magnesium delta-doped in the last QB.[12] The p-GaN to metal's ohmic contact, which could help the hole carrier injection by the low contact resistance.[10, 13] The design of the p-AlGaN gradual layer could help the hole carrier injection by releasing the strain between the QB

doi:10.6342/NTU202303083

and top layer.[14] The p-AlGaN with high Al not only has the low hole injection problem but also has different types of defects, during growth. The defect will limit the doping concentration in the AlGaN layer, especially in the growth of the high Al composition layer.[3]

Generally, the electron carrier overflow problem will be more severe in the smaller emission wavelength cases. Due to the higher activation energy's acceptor will lower the injection of hole carrier density to the active region. The hole carriers, which have the smaller mobility, are not sufficient to recombine with the electrons.[9] If the barrier can not block the electron carrier, the overflowing electron will recombine at the p-AlGaN layer and cause the leakage current.[9, 13] Therefore, the droop effect will decrease the radiative recombination efficiency by the severe carrier overflow when the by current density increases. The design of the electron blocking layer could efficiently reduce the electron carrier to overflow.

From the light extraction efficiency (LEE) perspective, the light absorption and the propagation direction of light emission are important factors.

Following are some designs that drop the light extraction efficiency (LEE) by light absorption. As mentioned, the p-GaN to metal's ohmic contact could help the hole carrier injection. However, the GaN material has a smaller band gap than the AlGaN active region so that the GaN top layer will absorb the light emission. In addition, the design of the p-AlGaN gradual layer will also absorb the emission light for the same reason. Due to the smaller emission wavelength in UVC-LEDs, the choice of packaging material with less absorption of the emission light and a high reflective index material to decrease the light absorption is hard to find.[13]

doi:10.6342/NTU202303083

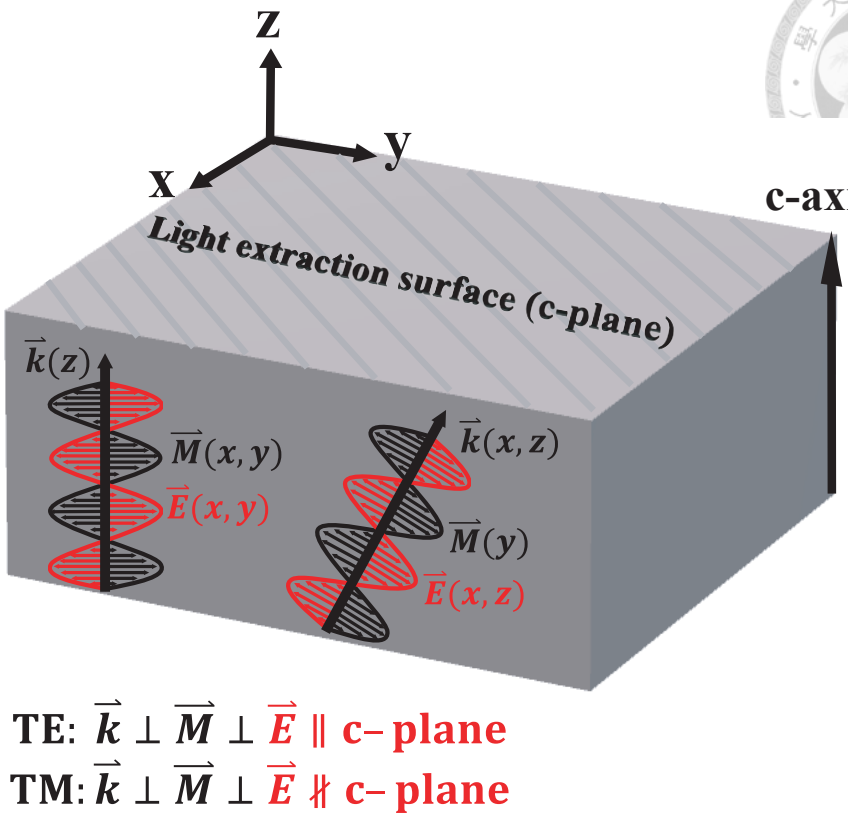

Figure 1.1: The schematic diagram of propagation direction in TE and TM light emission.

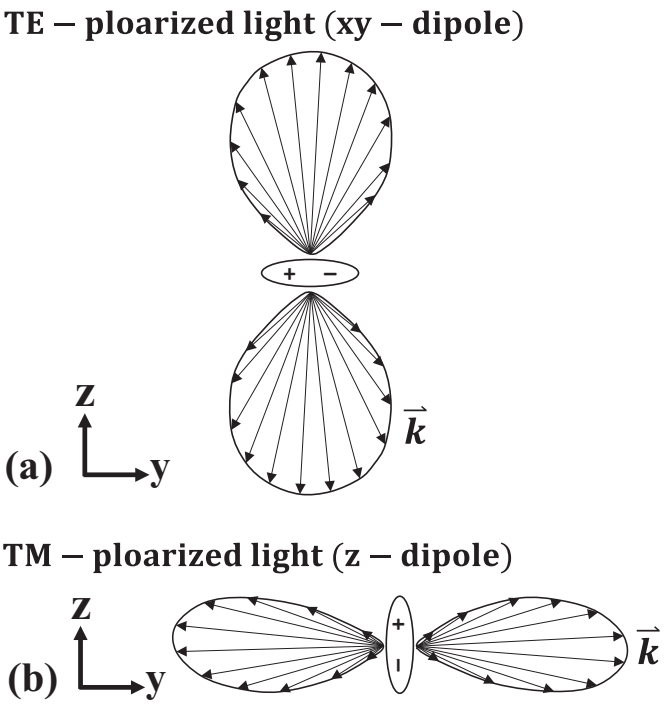

Figure 1.2: (a) and (b) are the radiation pattern of TE- and TM-polarized light[1].

For the wurtzite III-nitride crystal, the crystal orientation will cause anisotropic po-

doi:10.6342/NTU202303083

larization.[15–17] If the design of AlGaN epitaxial growth in the z-direction is parallel to the c-axis of the wurtzite structure, and the design of the top surface for light extraction is perpendicular to the c-axis (z-direction). Therefore, the c-plane surface is the light extraction surface.

According to the definition of transverse electric (TE) and transverse magnetic (TM) waves, the electric polarization parallel to the light extraction surface plane (c-plane surface) is the TE wave. On the other hand, the electric polarization for the TM wave has the component in the c-axis direction. Based on the traditional design for increasing the light extraction, such as the c-plane surface, pattern substrate, surface roughness, etc.[18] Given light extraction efficiency (LEE), the TE wave will be better than the TM wave.[19, 20]

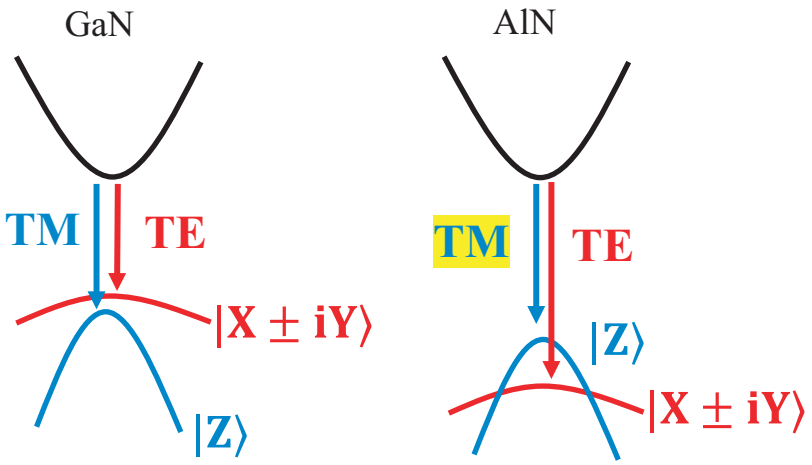

Figure 1.3: The band structure schematic diagram of GaN and AlN material.

Above have introduced the direction of the c-axis, the polarization direction of TE and TM waves, and the concept of light extraction under some assumptions. The connection between interband light emission and light extraction will be discussed afterward.

Before introducing the transition mechanism, the bands for electrons and holes transition must be clearly defined first. The minimum band of the conduction band (CB) is

doi:10.6342/NTU202303083

usually the s-orbital state dominant band. However, the valance band is more complex because the maximum valance band is usually the p-orbital state. Additionally, the p-orbital state can be sorted into six states and named the band by its dominant state. Such as the valance band dominated by the $|X + iY, \uparrow\rangle$ or $|X - iY, \downarrow\rangle$ state is CH1 band; the valance band dominated by the $|X + iY, \downarrow\rangle$ or $|X - iY, \uparrow\rangle$ state is CH2 band; the valance band dominated by the $|Z, \downarrow\rangle$ or $|Z, \uparrow\rangle$ state will be abbreviated to the split-off (SO) valence band or CH3 band.

In the interband optical momentum matrix elements for wurtzite GaN-based crystal, the response of the band edge transition in the conduction band to the CH1 band (C-CH1) and the conduction band to the CH2 band (C-CH2) have the nonzero interband momentum-matrix elements in x and y direction and zero terms in the z-direction. The conduction band to the CH3 band (C-CH3) transition has the nonzero interband momentum-matrix elements in the z-direction.

Based on the spontaneous emission rate can calculate by the integration of the interband momentum-matrix element in the x, y, and z directions.[21] The zero interband momentum-matrix element in the z-direction means the electric polarization in the z-direction has the zero term. Namely, the electric polarization for the C-CH1 band and the C-CH2 band transition is in the x and y direction. The propagation direction of it is the z-direction due to the orthogonal property in transverse electromagnetic (TEM) waves. Put differently, the C-CH3 band transition has electric polarization in the z-direction. [15, 22]

Based on the assumption above, the c-axis is in the z-direction, and the c-plane is the x-y plane. The C-CH1 and C-CH2 band transition will emit the TE-polarized light emission, and the C-CH3 band transition will emit the TM-polarized light emission. In

doi:10.6342/NTU202303083

brief, the TE-polarized light, generate from C-CH1 and C-CH2 band transition, is better for the light extraction design.

However, in AlGaN-based UVC-LEDs, decreasing the emission wavelength by increasing the Al composition in the active region will let the dominant valance band become the split-off band (CH3). When the emission wavelength is smaller than 270 nm.[23] due to the larger crystal field split-off energy in AlN material (Δ_1=−0.169), the |Z> band will become the dominated ground state band and lead to the TM emission. [18]. Therefore, the increasing TM-polarized light will lower the light extraction efficiency (LEE) because the incident angle to the c-plane surface is large, which makes the total internal reflection too strong in the UVC-LEDs system. In conclusion, AlGaN-based MQW UVC-LEDs have a light extraction problem. [23–26]

1.3 Random alloy fluctuation

Due to the crystal orientation in wurtzite GaN-based crystal[15–17], when the strain is applied, the piezoelectric and the spontaneous polarization cause band bending will strongly influence the GaN-based LEDs, such as the decreasing overlap of electron and hole wave function, the emission wavelength redshift, the IQE decrease, etc.[27, 28]

The random alloy fluctuation in the composition will lead to potential fluctuation. From the potential barrier fluctuation, the carrier could cross the potential barrier by the percolation path. Namely, the potential barrier effectively decreased. Therefore, the carrier transport will improve under the random alloy fluctuation when discussing the vertical transport through the barrier, and the operation voltage will decrease.[29, 30] For the potential fluctuation in quantum well (QW) with the lateral direction, the influence of the

doi:10.6342/NTU202303083

random alloy fluctuation in the lateral plane will localize the carrier at a relatively low potential position in the QW region. The carrier could avoid accumulating at the bending edge and increase the wave function overlap. However, it also limits the carrier spreading in the QW. The influence of the decreasing wave function overlap and wavelength red-shift from the quantum confinement stack effect (QCSE) will decrease by the random alloy fluctuation.[27] Due to the improving wave function overlap, the IQE will increase. Furthermore, carrier localization caused by potential fluctuation will decrease the diffusion length. It will reduce the nonradiative recombination from the sidewall defect for small chip size conditions (μ-LED) or defect centers.[2] The Auger recombination efficiency will increase by the carriers confined in the small localized region.[29, 30]

The study shows that the under the random alloy fluctuation, the polarization ratio is larger than without considering the random alloy fluctuation cases. To do the simulation precisely, considering random alloy fluctuation is essential. The details of how to simulate the random alloy fluctuation are in Chapter 2.

doi:10.6342/NTU202303083

1.4 The deformation potential is induced by strain

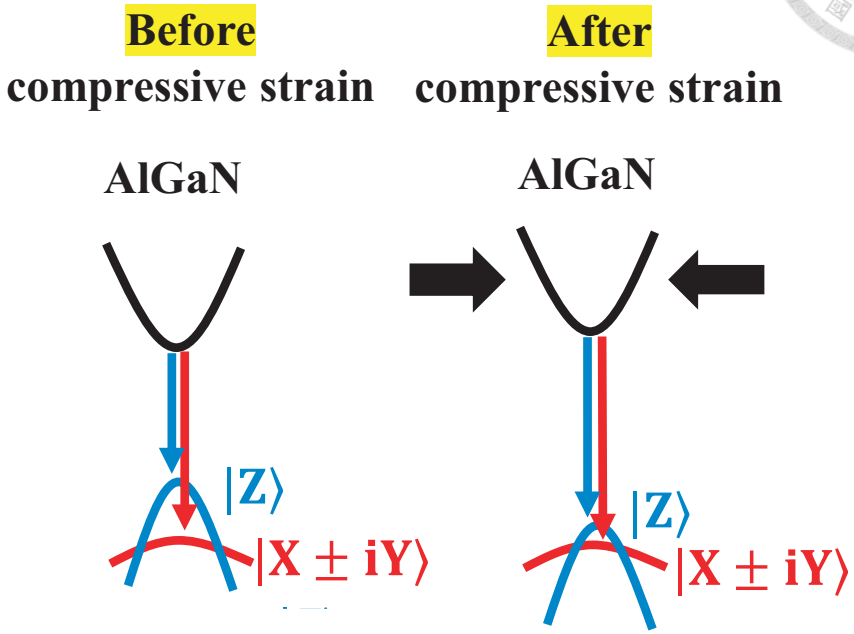

Figure 1.4: The E-k diagram of AlGaN material before and after considering the compressive strain in AlGaN with high Al.

Owing to the hydrostatic energy shift will occur in the presence of strain inhomogeneity. [31] For an anisotropic GaN-based wurtzite structure, the hydrostatic deformation potential will change the band gap when the strain is applied. Furthermore, based on the deformation theory, the potential perturbation will change the valance band. [32] Due to the relative position of atoms will change by the stress, the strain-caused band structure deformation could calculate by the deformation potential theory.

In 220∼250 nm, the Al composition in AlGaN is high. Due to the crystal field split-off energy being negative and much smaller in AlN material, the dominant valance band will be the $|Z\rangle$ state dominant band when increasing the Al composition.[18] After considering the compressive strain, the $|X \pm iY\rangle$ and $|Z\rangle$ state dominant band will decrease in electron energy.[23] The formula of 3-band's deformation potential induced by strain

doi:10.6342/NTU202303083

will be introduced in Chapter 2.5.4 and discussed in Chapter 5.2.2.

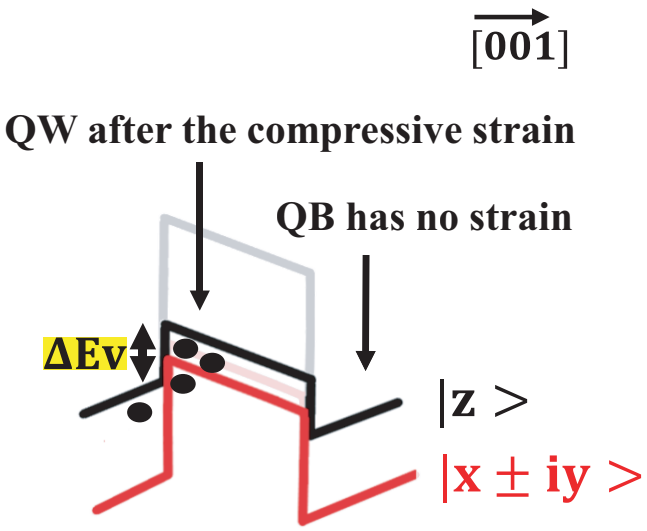

Figure 1.5: The band structure of AlGaN QW after considering the compressive strain in AlGaN with high Al composition.

In this study, due to the Al composition in the buffer layer (AlGaN transition buffer layer, n-AlGaN contact layer, n-AlGaN layer, and the QBs are the same, see Fig. 3.1). The strain in QWs is compressive, and the QB has no strain. After considering the compressive strain in QWs, whether the difference of the dominant valance band (ΔE_v) or the conduction band (ΔE_c) will reduce under the high Al AlGaN MQW region. [23] Additionally, detailed information on how the strain is applied to the QWs by the simulation structure design is in Chapter 3.1

1.5 Thesis overview

Chapter 2 contains detailed information on the simulation method in this study. This section talks about the simulation of random alloy fluctuation generated by the random seeding number generator and doing the Gaussian weighting in their atomic grid. Also, the

doi:10.6342/NTU202303083

derivation of the localization landscape (LL) model will be introduced before the strain-induced deformation potential LL model. In brief, under the effective mass approximation, the six states Hamiltonian question will be simplified to be the 3-band formula by ignoring the interaction terms of different states. Moreover, the parameter of the k·p method can be used to calculate the mass used in the strain-induced deformation potential LL model. Then, the critical points in this section include how we build the strain-induced deformation potential LL model and the difference between the LL model with and without considering the strain-caused deformation in the band structure.

In Chapter 3, this study's simulation parameter and structure will show here. The comparison and analysis of the polarization ratio solved by the strain-induced deformation potential LL model with and without the k·p method will be after that. The result tells that the strain-induced deformation potential LL model without the k·p method is time efficient. Therefore, the following discussion in Chapter 4 and Chapter 5 will use the strain-induced deformation potential LL model result to do the analysis.

In Chapter 4, this work will optimize the epitaxial layers of QBs and the p-AlGaN layer to decrease the electron carrier overflow by improving the hole injection efficiency between the p-GaN layer to the QW. The influences of the electron block layer will be discussed.

In Chapter 5, we will discuss the two impact factors of the carrier-blocking ability. One is the random alloy fluctuation, and the other is the strain-induced deformation potential.

doi:10.6342/NTU202303083

Chapter 2 Methodology

2.1 Overview of the simulation flow

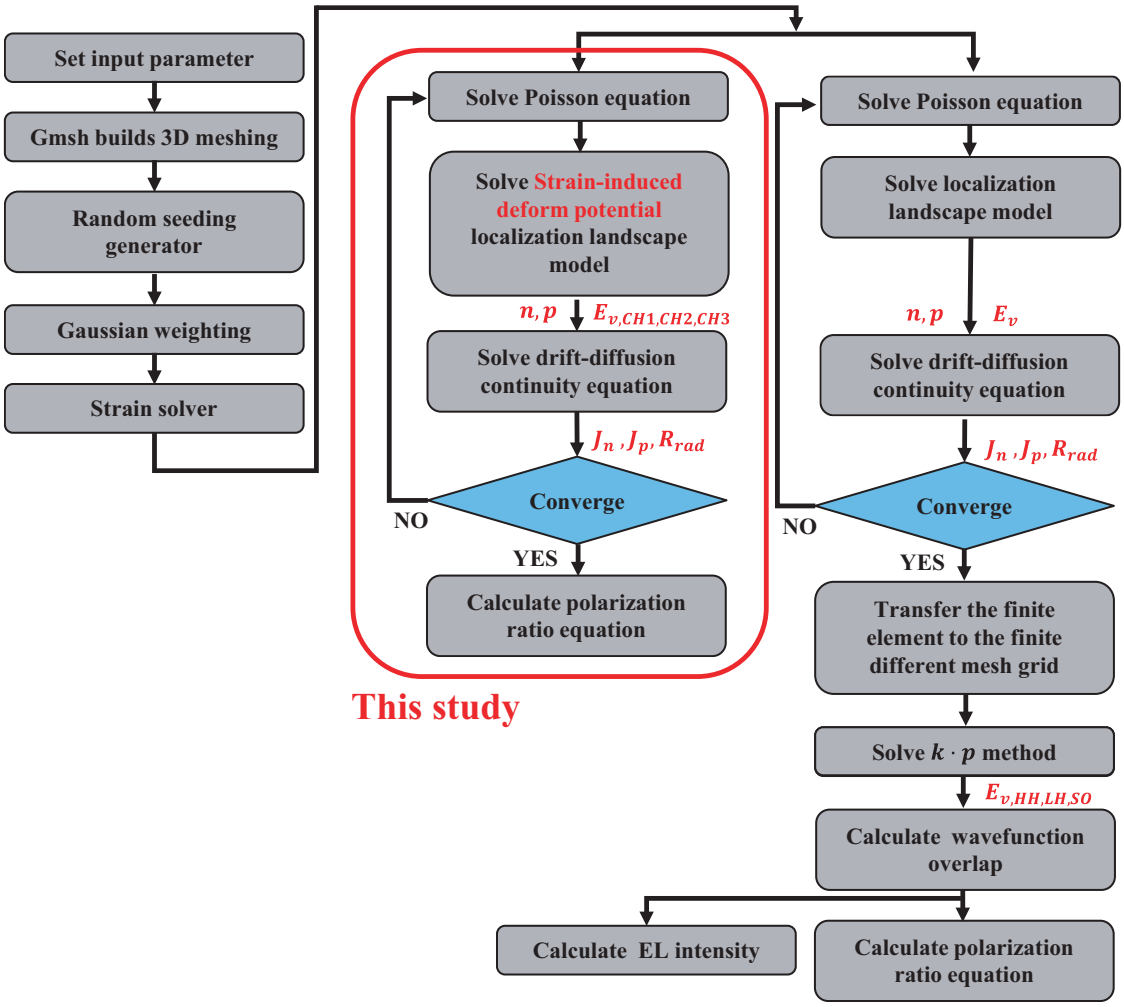

Figure 2.1: The simulation flow chart in this study.

doi:10.6342/NTU202303083

This study simulates the AlGaN UVC-LEDs by considering the random alloy fluctuation in a three-dimensional structure. First, this work uses GMSH[33], an open-source 3D finite element mesh generator, to build the three-dimensional structure. To generate the composition map with random alloy fluctuation, we used the additional function of a random seeding generator to output the random alloy fluctuation model. Due to the Gaussian weighting calculation, the composition distribution can arrange like the experimental seen Gaussian envelope shape.[34] After using the strain solver, the strain and piezoelectric charge under the random alloy fluctuation model can get. This work uses the Poisson, and drift-diffusion continuity equation with the LL model, including the strain-induced deformation potential, self-consistent to do the simulation. Until it is convergence, the information will be output for multi-bands (which are dominated by the $|X+iY,\uparrow\rangle$, $|X-iY,\downarrow\rangle$, $|X+iY,\downarrow\rangle$, $|X-iY,\uparrow\rangle$, $|Z,\uparrow\rangle$, and $|Z,\downarrow\rangle$ states), conduction band, Fermi-level, current density, carrier density and so on. Based on the traditional k·p method used to calculate the three-band position induced by strain.[17, 22, 35–39] However, the modified LL model has already considered and output the strain-induced three-band position.

Hence, this study proves that after removing the k·p method, the calculation still has similar trends in the polarization ratio value, and the calculation time could be saved. The detail is in Chapter 3.

doi:10.6342/NTU202303083

2.2 Random seeding generator

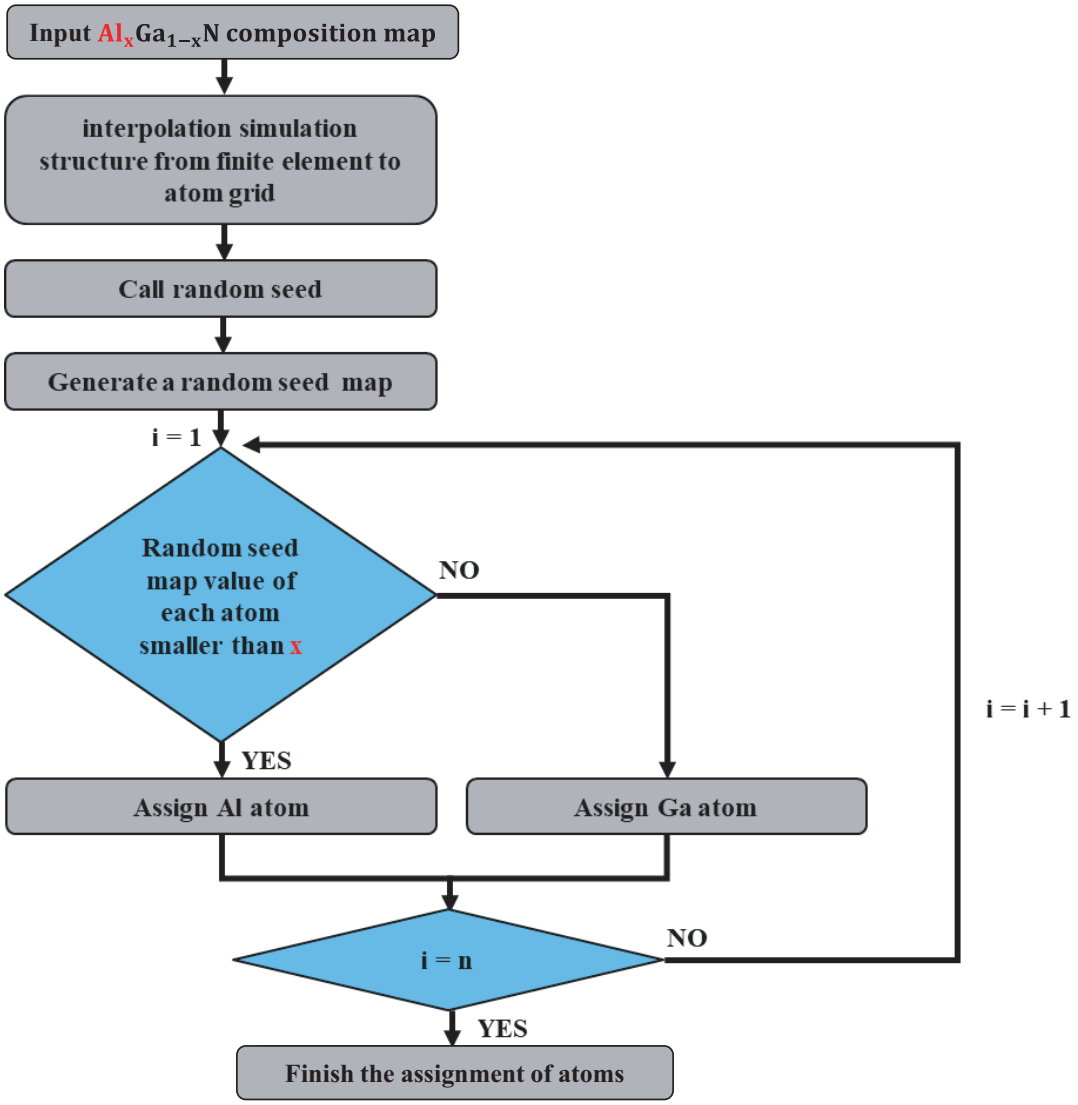

Figure 2.2: The flow chart of the random seeding generator.

The cubic lattice random alloy fluctuation model will be output after inputting the finite element composition map to the additional function of a random seeding generator. The following will discuss the concept of the random seeding generator.

In the random seeding generator, the interpolation is used to change the 3D structure

doi:10.6342/NTU202303083

from the finite element built by the GMSH to the atomic grid and set each atom's spacing as the bonding length of Ga-Ga (a=2.833Å), first.[40, 41] Then, the composition map with the atomic grid will be. Second, in the atomic grid, use the random seeding number to assign the value of 0 to 1 to each atom to get the random seeding map. Finally, we determined the material of the atom in the atomic grid by the random seeding map. For example, if the layer is $Al_{0.6}Ga_{0.4}N$ alloy material. According to the concept, even though the arrangement of the composition map in the atomic grid has an random alloy fluctuation, the average of the Al composition map in that layer must be a value of 0.6.[42] Therefore, by distinguishing the value of the random seeding map in each position is larger or smaller than the average Al composition in this layer, the crystal structure of each cubic lattice will be determined. If the value is larger than the average Al composition, the material of the atom will set Ga and output 0 to the random alloy fluctuation model. In other words, if the value is smaller than the average Al composition, the material of the atom will set Al and output 1 to the random alloy fluctuation model. Therefore, the output of the random seeding generator is the cubic lattice random alloy fluctuation model in the atomic grid, then knowing that the crystal structure of each cubic lattice is GaN or AlN.

2.3 Gaussian weighting calculation

Due to the composition distribution seen in the Gaussian or arbitrary profiles of the experiment, using the Gaussian shape envelope to build the composition map is essential in simulation.[2, 34, 43, 44] As the Gaussian weighting calculation is entirely determined by the nearby atoms' cubic lattice and their distance. The Gaussian weighting calculation will let the composition distribution include the nearby cubic lattice information. Below is the introduction to the Gaussian weighting calculation using in this study.

doi:10.6342/NTU202303083

For the composition map with random alloy fluctuation in the atomic grid, each cubic lattice's composition will determine by the nearby cubic lattice and the spacing between them. The definition of the maximum nearby distance equals the full width at half maximum of the Gaussian envelope (2a≃0.6 nm).[40] The calculation of the Gaussian weighting for each atom in the atomic grid will be under the window with a 0.6 nm diameter. The Gaussian weighting formula in Eq. (2.1) refers to the [40, 41].

$$x_{weighting}(r_m) = \frac{\sum_{r_n} \text{Cubic lattice}(\mathrm{r_n}) e^{-(\mathrm{r_n}-\mathrm{r_m})^2/2\sigma^2}}{\sum_{r_n} e^{-(r_n-r_m)^2/2\sigma^2}}\ , \tag{2.1}$$

where σ is the full width at half maximum of the Gaussian envelope (2a≃0.6 nm), $r_m = (x_m, y_m, z_m)$ is the atomic grid position where we want to know their composition, $r_n = (x_n, y_n, z_n)$ is the nearby position of r_m, Cubic lattice($\mathrm{r_n}$) representing the Ga or Al atom material at the nearby position, and $x_{weighting}(r_m)$ is the value of the Gaussian weighting composition, which is the composition map from the cubic lattice random alloy fluctuation model after the Gaussian weighting calculation at the position r_m. To note, the value of weighting composition ($x_{weighting}(r_m)$) did not consider the cubic lattice itself but considered the nearby position's cubic lattice. The only thing related to it is the spacing between itself and nearby atoms.

Moreover, the value of the composition map with random alloy fluctuation is 0∼1 in the atomic grid due to the Gaussian weighting formula doing the weighting calculation to the value of the cubic lattice random alloy fluctuation mode, either 1 or 0, by the distance. The formula for Gaussian weighting calculation is in Eq. (2.1).[40] Finally, the additional interpolation calculation will change the 3D structure from the atomic grid to the finite element afterward to let the following simulation calculate with a finite element mesh

doi:10.6342/NTU202303083

grid and save the calculation resource used in the 3D simulation.

2.4 Strain solver

$$\begin{bmatrix} \sigma_{xx} \\ \sigma_{yy} \\ \sigma_{zz} \\ \sigma_{yz} \\ \sigma_{zx} \\ \sigma_{xy} \end{bmatrix} = \begin{bmatrix} c_{11} & c_{12} & c_{13} & 0 & 0 & 0 \\ c_{12} & c_{11} & c_{13} & 0 & 0 & 0 \\ c_{13} & c_{13} & c_{33} & 0 & 0 & 0 \\ 0 & 0 & 0 & c_{44} & 0 & 0 \\ 0 & 0 & 0 & 0 & c_{44} & 0 \\ 0 & 0 & 0 & 0 & 0 & \frac{C_{11}-C_{12}}{2} \end{bmatrix} \begin{bmatrix} \epsilon_{xx} \\ \epsilon_{yy} \\ \epsilon_{zz} \\ \epsilon_{yz} \\ \epsilon_{zx} \\ \epsilon_{xy} \end{bmatrix}, \tag{2.2}$$

where the symbol of σ, c, and ϵ are the stress, elastic stiffness constant, and strain, respectively.

Lattice mismatch will cause strain in the structure. The strain in the system will let the atom arrangement deform and produce the force of stress. According to Hook's law, the degree of the deformation will cause stress in different magnitudes. When the pressure is applied, the responses in different materials in different directions will be different because of the crystal orientation and their properties, etc.[15–17, 36]

After considering the sixfold symmetric in the wurtzite structure of nitride material, then 6×6 elastic stiffness constant matrix can simplify as Eq. (2.2). Additionally, piezoelectric polarization is the material's response when applied strain. The piezoelectric polarization formula and its description are listed below; see Eq. (2.4).[45]

According to the sixfold symmetric for the wurtzite structure of nitride material, the leaving term of the strain tensor is the normal strain (ϵ_{xx}, ϵ_{yy}, and ϵ_{zz}). Namely, the value

doi:10.6342/NTU202303083

and the direction of total electric polarization could be evaluated by the symmetric of its crystal arrangement. [45] Therefore, the existing piezoelectric polarization ($\boldsymbol{P_{piezo}}$) in the z direction for the sixfold symmetric AlGaN wurtzite structure is essential because it will tilt the band structure and make the material property more complex and interesting.

$$\boldsymbol{P_{piezo}} = \begin{bmatrix} 0 & 0 & 0 & 0 & e_{15} & 0 \\ 0 & 0 & 0 & e_{15} & 0 & 0 \\ e_{31} & e_{31} & e_{33} & 0 & 0 & 0 \end{bmatrix} \begin{bmatrix} \epsilon_{xx} \\ \epsilon_{yy} \\ \epsilon_{zz} \\ \epsilon_{yz} \\ \epsilon_{zx} \\ \epsilon_{xy} \end{bmatrix} \tag{2.3}$$

$$= \begin{bmatrix} e_{15}\epsilon_{xz} \\ e_{15}\epsilon_{yz} \\ e_{31}(\epsilon_{xx} + \epsilon_{yy}) + e_{33}\epsilon_{zz} \end{bmatrix} \tag{2.4}$$

where the symbol of e is the piezoelectric stress constant.

doi:10.6342/NTU202303083

2.5 The self-consistent Poisson drift-diffusion continuity solver with strain-induced deformation potential localization model

2.5.1 Poisson equation

Following is the derivation of the Poisson equation. After calculating the Poisson equation, the information on potential will know.

$$\nabla \cdot (\epsilon \nabla V) = -q \left(p - n + N_d^+ - N_a^- \pm \rho_{pol} \right), \tag{2.5}$$

where V is potential energy (eV), the symbol ρ means charge density (C/cm^3), the symbol ϵ implies permittivity (F/cm), n and p are the electric and hole carrier density (1/cm^3), the N_a^- and N_d^+ are the p-type and n-type dopant concentration (1/cm^3), and the symbol ρ_{pol} imply the electric density from polarization (1/cm^3).

2.5.2 Localization landscape model

The theory of the LL model brings forward in a 2016's paper.[46] Some studies in our laboratory have used the LL model to simulate and analyze its property.[40, 41, 47] The derivation of the LL model is based on the Schrodinger equation in Eq. (2.6).

$$\hat{H}\psi_{e,h}(\vec{r}) = \left(-\frac{\hbar^2}{2m_{e,h}^*}\Delta + E_{c,v} \right) \psi_{e,h}(\vec{r}) = E_{e,h}\psi_{e,h}(\vec{r}), \tag{2.6}$$

where the symbol of $m_{e,h}^*$ is the effective mass (kg) of electron and hole, the symbol of $E_{c,v}$ is the conduction and valance band potential (eV) , and the symbol of $\psi_{e,h}$ is the electron

doi:10.6342/NTU202303083

and hole wave function distribution.

Then, setting the formula of the landscape $u_{e,h}(\vec{r})$ multiplied by the Hamiltonian of the Schrodinger equation is equal to 1.

$$\hat{H}u_{e,h}(\vec{r}) = \left(-\frac{\hbar^2}{2m^*_{e,h}}\Delta + E_{c,v}\right)u_{e,h}(\vec{r}) = 1 \tag{2.7}$$

$$-\frac{\hbar^2}{2m^*_{e,h}}\Delta u_{e,h}(\vec{r}) + E_{c,v}u_{e,h}(\vec{r}) = 1 \tag{2.8}$$

$$-\frac{\hbar^2}{2m^*_{e,h}}\frac{\Delta u_{e,h}(\vec{r})}{u_{e,h}(\vec{r})} + E_{c,v} = \frac{1}{u_{e,h}(\vec{r})} \tag{2.9}$$

$$\left(E_{c,v} - \frac{1}{u_{e,h}(\vec{r})}\right) = \frac{\hbar^2}{2m^*_{e,h}}\frac{\Delta u_{e,h}(\vec{r})}{u_{e,h}(\vec{r})}, \tag{2.10}$$

where the $u_{e,h}(\vec{r})$ is landscape $u(\vec{r})$ for electron and hole. The explanation of other symbols in this formula has been listed in Eq.(2.6)

Consequently, for the potential in landscape theory, the complicated and computation-intense Schrodinger Hamiltonian will turn to the differential equations with one unknown. Then, after the calculation of Eq. (2.10), the value of landscape $u_{e,h}(\vec{r})$ will be known. The fundamental inequality of LL is in Eq. (2.11)

$$|\psi(\vec{r})| \leq Eu(\vec{r}), \tag{2.11}$$

where $\psi(\vec{r})$is the wave function at different positions, E is the eigenvalue corresponding to the wave function, and u is the landscape parameter.

doi:10.6342/NTU202303083

Based on the fundamental inequality Eq. (2.11), the wave function $\psi(\vec{r})$ will be limited by the landscape $u(\vec{r})$. Namely, the landscape $u(\vec{r})$ has considered the quantum confinement effect. Note that the study from Douglas N. Arnold and coworkers in 2016[46] has shown that replacing the conduction and valance band potential (E_c and E_v) to the reciprocal of landscape $u_{e,h}(\vec{r})$ ($1/u_{e,h}(\vec{r})$) in calculating electron and hole density. The electron and hole density distribution have the carrier confinement effect. Therefore, there has an essential and powerful approximation of the effective confinement potential $W(\vec{r})$, which is the reciprocal of $u(\vec{r})$. After the assumption, the effective confinement potential $W(\vec{r})$ will calculate the band structure with the quantum confinement effect.

$$W(\vec{r}) = 1/u(\vec{r}), \tag{2.12}$$

where the $W(\vec{r})$ is the effective confinement potential in the LL model. The $u(\vec{r})$ is the landscape parameter. Therefore, the $1/u_e(\vec{r})$ is the effective confinement potential for electrons. The $1/u_h(\vec{r})$ is the effective confinement potential for holes.

Because the result of $1/u_e(\vec{r})$ is never larger than the eigenvalue of any quantum state for electrons.[46] In other words, the result of $1/u_h(\vec{r})$ is never smaller than the eigenvalue of any quantum state for holes. Thus, the assumption of replacing the conduction and valance band potential ($E_{c,v}$) by effective confinement potential ($1/u_{e,h}(\vec{r})$) can be set up, and used in the following derivation. [47]

doi:10.6342/NTU202303083

$$n(\vec{r}) = \int_{E_c(\vec{r})}^{+\infty} f_n(E) \times LDOS_n(\vec{r}, E)\, dE, \tag{2.13}$$

$$= \int_{E_c(\vec{r}) \approx 1/u_e(\vec{r})}^{+\infty} f_n(E) \times LDOS_n(\vec{r}, E)\, dE, \tag{2.14}$$

$$p(\vec{r}) = \int_{-\infty}^{E_v(\vec{r})} f_p(E) \times LDOS_p(\vec{r}, E)\, dE, \tag{2.15}$$

$$= \int_{-\infty}^{E_v(\vec{r}) \approx 1/u_h(\vec{r})} f_p(E) \times LDOS_p(\vec{r}, E)\, dE, \tag{2.16}$$

where $n(\vec{r})$ and $p(\vec{r})$ are the electron and hole density in different propagation directions, $E_c(\vec{r})$ and $E_v(\vec{r})$ are conduction and valance band potential, the $1/u_e(\vec{r})$ and $1/u_h(\vec{r})$ are the effective confinement potential for electrons and holes, $f_n(E)$ and $f_p(E)$ are the Fermi-Dirac distribution for electrons and holes under the different eigenvalue, and $LDOS_n(\vec{r}, E)$ and $LDOS_p(\vec{r}, E)$ are the local density of states for electrons and holes in different propagation directions under the different eigenvalue.

$$LDOS_n(\vec{r}, E) = \left(2\pi^2\right)^{-1} \left(\frac{2m_e^*}{\hbar^2}\right)^{3/2} \sqrt{E - E_c(\vec{r})}, \tag{2.17}$$

$$= \left(2\pi^2\right)^{-1} \left(\frac{2m_e^*}{\hbar^2}\right)^{3/2} \sqrt{E - 1/u_e(\vec{r})}, \tag{2.18}$$

$$LDOS_p(\vec{r}, E) = \left(2\pi^2\right)^{-1} \left(\frac{2m_h^*}{\hbar^2}\right)^{3/2} \sqrt{E_v(\vec{r}) - E}, \tag{2.19}$$

$$= \left(2\pi^2\right)^{-1} \left(\frac{2m_h^*}{\hbar^2}\right)^{3/2} \sqrt{1/u_v(\vec{r}) - E}, \tag{2.20}$$

where m_e^* and m_h^* are the effective mass for electron and hole calculated by the effective

doi:10.6342/NTU202303083

mass theory, and the $\hbar$ is the reduced Planck constant (Dirac constant) around 1.055×10^{-34} (J $\cdot$ s).

$$f_n(E) = \frac{1}{1 + exp^{\left(\frac{E-E_{fn}}{k_B T}\right)}}, \tag{2.21}$$

$$f_p(E) = \frac{1}{1 + exp^{\left(\frac{E_{fp}-E}{k_B T}\right)}}, \tag{2.22}$$

Additionally, the landscape theory calculates $u_{e,h}$ based on the Schrodinger equation(the effective mass theory). Therefore, effective confinement potential ($1/u_{e,h}(\vec{r})$) included the quantum confinement effect and the effective mass distribution in different directions and positions. Namely, the carrier density (n, p) and the current density (J_n, J_p) calculated by the effective confinement potential will let the result of them more precisely by including the quantum effect under the effective mass assumption.

doi:10.6342/NTU202303083

2.5.3 k·p method

Traditionally, the 6×6 k·p method calculates the 3-band position induced by strain. The Eigen-values and Eigen-functions of the multi-band are the output of the k·p method.

$$\hat{H}^v\phi = \begin{bmatrix} F+E_v & 0 & -H^* & 0 & K^* & 0 \\ 0 & G+E_v & \Delta & -H^* & 0 & K^* \\ -H & \Delta & \lambda+E_v & 0 & I^* & 0 \\ 0 & -H & 0 & \lambda+E_v & \Delta & I^* \\ K & 0 & I & \Delta & G+E_v & 0 \\ 0 & K & 0 & I & 0 & F+E_v \end{bmatrix} \begin{bmatrix} \phi_1^h \\ \phi_2^h \\ \phi_3^h \\ \phi_4^h \\ \phi_5^h \\ \phi_6^h \end{bmatrix}, \tag{2.23}$$

$$\phi_1^h = \frac{1}{\sqrt{2}}|X+iY,\uparrow\rangle, \tag{2.24}$$

$$\phi_2^h = \frac{1}{\sqrt{2}}|X+iY,\downarrow\rangle, \tag{2.25}$$

$$\phi_3^h = |Z,\uparrow\rangle, \tag{2.26}$$

$$\phi_4^h = |Z,\downarrow\rangle, \tag{2.27}$$

$$\phi_5^h = \frac{1}{\sqrt{2}}|X-iY,\uparrow\rangle, \tag{2.28}$$

$$\phi_6^h = \frac{1}{\sqrt{2}}|X-iY,\downarrow\rangle, \tag{2.29}$$

where $\phi_1^h \sim \phi_6^h$ are the different states of p-orbital for holes.

doi:10.6342/NTU202303083

$$F = \Delta_1 + \Delta_2 + \lambda + \theta, \tag{2.30}$$

$$G = \Delta_1 - \Delta_2 + \lambda + \theta, \tag{2.31}$$

$$\lambda = A_1 k_z^2 + A_2 k_\perp^2 + D_1 \epsilon_{zz} + D_2 \left(\epsilon_{xx} + \epsilon_{yy}\right), \tag{2.32}$$

$$\theta = A_3 k_z^2 + A_4 k_\perp^2 + D_3 \epsilon_{zz} + D_4 \left(\epsilon_{xx} + \epsilon_{yy}\right), \tag{2.33}$$

$$H = i \left(A_6 k_z k_+ + A_7 k_+ + D_6 \epsilon_{z+}\right), \tag{2.34}$$

$$I = i \left(A_6 k_z k_+ - A_7 k_+ + D_6 \epsilon_{z+}\right), \tag{2.35}$$

$$K = A_5 k_z k_+^2 + D_5 \epsilon_+, \tag{2.36}$$

$$\Delta = \sqrt{2}\Delta_3, \tag{2.37}$$

$$\epsilon_+ = \epsilon_{xx} - \epsilon_{yy} + 2i\epsilon_{xy}, \tag{2.38}$$

$$\epsilon_{z+} = \epsilon_{xz} + i\epsilon_{yz}, \tag{2.39}$$

$$k_+ = k_x + ik_y, \tag{2.40}$$

$$k_\perp^2 = k_x^2 + k_y^2, \tag{2.41}$$

doi:10.6342/NTU202303083

Table 2.1: Parameter setting of k·p matrix

Parameters	GaN	AlN
Energy parameter (eV)		
Δ_1	0.022[b]	-0.169[c]
Δ_2, Δ_3	0.005[d]	0.00633[e]
Effective mass (m_0)		
$m^*_{e,x-y}$	0.21	0.32[c]
$m^*_{e,z}$	0.2[b]	0.3[c]
$m^*_{CH1,x-y}$	0.267	0.637
$m^*_{CH1,z}$	1.0989	3.57
$m^*_{CH3,x-y}$	1.0989	4.0
$m^*_{CH3,z}$	0.1524	0.2590
Deformation potential parameters (eV)		
a_c	-4.50	-4.50[a]
D_1	-1.70[b]	-17.1[a]
D_2	6.30[b]	7.9[a]
D_3	8.0[b]	8.8[a]
D_4	-4.0[b]	-3.9[a]
D_5	-4.0[b]	-3.4[a]
D_6	-5.5[b]	-3.4[a]
Valence band effective-mass parameters ($\hbar^2/2m_0$)		
A_1	-6.56[a]	-3.86[c]
A_2	-0.91[a]	-0.25[c]
A_3	5.65 [a]	3.58 [c]
A_4	-2.83[a]	-1.32[c]
$A-5$	-3.13[a]	-1.47[c]
$A-6$	-4.86[a]	-1.64[c]

[a]Reference [35] [b]Reference [36] [c]Reference [37]
[d]Reference [48] [e]Reference [23]

2.5.4 Strain-induced deformation potential localization landscape model

In the past study of our laboratory, we will input the potential of dominant valance in the LL model to the k·p method, then get the 3-band positions after that.[23] However, for calculating AlGaN materials with a high Al composition in the LL model, the dedication of the 3-bands could not simplify to the dedication of the dominant valance band. Suppose we use the dominant valance band calculated by the LL model to the k·p method. For Al-

doi:10.6342/NTU202303083

GaN with a high Al case, its Eigen solution's result will not be precise due to insufficient information from the LL model's dominant valance band. Therefore, after including the strain-induced deformation potential of three bands in the traditional LL model, the calculation can transfer from the dominant band formula and its effective mass to the three formulas for multi-bands and their effective masses. The main difference is that the three-band formula could include more detailed information about different bands. Thus, the strain-induced deformation potential LL model is helpful in the calculation of multi-band material. The discussion of how the influence of strain-induced deformation potential could add to the LL model and what kind of strains will include will occur afterward.

The Schrodinger equation and LL theory have been considered the effective mass theory.[40, 41, 47] To add that, the LL theory derivation is according to the Schrodinger equation. The effective mass theory approaches the mass used in the calculation to ground state mass. In brief, for the wave vector k that is away from the band gap, its corresponding carrier's mass information will be neglected in the effective mass theory.

In order to let the LL model include the strain-induced deformation potential information from the k·p method, using the concept of effective mass theory to simplify the k·p method. Based on the effective mass theory, it only considers the mass value of the band gap's wave vector k. The off-diagonal terms in the k·p matrix, which are the response of energy mixing for different state interactions, can be neglected due to the off-diagonal terms basically dedicated by being proportional to the k square, see Eq. (2.42) to Eq. (2.45) Namely, the influence of the off-diagonal can be seen just when the wave vector k is far away from the band gap, which is usually the high energy states instead of ground

doi:10.6342/NTU202303083

states. Following are the 3 approximation of the off-diagonal term in the k·p method,

$$H = i\left(A_6 k_z k_+ + A_7 k_+ + D_6 \epsilon_{z+}\right) \approx 0, \tag{2.42}$$

$$I \ = i\left(A_6 k_z k_+ - A_7 k_+ + D_6 \epsilon_{z+}\right) \approx 0, \tag{2.43}$$

$$K = A_5 k_z k_+^2 + D_5 \epsilon_+ \approx 0, \tag{2.44}$$

$$\hat{H}^v \phi = \begin{bmatrix} F+E_v & 0 & 0 & 0 & 0 & 0 \\ 0 & G+E_v & 0 & 0 & 0 & 0 \\ 0 & 0 & \lambda+E_v & 0 & 0 & 0 \\ 0 & 0 & 0 & \lambda+E_v & 0 & 0 \\ 0 & 0 & 0 & 0 & G+E_v & 0 \\ 0 & 0 & 0 & 0 & 0 & F+E_v \end{bmatrix} \begin{bmatrix} \phi_1^h \\ \phi_2^h \\ \phi_3^h \\ \phi_4^h \\ \phi_5^h \\ \phi_6^h \end{bmatrix} = E\phi, \tag{2.45}$$

where ϕ is the eigenvector in six states, which describes their wave function distribution, E_v is the valance band potential, and E is the eigenvalue of six states. In addition, all the detailed information of the k·p matrix is listed in Chapter 2.5.3.

After ignoring the off-diagonal terms, the k·p matrix will transfer to the diagonal matrix, leaving the three bands formula in Eq. (2.46) to Eq. (2.48):

$$\left(F+E_v\right)\phi_1^v = E_{CH1}\phi_1^v, \tag{2.46}$$

$$\left(G+E_v\right)\phi_2^v = E_{CH2}\phi_2^v, \tag{2.47}$$

$$\left(\lambda+E_v\right)\phi_3^v = E_{CH3}\phi_3^v, \tag{2.48}$$

where ϕ is the eigenvector and describes the wave function distribution. E_v is the valance

doi:10.6342/NTU202303083

band potential. The E_{CH1} is the eigenvalue of $|X+iY,\uparrow\rangle$ or $|X-iY,\downarrow\rangle$) state. , E_{CH2} is the eigenvalue of $|X-iY,\uparrow\rangle$ or $|X+iY,\downarrow\rangle$) state. E_{CH3} is the eigenvalue of $|Z,\uparrow\rangle$ or $|Z,\downarrow\rangle$ state.

After expanding the three bands formula in Eq. (2.46) to Eq. (2.48), we can get the strain-induced deformation potential localized landscape model. Hence, in the strain-induced deformation potential LL model, the information of three bands can be solved without the k·p method calculation. Furthermore, this study will also include the deformation induced by strain in the conduction band. Differently, the forming of it is not the same as the valance band deformation energy in k·p but the hydrostatic deformation potential, see Eq. (2.49).

$$\left(-\frac{\hbar^2}{2m_e^*}\nabla^2 + E_c + \Delta E_{c,\text{strain}}\right) u_e(\vec{r}) = 1, \tag{2.49}$$

$$\left(-\frac{\hbar^2}{2m_{h,CH1}^*}\nabla^2 + E_v + \Delta_1 + \Delta_2 + \Delta E_{v,\text{strain},CH1}\right) u_{h,CH1}(\vec{r}) = 1, \tag{2.50}$$

$$\left(-\frac{\hbar^2}{2m_{h,CH2}^*}\nabla^2 + E_v + \Delta_1 - \Delta_2 + \Delta E_{v,\text{strain},CH2}\right) u_{h,CH2}(\vec{r}) = 1, \tag{2.51}$$

$$\left(-\frac{\hbar^2}{2m_{h,CH3}^*}\nabla^2 + E_v + \Delta E_{v,\text{strain},CH3}\right) u_{h,CH3}(\vec{r}) = 1, \tag{2.52}$$

where the $m_{h,CH1}^*$, $m_{h,CH2}^*$, and $m_{h,CH3}^*$ are the effective mass calculated by the k·p method's parameter. E_v and E_c are the valance band potential calculated by the Poisson equation in this study, Δ_1 and Δ_2 are spin-orbit split-off energy, which is the energy splitting under the bands' interaction. $\Delta E_{v,\text{deform},CH1}$, $\Delta E_{v,\text{deform},CH2}$, $\Delta E_{v,\text{deform},CH3}$, and $\Delta E_{c,\text{strain}}$ are the strain caused deformation potential in CH1, CH2, CH3, and conduction band. $u_{h,CH1}(\vec{r})$, $u_{h,CH2}(\vec{r})$, $u_{h,CH3}(\vec{r})$, and $u_e(\vec{r})$ are the landscape $u(\vec{r})$ of different bands

doi:10.6342/NTU202303083

for holes and electrons.

$$\Delta E_{c,\text{strain}} = \Delta E_{c,\text{hydrostatic}}, \tag{2.53}$$

$$\Delta E_{v,\text{strain},CH1} = \Delta E_{v,\text{hydrostatic}} + \Delta E_{v,\text{deform},CH1}, \tag{2.54}$$

$$\Delta E_{v,\text{strain},CH2} = \Delta E_{v,\text{hydrostatic}} + \Delta E_{v,\text{deform},CH2}, \tag{2.55}$$

$$\Delta E_{v,\text{strain},CH3} = \Delta E_{v,\text{hydrostatic}} + \Delta E_{v,\text{deform},CH3}, \tag{2.56}$$

where $\Delta E_{v,\text{deform},CH1}$, $\Delta E_{v,\text{deform},CH2}$, and$\Delta E_{v,\text{deform},CH3}$ are the CH1, CH2, and CH3 band deformation from the valence-band deformation potential induced by strain. The $\Delta E_{c,\text{hydrostatic}}$ and $\Delta E_{v,\text{hydrostatic}}$ are conduction and valance deformation from the hydrostatic deformation potential induced by strain.

$$\Delta E_{v,\text{deform},CH1} = (D_1 + D_3)\,\epsilon_{zz} + (D_2 + D_4)\,(\epsilon_{xx} + \epsilon_{yy}), \tag{2.57}$$

$$\Delta E_{v,\text{deform},CH2} = (D_1 + D_3)\,\epsilon_{zz} + (D_2 + D_4)\,(\epsilon_{xx} + \epsilon_{yy}), \tag{2.58}$$

$$\Delta E_{v,\text{deform},CH3} = (D_1)\,\epsilon_{zz} + (D_2)\,(\epsilon_{xx} + \epsilon_{yy}), \tag{2.59}$$

where the $D_1 \sim D_4$ are the valence-band deformation potential in the k·p method, and the ϵ_{xx}, ϵ_{yy}, and ϵ_{zz} are a strain in a different direction.

$$\Delta E_{c,\text{hydrostatic}} = a\,(\epsilon_{xx} + \epsilon_{yy} + \epsilon_{zz}) \times (\text{conduction band offset ratio}), \tag{2.60}$$

$$\Delta E_{v,\text{hydrostatic}} = a\,(\epsilon_{xx} + \epsilon_{yy} + \epsilon_{zz}) \times (\text{conduction band offset ratio} - 1), \tag{2.61}$$

where a is hydrostatic deformation potential, and the ϵ is a strain in a different direction.

Due to the ratio of the conduction band difference (ΔE_c) and the valance band dif-

doi:10.6342/NTU202303083

ference (ΔE_v) in the discontinuity band gap of the GaN/AlGaN interface is assumed to be 0.63.[47, 49] Therefore, the conduction band offset ratio is 0.63 in this work. To sum up, in the above equation, strain-caused $\Delta E_{c,\text{strain}}$, $\Delta E_{v,\text{deform},CH1}$, $\Delta E_{v,\text{deform},CH2}$, and $\Delta E_{v,\text{deform},CH3}$ are the CB, CH1, CH2, and CH3 band potential difference induced by strain. The potential difference induced by strain can be divided into two parts. One is the strain-caused valance band deformation potential from $D_1 \sim D_6$ in k·p ($\Delta E_{v,\text{deform},CH1}$, $\Delta E_{v,\text{deform},CH2}$, and $\Delta E_{v,\text{deform},CH3}$) caused, another is strain caused band gap changing from hydrostatic deformation potential ($\Delta E_{v,\text{hydrostatic}}$ and $\Delta E_{v,\text{hydrostatic}}$). The influence of strain will discuss in Chapter 5.

The formula below is the expansion of the second differential term in Eq. (2.50) ~ Eq. (2.52).

$$-\frac{\hbar^2}{2m^*_{h,CH1}}\Delta = -\frac{\hbar^2}{2}\left(\frac{1}{m^*_{h,CH1,x}}\frac{\partial^2}{\partial x^2}+\frac{1}{m^*_{h,CH1,y}}\frac{\partial^2}{\partial y^2}+\frac{1}{m^*_{h,CH1,z}}\frac{\partial^2}{\partial z^2}\right), \tag{2.62}$$

$$-\frac{\hbar^2}{2m^*_{h,CH2}}\Delta = -\frac{\hbar^2}{2}\left(\frac{1}{m^*_{h,CH2,x}}\frac{\partial^2}{\partial x^2}+\frac{1}{m^*_{h,CH2,y}}\frac{\partial^2}{\partial y^2}+\frac{1}{m^*_{h,CH2,z}}\frac{\partial^2}{\partial z^2}\right), \tag{2.63}$$

$$-\frac{\hbar^2}{2m^*_{h,CH3}}\Delta = -\frac{\hbar^2}{2}\left(\frac{1}{m^*_{h,CH3,x}}\frac{\partial^2}{\partial x^2}+\frac{1}{m^*_{h,CH3,y}}\frac{\partial^2}{\partial y^2}+\frac{1}{m^*_{h,CH3,z}}\frac{\partial^2}{\partial z^2}\right), \tag{2.64}$$

In the strain-induced deformation potential LL model, the parameter of deformation potential comes from the k·p method. To make the calculation more easily converge and include the three bands' information, the mass parameter in the LL model will also adopt the valence band effective-mass parameter A in the k·p method. Based on the mass-related terms (A) of the 3-band formula (Eq. (2.46) to Eq. (2.48)) in the F, G, and λ terms and the formula listed in Eq. (2.41), we can get the following equation.

doi:10.6342/NTU202303083

$$m^*_{\mathrm{AlN},CH1,z} = \left| \frac{1}{A_{1,\mathrm{AlN}} + A_{3,\mathrm{AlN}}} \right|, \tag{2.65}$$

$$m^*_{\mathrm{AlN},CH1,x-y} = \left| \frac{1}{A_{2,\mathrm{AlN}} + A_{4,\mathrm{AlN}}} \right|, \tag{2.66}$$

$$m^*_{\mathrm{AlN},CH2,z} = \left| \frac{1}{A_{1,\mathrm{AlN}} + A_{3,\mathrm{AlN}}} \right|, \tag{2.67}$$

$$m^*_{\mathrm{AlN},CH2,x-y} = \left| \frac{1}{A_{2,\mathrm{AlN}} + A_{4,\mathrm{AlN}}} \right|, \tag{2.68}$$

$$m^*_{\mathrm{AlN},CH3,z} = \left| \frac{1}{A_{1,\mathrm{AlN}}} \right|, \tag{2.69}$$

$$m^*_{\mathrm{AlN},CH3,x-y} = \left| \frac{1}{A_{2,\mathrm{AlN}}} \right|, \tag{2.70}$$

where the symbols of $m^*_{\mathrm{AlN},CH1,z}$, $m^*_{\mathrm{AlN},CH1,x-y}$, $m^*_{\mathrm{AlN},CH2,z}$, $m^*_{\mathrm{AlN},CH2,x-y}$, $m^*_{\mathrm{AlN},CH3,z}$, and $m^*_{\mathrm{AlN},CH3,x-y}$ are the CH1, CH2, and CH3 band effective mass of AlN material in z and x-y directions, respectively. $A_{1,\mathrm{AlN}} \sim A_{4,\mathrm{AlN}}$ are valence band effective-mass parameter A for AlN in the k·p.

$$m^*_{\mathrm{GaN},CH1,z} = \left| \frac{1}{A_{1,\mathrm{GaN}} + A_{3,\mathrm{GaN}}} \right|, \tag{2.71}$$

$$m^*_{\mathrm{GaN},CH1,x-y} = \left| \frac{1}{A_{2,\mathrm{GaN}} + A_{4,\mathrm{GaN}}} \right|, \tag{2.72}$$

$$m^*_{\mathrm{GaN},CH2,z} = \left| \frac{1}{A_{1,\mathrm{GaN}} + A_{3,\mathrm{GaN}}} \right|, \tag{2.73}$$

$$m^*_{\mathrm{GaN},CH2,x-y} = \left| \frac{1}{A_{2,\mathrm{GaN}} + A_{4,\mathrm{GaN}}} \right|, \tag{2.74}$$

$$m^*_{\mathrm{GaN},CH3,z} = \left| \frac{1}{A_{1,\mathrm{GaN}}} \right|, \tag{2.75}$$

$$m^*_{\mathrm{GaN},CH3,x-y} = \left| \frac{1}{A_{2,\mathrm{GaN}}} \right|, \tag{2.76}$$

where the symbols of $m^*_{\mathrm{GaN},CH1,z}$, $m^*_{\mathrm{GaN},CH1,x-y}$, $m^*_{\mathrm{GaN},CH2,z}$, $m^*_{\mathrm{GaN},CH2,x-y}$, $m^*_{\mathrm{GaN},CH3,z}$, and

doi:10.6342/NTU202303083

$m^*_{\text{GaN},CH3,x-y}$ are the CH1, CH2, and CH3 band effective mass of GaN material in z and x-y directions, respectively. $A_{1,\text{GaN}} \sim A_{4,\text{GaN}}$ are valence band effective-mass parameters A for GaN in the k·p.

The effective mass calculates by the linear interpolation of AlN and GaN composition after that. The effective mass of the $Al_xGa_{1-x}N$ alloy could be known and used in the Poisson drift-diffusion continuity solver with a strain-induced deformation potential LL model.

$$\frac{1}{m^*_{CH1,z}} = \frac{x}{m^*_{\text{AlN},CH1,z}} + \frac{1-x}{m^*_{\text{GaN},CH1,z}}, \tag{2.77}$$

$$\frac{1}{m^*_{CH1,x-y}} = \frac{x}{m^*_{\text{AlN},CH1,x-y}} + \frac{1-x}{m^*_{\text{GaN},CH1,x-y}}, \tag{2.78}$$

$$\frac{1}{m^*_{CH2,z}} = \frac{x}{m^*_{\text{AlN},CH2,z}} + \frac{1-x}{m^*_{\text{GaN},CH2,z}}, \tag{2.79}$$

$$\frac{1}{m^*_{CH2,x-y}} = \frac{x}{m^*_{\text{AlN},CH2,x-y}} + \frac{1-x}{m^*_{\text{GaN},CH2,x-y}}, \tag{2.80}$$

$$\frac{1}{m^*_{CH3,z}} = \frac{x}{m^*_{\text{AlN},CH3,z}} + \frac{1-x}{m^*_{\text{GaN},CH3,z}}, \tag{2.81}$$

$$\frac{1}{m^*_{CH3,x-y}} = \frac{x}{m^*_{\text{AlN},CH3,x-y}} + \frac{1-x}{m^*_{\text{GaN},CH3,x-y}}, \tag{2.82}$$

where the symbol of $m^*_{CH1,z}$, and $m^*_{CH1,x-y}$ are the CH1 band effective mass of $Al_xGa_{1-x}N$ alloy in z and x-y direction, respectively. The symbol of $m^*_{CH2,z}$, and $m^*_{CH2,x-y}$ are the CH2 band effective mass of $Al_xGa_{1-x}N$ alloy in z and x-y direction, respectively. The symbol of $m^*_{CH3,z}$, and $m^*_{CH3,x-y}$ are the CH3 band effective mass of $Al_xGa_{1-x}N$ alloy in z and x-y direction, respectively.

doi:10.6342/NTU202303083

2.5.5 Drift-diffusion equation

$$\vec{J_n} = -q\mu_n n\vec{\nabla}E_c + qD_n\vec{\nabla}n, \tag{2.83}$$

$$\vec{J_p} = -q\mu_p p\vec{\nabla}E_v - qD_p\vec{\nabla}p, \tag{2.84}$$

where the μ_n and μ_p are the mobility (m^2/ (V· s)) for electrons and holes, D_n and D_p are the diffusion coefficient (m^2/s) of electrons and holes, and J_n and J_p are the current density (A/cm^2) of electrons and holes. n and p are the electron and hole density (1/cm^3).

2.5.6 Continuity equation

Based on Maxwell's equation

$$\vec{\nabla} \times \vec{H} = \vec{J} + \frac{\partial \vec{D}}{\partial t}, \tag{2.85}$$

$$\vec{\nabla} \cdot \vec{\nabla} \times \vec{H} = \vec{\nabla} \cdot \vec{J} + \frac{\partial \vec{\nabla} \cdot \vec{D}}{\partial t}, \tag{2.86}$$

$$0 = \nabla^2 \vec{H} = \vec{\nabla} \cdot \vec{J} + \frac{\partial \rho}{\partial t}, \tag{2.87}$$

where the symbol ρ means charge density (C/cm^3), and the $\vec{H}$ is the vector of the magnetic field (A/m). Under the steady state and considering the recombination-generation machine of the system, the continuity equation will solve not the transient state but the steady-state current density.

$$0 = \frac{\partial n}{\partial t} = \frac{1}{q}\vec{\nabla} \cdot \vec{J_n} - (R - G), \tag{2.88}$$

$$0 = -\frac{\partial p}{\partial t} = \frac{1}{q}\vec{\nabla} \cdot \vec{J_p} - (R - G), \tag{2.89}$$

doi:10.6342/NTU202303083

where R and G are the recombination and generation in the system.

$$R \approx R_{SRH} + R_{Radiative} + R_{Auger}, \tag{2.90}$$

$$R_{SRH} = \frac{np - n_i^2}{\tau_p \left(n + N_c e^{\left(\frac{E_t - Ec}{k_B T}\right)} \right) + \tau_n \left(p + N_v e^{\left(\frac{Ev - E_t}{k_B T}\right)} \right)}, \tag{2.91}$$

$$R_{Radiative} = B_0 np, \tag{2.92}$$

$$R_{Auger} = C_0 \left(n^2 p + p^2 n \right), \tag{2.93}$$

Above are the formula of Shockley-read-hall, radiative, and Auger recombination.[50, 51] B_0 and C_0 are the radiative recombination coefficient (cm^3/s) and Auger recombination coefficient (cm^6/s). n and p are the electron and hole density (1/cm^3).

After considering the drift-diffusion equation with the continuity equation under the steady-state ($G \approx 0$), the equation can be transferred to:

$$-\mu_n n \vec{\nabla}^2 Ec - \mu_n \vec{\nabla} n \vec{\nabla} Ec + D_n \nabla^2 n = \left(R_{SRH} + B_0 np + C_0 \left(n^2 p + p^2 n \right) \right), \tag{2.94}$$

$$-\mu_p p \vec{\nabla}^2 Ev - \mu_p \vec{\nabla} p \vec{\nabla} Ev - D_p \nabla^2 p = \left(R_{SRH} + B_0 np + C_0 \left(n^2 p + p^2 n \right) \right), \tag{2.95}$$

Therefore, the information on radiative recombination, non-radiative recombination, auger recombination, and overflow will be output. Then, know the IQE in the system.

doi:10.6342/NTU202303083

2.6 Another equation use in the k·p method model

2.6.1 Wave function overlap

To describe the existing probability of the particle by the form of the wave in volume, the integration of the probability density function by volume should be a unit.[52] Therefore, under the same eigenvalue, the integration of the wave function square in six states should be a unit in the volume. Here we calculated the wave function from the k·p method and normalized them first. Then, we multiply the hole and electron's complex form wave function in different states and take the absolute value of it. Therefore, the value of wave function overlap can be known.

2.6.2 EL intensity equation

$$R = \int \frac{q^2 n_r \hbar\omega}{\pi m_0^2 \epsilon_0 c^3 \hbar^2} \frac{1}{3} \sum_{i,j} |\langle \phi_i u_s | \hat{a}\cdot\hat{p} | \phi_j u_p \rangle|^2 f^e(E_i^e) f^h(E_j^h) \times \frac{1}{\sqrt{2\pi}\sigma} exp^{\left(\frac{-(E_{i,j}-\hbar\omega)^2}{2\sigma^2}\right)} d(\hbar\omega), \tag{2.96}$$

where R is the Electroluminescence (EL) intensity generated by radiative recombination, n_r is the relative permittivity, i implies the state of electrons, j means the state of holes, $\frac{1}{3}$ is for the EL intensity in one propagation direction, $\langle \phi_i u_s | \hat{a}\cdot\hat{p} | \phi_j u_p \rangle$ describe different state transition and their wave function overlap under the perturbation theory, ϕ_i and ϕ_j are the i_{th} and j_{th}states of the conduction band and valance bands, u_s and u_p are the core states of s and p orbitals distributed in the conduction band or valence bands, $\hat{a}$ is the polarization direction of the electric field that forms the output light, $\hat{p}$ is the momentum

doi:10.6342/NTU202303083

operator in the quantum system, $E_{i,j}$ is the eigenvalue of electrons and holes, σ is half of the full width at half maximum in the Gaussian envelope, $f_e(E_i^e)$ and $f_h(E_j^h)$ are the Fermi-Dirac distribution for electrons and holes in different eigenstates.

The polarization direction of the light emission will be determined by the eigenstate of the holes, as mentioned above. In addition, the EL intensity is the response of the electron-hole pair transition. Therefore, the polarization direction of the EL intensity will be determined by the eigenstate of the hole in the transition. Such as, the conduction band to CH1 band transition (C-CH1) will emit the TE-polarized light. On the other hand, the conduction band to CH3 band transition (C-CH3) will emit the TM-polarized light. Namely, the EL intensity could divide into I_{TE} or I_{TM} by the eigenstate of the hole in transition. After calculating the polarization ratio equation in Eq. (2.97), the value of the polarization ratio will be obtained.

$$\text{Polarization ratio} = \frac{\mathrm{I_{TM}} - \mathrm{I_{TE}}}{\mathrm{I_{TM}} + \mathrm{I_{TE}}}, \tag{2.97}$$

doi:10.6342/NTU202303083

Chapter 3 Strain-induced localization landscape model

3.1 Simulation structure

Following are the simulation structure and the parameter setting in this work.

Table 3.1: Fixing parameters in this study

	n-AlGaN	n-first QB	QW/QB	LQB	p-AlGaN	p-$Al_xGa_{1-x}N$	p-GaN
μ_n ($cm^2\ V^{-1}\ s^{-1}$)	21.9	21.9	100	5	5	5	5
μ_p ($cm^2\ V^{-1}\ s^{-1}$)	2	2	5	2	2	2	2
Doping (cm^{-3})	5×10^{19}	5×10^{19}	–	5×10^{18}	5×10^{19}	5×10^{19}	5×10^{19}
Impurity (cm^{-3})	–	10^{17}	10^{17}	–	–	–	–
$\tau_{n,nonrad}$ (s)	10^{-8}	10^{-8}	10^{-8}	10^{-8}	10^{-8}	10^{-8}	10^{-8}
$\tau_{p,nonrad}$ (s)	10^{-8}	10^{-8}	10^{-8}	10^{-8}	10^{-8}	10^{-8}	10^{-8}
B_0 coefficient (cm^3/s)	2×10^{-11}	2×10^{-11}	2×10^{-11}	2×10^{-11}	2×10^{-11}	2×10^{-11}	2×10^{-11}
C_0 coefficient (cm^6/s)	2×10^{-31}	2×10^{-31}	2×10^{-31}	2×10^{-31}	2×10^{-31}	2×10^{-31}	2×10^{-31}

Table 3.2: The simulation parameters of 225 nm's UVC-LEDs

	n-AlGaN	n-first QB	QW/QB	LQB	p-AlGaN	p-$Al_xGa_{1-x}N$	p-GaN
Thickness (nm)	40	$2/10$ (total 70)			10	1×12	33
Al composition (%)	100	100	80/100	100	93.75	87.5–0	0
Activation energy (meV)	110	110	–	600	573.75	547.5–180 linear interpolation with Al composition	180
$m^*_{CH1,z}$ (m_0)	3.57	3.57	2.46/3.57	3.57	3.13	2.79–1.10	1.10
$m^*_{CH1,x-y}$ (m_0)	0.64	0.64	0.50/0.64	0.64	0.59	0.54–0.27	0.27
$m^*_{CH3,z}$ (m_0)	0.26	0.26	0.23/0.26	0.26	0.25	0.24–0.15	0.15
$m^*_{CH3,x-y}$ (m_0)	4.00	4.00	2.62/4.00	4.00	3.43	3.01–1.10	1.10

doi:10.6342/NTU202303083

Table 3.3: The simulation parameters of 253 nm's UVC-LEDs

	n-AlGaN	n-first QB	QW/QB	LQB	p-AlGaN	p-$Al_xGa_{1-x}N$	p-GaN
Thickness (nm)	40	$2/10$ (total 70)			10	0.8×12	33
Al composition (%)	80	80	60/80	80	75	70–0	0
Activation energy (meV)	93	93	–	516	495	474–180 linear interpolation with Al composition	180
$m^*_{CH1,z}$ (m_0)	2.46	2.46	1.88/2.46	2.46	2.29	2.13–1.10	1.10
$m^*_{CH1,x-y}$ (m_0)	0.50	0.50	0.41/0.50	0.50	0.47	0.45–0.27	0.27
$m^*_{CH3,z}$ (m_0)	0.23	0.23	0.20/0.23	0.23	0.22	0.21–0.15	0.15
$m^*_{CH3,x-y}$ (m_0)	2.62	2.62	1.95/2.62	2.62	2.41	2.23–1.10	1.10

Table 3.4: The simulation parameters of 267 nm's UVC-LEDs

	n-AlGaN	n-first QB	QW/QB	LQB	p-AlGaN	p-$Al_xGa_{1-x}N$	p-GaN
Thickness (nm)	40	$2/10$ (total 70)			10	1×12	33
Al composition (%)	70	70	50/70	70	61.25	52.5–0	0
Activation energy (meV)	84.5	84.5	–	474	437	401–180 linear interpolation with Al composition	180
$m^*_{CH1,z}$ (m_0)	2.13	2.13	1.68/2.13	2.13	1.91	1.73–1.10	1.10
$m^*_{CH1,x-y}$ (m_0)	0.45	0.45	0.38/0.45	0.45	0.41	0.38–0.27	0.27
$m^*_{CH3,z}$ (m_0)	0.21	0.21	0.19/0.21	0.21	0.20	0.19–0.15	0.15
$m^*_{CH3,x-y}$ (m_0)	2.23	2.23	1.72/2.23	2.23	1.97	1.77–1.10	1.10

Table 3.5: The simulation parameters of 282 nm's UVC-LEDs

	n-AlGaN	n-first QB	QW/QB	LQB	p-AlGaN	p-$Al_xGa_{1-x}N$	p-GaN
Thickness (nm)	40	$2/10$ (total 70)			10	1×12	33
Al composition (%)	60	60	40/60	60	52.5	45–0	0
Activation energy (meV)	76	76	–	432	401	369–180 linear interpolation with Al composition	180
$m^*_{CH1,z}$ (m_0)	1.88	1.88	1.52/1.88	1.88	1.73	1.60–1.10	1.10
$m^*_{CH1,x-y}$ (m_0)	0.41	0.41	0.35/0.41	0.41	0.38	0.36–0.27	0.27
$m^*_{CH3,z}$ (m_0)	0.20	0.20	0.18/0.20	0.20	0.19	0.19–0.15	0.15
$m^*_{CH3,x-y}$ (m_0)	1.95	1.95	1.55/1.95	1.95	1.77	1.63–1.10	1.10

doi:10.6342/NTU202303083

Table 3.6: The simulation parameters of 299 nm's UVB-LEDs

	n-AlGaN	n-first QB	QW/QB	LQB	p-AlGaN	p-$Al_xGa_{1-x}N$	p-GaN
Thickness (nm)	40	2/10 (total 70)			10	1×12	33
Al composition (%)	50	50	30/50	55	46.41	37.81–0	0
Activation energy (meV)	68	68	–	411	375	339–180 linear interpolation with Al composition	180
$m^*_{CH1,z}$ (m_0)	1.77	1.77	1.39/1.77	1.77	1.62	1.49–1.10	1.10
$m^*_{CH1,x-y}$ (m_0)	0.39	0.39	0.32/0.39	0.39	0.37	0.34–0.27	0.27
$m^*_{CH3,z}$ (m_0)	0.20	0.20	0.17/0.20	0.20	0.19	0.18–0.15	0.15
$m^*_{CH3,x-y}$ (m_0)	1.83	1.83	1.40/1.83	1.83	1.66	1.51–1.10	1.10

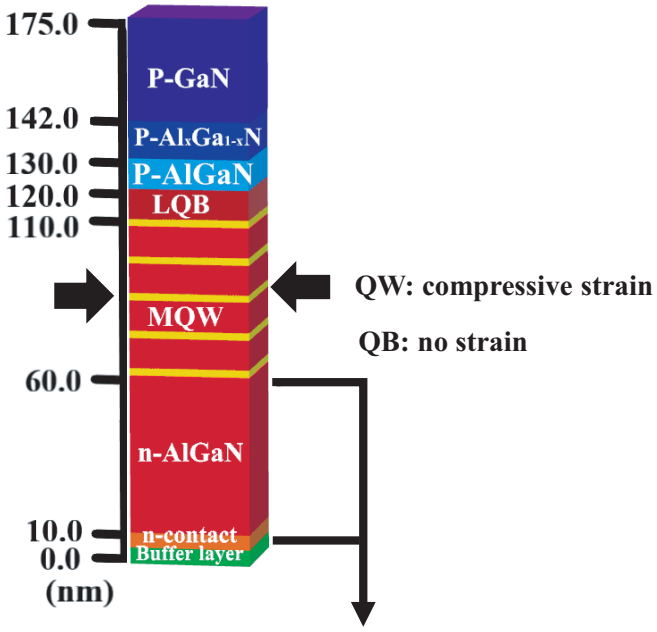

Figure 3.1: Simulation structure in this study

In this study, the simulation structure shown in Fig. 3.1, the structure including the 5 nm AlGaN transition buffer layer followed by 5 nm AlGaN n-contact, 50 nm n-AlGaN doping layer to improve the electron carriers injection, the MQW group by 2 nm AlGaN QW/10 nm AlGaN QB, the 10 nm AlGaN Last QW, 10 nm n-AlGaN dopant layer to help the hole carrier injection, 12 nm (9.6 nm) AlGaN gradual layer in 225 nm (253 nm) to fix the composition slope in the p-AlGaN gradual layer in different wavelengths, and 33 nm

doi:10.6342/NTU202303083

p-AlGaN to form the ohmic contact with metal. Under the limitation of the calculation source in 3D simulation, the periodic boundary setting can effectively decrease the size of the simulation structure. The simulation structure is $L_x \times L_y = 30 \times 30$ (nm^2) in the random alloy fluctuation case and $L_x \times L_y = 50 \times 50$ (nm^2) in the without random alloy fluctuation case. The L_z= 175 nm and 172.6 nm in 225 nm and 253 nm cases, respectively. Additionally, the ten seedlings' data will average the result of the random alloy fluctuation cases.[23] Then, the concept of the simulation design in this work will explain afterward.

The following is the motivation for the structure design. First, due to the wurtzite GaN crystal orientation will let the electrons and holes accumulate at the different side tilted quantum potential and decrease the wave function overlap.[15–17]. The thin quantum well design in 2 nm will have better electron-hole overlap due to the smaller distance to separate the carriers.[7] But it also reduces the allowed carrier density in the QW, which is also a drawback discussed in Chapter 4. Therefore, the larger wave function overlap will reduce the radiative lifetime and increase the IQE. Therefore, in our study's MQW structure, the 2 nm $Al_xGa_{1-x}N$ quantum well is sandwiched by the 5 nm $Al_xGa_{1-x}N$ QBs[53]. Second, using the p-$Al_xGa_{1-x}N$ gradual layer to help the hole carrier injection based on the GaN to metal ohmic contact design. Therefore, the barrier for holes to injection can effectively decrease.

The following will introduce how the strain is applied by the simulation structure design in this study and divided into two parts: the transport contact layer and the buffer layer.

For the limitation of the calculation source in 3D simulation, this work uses the transition buffer layer followed by the n-contact layer and the n-AlGaN layer structure arrange-

doi:10.6342/NTU202303083

ment to simulate the epitaxial layer of lateral LEDs below the MQW region. Also, the metal contact will be at the side wall of the n-AlGaN layer to simulate the electron injection from the n-AlGaN layer to the active region because the electron is not injected from the buffer layer or substrate in most cases. Namely, the Al composition in the n-AlGaN and the AlGaN n-contact layer are the same.

Generally, the template of sapphire substrate with an AlN buffer layer will be used in GaN growth to relax strain caused by lattice mismatch[54]. Several groups[55–57] have reported that the AlN buffer layer can effectively decrease the threading dislocation density in III-nitride wurtzite GaN. Furthermore, other semiconductor fabrication, like high-temperature annealing and pattern substrate, could further reduce the TDD and improve the IQE.

For the lattice mismatch problem in n-AlGaN and AlN buffer layer, the thick transition AlGaN layer or the AlGaN gradual layer will be added between the AlN and n-AlGaN in the experiment.[6, 55–57] Due to the transition layer used to release the strain and decrease the defect in the active region, the definition of the buffer layer includes the AlN in the bottom followed by a thick transition layer. This study's simulation structure includes the top layer in the transition AlGaN layer, which is named the buffer layer in this work. In conclusion, this study did not discuss the additional strain from the buffer to QWs. The Al composition in the buffer layer and the QB are the same in this work. In addition, the influence of the strain in QW, which is applied by the buffer layer, has been discussed in the paper [23].

doi:10.6342/NTU202303083

3.2 The influence of the strain-induced deformation potential

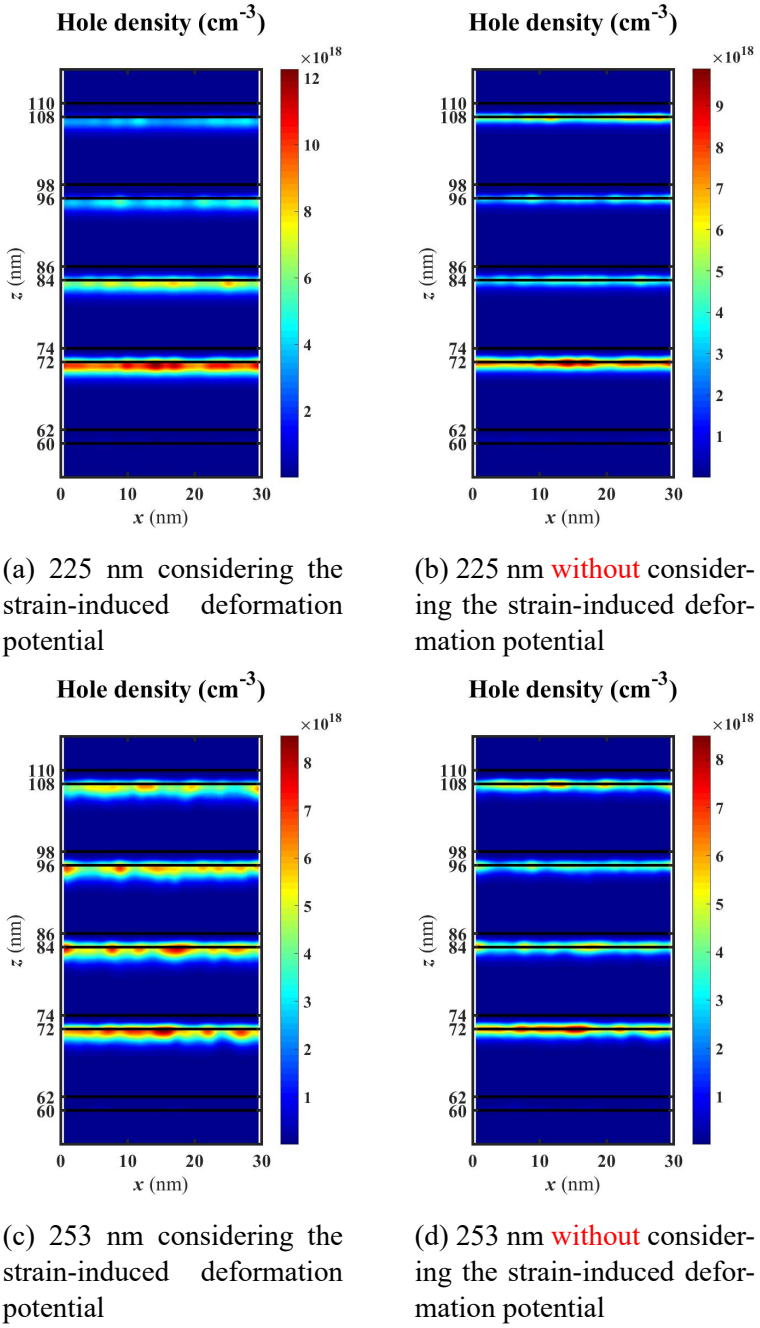

(a) 225 nm considering the strain-induced deformation potential

(b) 225 nm without considering the strain-induced deformation potential

(c) 253 nm considering the strain-induced deformation potential

(d) 253 nm without considering the strain-induced deformation potential

Figure 3.2: The hole density distribution of the active region in 225 nm and 253 nm with and without considering the random alloy fluctuation cases.

doi:10.6342/NTU202303083

The hole carrier in the QB region will increase after considering the strain-induced deformation potential in the LL model, as shown in Fig. 3.2. In brief, the QW for holes will be shallower due to the strain-induced deformation potential. The detail will be discussed in Chapter 5.2.2.3

Therefore, including the strain-induced deformation potential in the band structure calculation is essential and makes the calculation more precise in predicting the carrier density distribution of the LL model.

3.3 The comparison of the strain-induced localization landscape model with and without the k·p method

As mentioned above, the strain-induced deformation potential LL model will output the 3-band information induced by strain. Similarly, the k·p method uses to calculate the 3-band position.[17, 22, 35–39] Theoretically, the k·p method could be removed or calculated at the end for final confirmation after the computation of the strain-induced deformation potential LL model. The iteration step can neglect the k.p method.

3.3.1 Polarization ratio

To explain the simulation result of the strain-induced deformation potential LL model without the k·p method is credible, namely, whether the output of the 3-band position or its related physical quantity has a similar tendency under the strain-induced deformation potential LL model with and without the k·p method. According to the polarization ratio value calculation is related to the three-band potential, comparing the polarization ratio

doi:10.6342/NTU202303083

result can tell the credibility of the strain-induced deformation potential LL model without the k·p method.

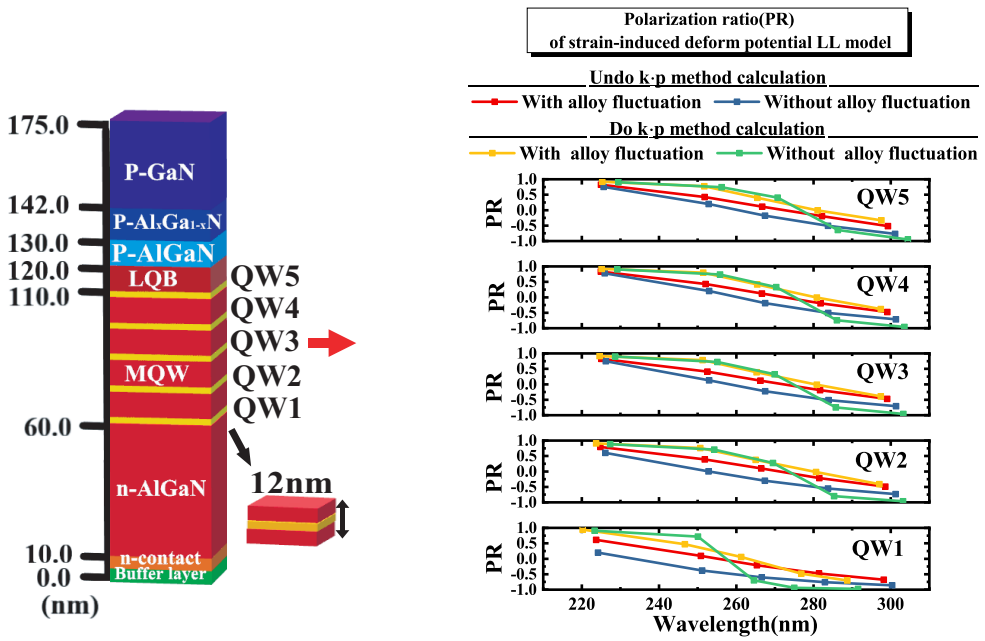

(a) simulation structure (b) Polarization ratio

Figure 3.3: (a) This work's schematic diagram of MQW structure. (b) Four lines are the polarization ratio value in different wavelengths at different QWs solved by the strain-induced deformation potential LL model. The red and blue lines are with and without random alloy fluctuation cases without the k·p method calculation. The yellow and green lines are with and without random alloy fluctuation cases with the k·p method calculation.

Basically, in each QW, the polarization ratio in different wavelengths solved by the strain-induced deformation potential LL model without the k·p method has a similar tendency to with k·p method calculation, whether with or without considering the random alloy fluctuation cases, shown in Fig. 3.3 (b). Then, the analysis of Fig. 3.3 is in the following.

For the electron injection, the structure design of this work has the n-type dopant in the first QB (QB1). The first QB means the QB closest to the n-contact one; see Fig. 3.3 (a). Hence, the shape of the band structure in the first QW (QW 1) is quite different from other QWs (QW 2, QW3, QW 4, QW 5). Furthermore, when the shape of the band struc-

doi:10.6342/NTU202303083

ture changes, the influence will include widely, like the carrier distribution, wave function distribution, wave function overlap, and polarization value. That is why the polarization tendency of QW 1 is relatively different from other QWs.

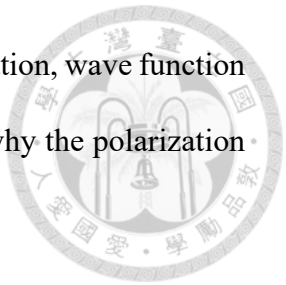

According to the magnitude of radiative recombination in different quantum, the averaging polarization ratio can be calculated by Eq. (3.3).

$$\mathrm{PR_{Avg}} = \frac{Rad_{\mathrm{TM,Total}} - Rad_{\mathrm{TE,Total}}}{Rad_{\mathrm{TM,Total}} + Rad_{\mathrm{TE,Total}}}, \tag{3.1}$$

$$Rad_{\mathrm{TM,Total}} = \sum_{n=1}^{5} Rad_{\mathrm{QW}_n,\mathrm{TM}}, \tag{3.2}$$

$$Rad_{\mathrm{TE,Total}} = \sum_{n=1}^{5} Rad_{\mathrm{QW}_n,\mathrm{TE}}, \tag{3.3}$$

where the $\mathrm{PR_{Avg}}$ is the average polarization ratio in MQW, $Rad_{\mathrm{TM,Total}}$ is the total TM polarized radiative recombination in MQW, $Rad_{\mathrm{TE,Total}}$ is the total TE polarized radiative recombination in MQW, $Rad_{\mathrm{QW\ 1,TM}} \sim Rad_{\mathrm{QW\ 5,TM}}$ are the TM polarized radiative recombination in QW 1 to QW 5, $Rad_{\mathrm{QW\ 1,TE}} \sim Rad_{\mathrm{QW\ 5,TE}}$ are the TE polarized radiative recombination in QW 1 to QW 5.

doi:10.6342/NTU202303083

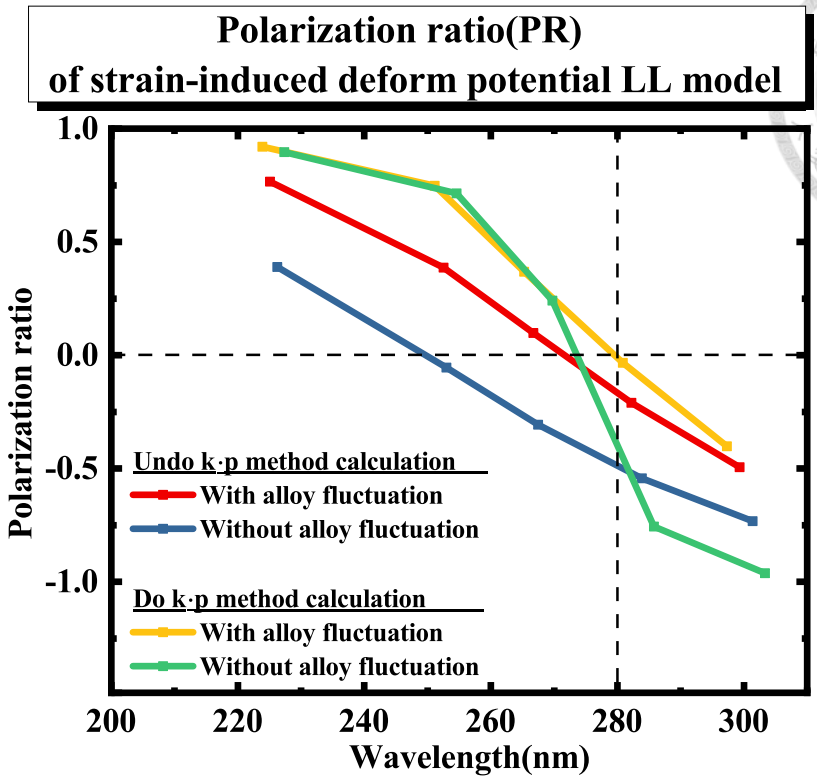

Figure 3.4: Four lines are the averaging polarization ratio value in different wavelengths solved by the strain-induced deformation potential LL model. The red and blue lines are with and without random alloy fluctuation cases without the k·p method calculation. The yellow and green lines are with and without random alloy fluctuation cases with the k·p method calculation.

The polarization ratio is calculated by the TM-polarized and TE-polarized light emission, as shown in Eq. (2.97). The EL intensity in this study is calculated by the spontaneous light emission from the recombination and generation of electron-hole pairs, as shown in Eq. (2.96). Therefore, the corresponding valance band of the hole will directly influence the polarization of the light emission. [15, 22] Note that the splitting of the $|X \pm iY\rangle$ and $|Z\rangle$ state dominant band will significantly influence the wave function overlap and their polarization ratio value that will be analyzed afterward.

The following introduces the potential shape difference between the strain-induced deformation potential LL model and the k·p method.

The shapes of the band structure solved by the strain-induced deformation potential

doi:10.6342/NTU202303083

LL model and the k·p method are different. In the QW region, the potential profile in the k·p method is sharper in the boundary of the QW and linear inside the QW region. On the contrary, the strain-induced deformation potential LL model's potential shape will be the valley profile[47] because the quantum confinement effect will imply the carrier distribution on the other side.[40] Additionally, the study in 2017 stated that for the infinite medium with identical material composition and a parabolic band whose minimal energy would be the effective confinement potential $W(\vec{r})$ in the LL model[47].

In the wurtzite GaN crystal, the crystal orientation will cause in-homogeneous polarization.[15–17] In the QW region, the piezoelectric field, which causes strong quantum confined Stark effect (QCSE), will tilt the band structure and let the electrons and holes wave function separated.[2, 16, 27] Therefore, the quantum confinement and the carrier distribution in the QW region will change by the internal electric field. As mentioned above, the strain-induced deformation potential LL model considers the quantum confinement effect. Therefore, the shape of the potential in the strain-induced deformation potential LL model is valley-like and tilts its valley to the minimum of the tilted band structure caused by the internal electric field. .[4, 47]

Above is the analysis of why the potential shapes differ in the strain-induced deformation potential LL model and the k·p method. The study of how the splitting in $|Z\rangle$ and $|X \pm iY\rangle$ state dominant band influences the polarization ratio value afterward.

In the QW regions, the splitting of the different Eigenvalues is fixed under the quantum model of the k·p method. However, the splitting of $|Z\rangle$ and $|X \pm iY\rangle$ state dominant band in the QW regions is not the constant value under the strain-induced deformation potential LL model as the effective potential of the strain-induced deformation potential

doi:10.6342/NTU202303083

LL model includes the quantum confinement effect. Therefore, the effective potential of it could calculate the carrier density under the carrier confinement effect.[40, 41, 46, 47] Additionally, the carrier density is related to the energy difference between the potential and Fermi-level energy. The changing of the splitting between $|Z\rangle$ and $|X \pm iY\rangle$ state dominant band in the QW regions will reflect the carrier density from the side. Hence, the influence is that the polarization ratio is not a definite value in different positions of the QW region. Namely, the polarization ratio value will be averaged in the strain-induced deformation potential LL model. Therefore, the green line is sharper than the blue line in Eq. (3.4).

In conclusion, because the splitting of $|Z\rangle$ and $|X \pm iY\rangle$ state dominant band in the QW regions is not the constant value, the polarization ratio value will be average in the strain-induced deformation potential LL model. Further information about the influence of random alloy fluctuation in polarization will be mainly discussed in Chapter 5.1

3.4 Summary

Owing to the trend of polarization ratio being similar in strain-induced deformation potential LL model with and without the k·p method, using the modified LL model is more efficient and provided enough information for device design. The calculation time can save around 47 hours per step under the simulation structure of this work, as shown in Table 3.7.

The dominant light emission will change from TE to TM polarized light when the polarization value equals zero. Namely, the light emission will switch from TM to TE-polarized light at ∼280 nm in this work.

doi:10.6342/NTU202303083

The potential shape of the strain-induced deformation potential LL model is valley-like and tilted by the quantum confined Stark effect (QCSE). The splitting of $|Z\rangle$ and $|X \pm iY\rangle$ state dominant band in the QW regions is not the constant value, so the LL model's polarization ratio value will be average. Furthermore, the effective potential with the quantum confinement effect in the LL mode could can be used to the carrier density more precisely.

Table 3.7: The calculation time in different solver

Solver	Calculation time
Poisson drift-diffusion strain-induced deformation potential LL solver	$\simeq$ 48 minus/step
k·p method	$\simeq$ 47 hours/step

doi:10.6342/NTU202303083

doi:10.6342/NTU202303083

Chapter 4 Analyzing the performance of the optimized epitaxial structure in 225 nm and 253 nm UVC-LEDs

4.1 Overview

This work will improve the performance of UVC-LEDs by optimizing the epitaxial layer design. The most important thing before the optimization is knowing the problem with UVC-LEDs and the chance to improve their performance. Hence, the following will introduce problems in UVC-LED and the epitaxial layer design that can improve the issues.

The p-type doping is the method to increase the injection of hole density.[12, 58, 59] However, the ionization energy of AlGaN material is quite large and increases with the larger Al composition.[58] That means the hole injection from the p-AlGaN layer is low. Moreover, AlGaN alloy material with a high Al composition will have many defects, influencing the material's doping concentration and light extraction.[3] The experimental result shows that at the peak of the impurity emission from the Mg dopant, the emission

doi:10.6342/NTU202303083

energy is closest to the band edge, caused by the vacancy defect in the Mg dopant.[58] Due to the defect of the nitrogen-vacancy with three positive charges V_N^{3+} in the band structure act as the deep donor energy level, the relatively smaller energy to transition will let the V_N^{3+} more easily capture the holes in free.[60] In brief, under the p-type dopant by Mg, the ionized hole carrier will be captured by the V_N^{3+} and decrease the free hole density injection to the doping region.

The problem of electron carrier overflow will be more severe in the smaller emission wavelength cases, such as UVC-light. Due to the higher activation energies in AlGaN material with high Al composition will lower the injection of hole carrier density to the active region, the hole carriers are not sufficient to recombine with the electrons. If the barrier can not block the electron carrier, the overflowing electron will recombine with the holes in the p-AlGaN layer and cause the leakage current. [9] Therefore, the droop effect will reduce the radiative recombination efficiency by the severe carrier overflow when the current density increases.[61] Additionally, the heat generated from current crowding will influence the lifetime of LEDs due to the lifetime of LEDs is related to the operating temperature of it. [9, 62, 63]

According to the above issue, the epitaxial layer design will focus on improving the hole carrier injection and decreasing the electron overflow to increase the wall plug efficiency. Based on the Al composition difference between the QB and the QW region will directly influence the carrier confinement in the active region.[49, 64] The Al composition in the QB region might be the critical factor leading to the electron carrier overflow. (It is thoroughly investigated in Chapter 5.2.1.) Namely, this work will do the optimization by changing the Al composition of the QB layer to decrease the electron carrier overflow first. Additionally, to further decrease the electron carrier overflow, optimizing the p-AlGaN

doi:10.6342/NTU202303083

layer, which inhibits the electron carrier overflow to the p-AlGaN layer, will be done after optimizing the Al composition of the QB region. [4, 9]

4.2 The optimization of the epitaxial structure in quantum barriers and electron-blocking layer

4.2.1 The optimization of the quantum barriers

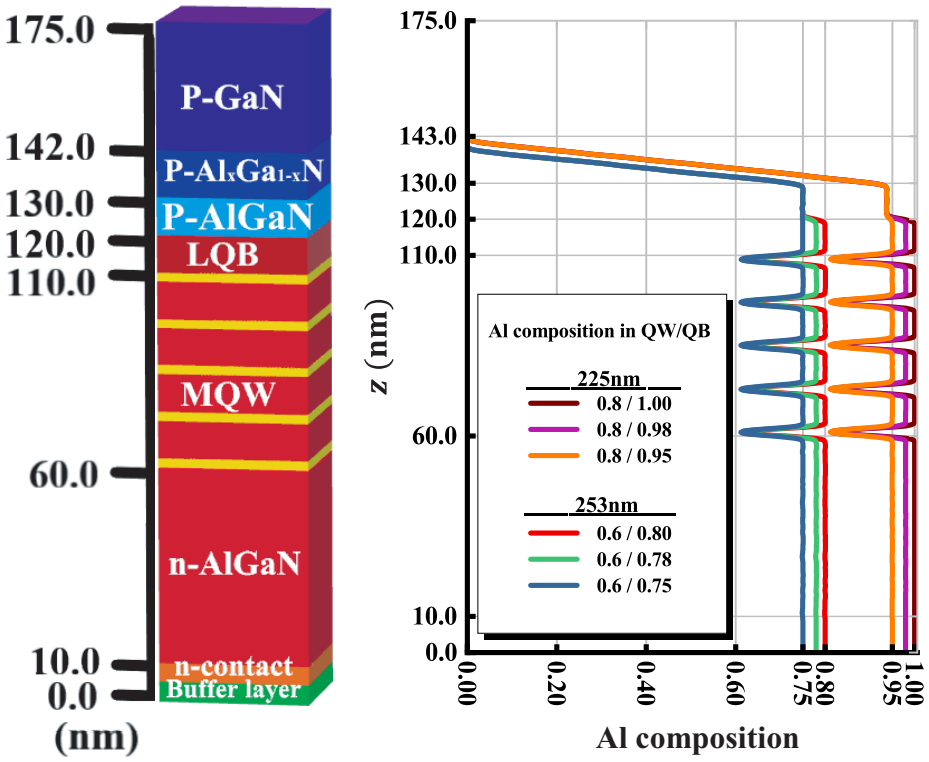

Figure 4.1: Considering the random alloy fluctuation, the Al composition map in 225 nm and 253 nm under different quantum barrier cases.

Since the depth of the QB will be closely related to the IQE by the efficiency of the carrier confinement.[49, 64] In the simulation design, we fix the Al composition in QWs and change the Al composition in QBs. The Al composition difference between the QW

doi:10.6342/NTU202303083

and the QB will vary from 0.2 to 0.15 at around 225 nm and 253 nm cases. The details of the simulation parameter in 225 nm and 253 nm are in Table 3.1, Table 3.2, and Table 3.3.

Having defined the design of the optimization simulation, the following will analyze the simulation result of the current density to voltage plot, radiative recombination, and their wall-plug efficiency (WPE).

4.2.1.1 J-V plot and band structure

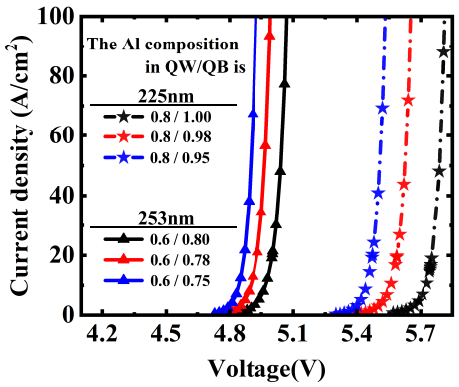

(a) The J−V plot

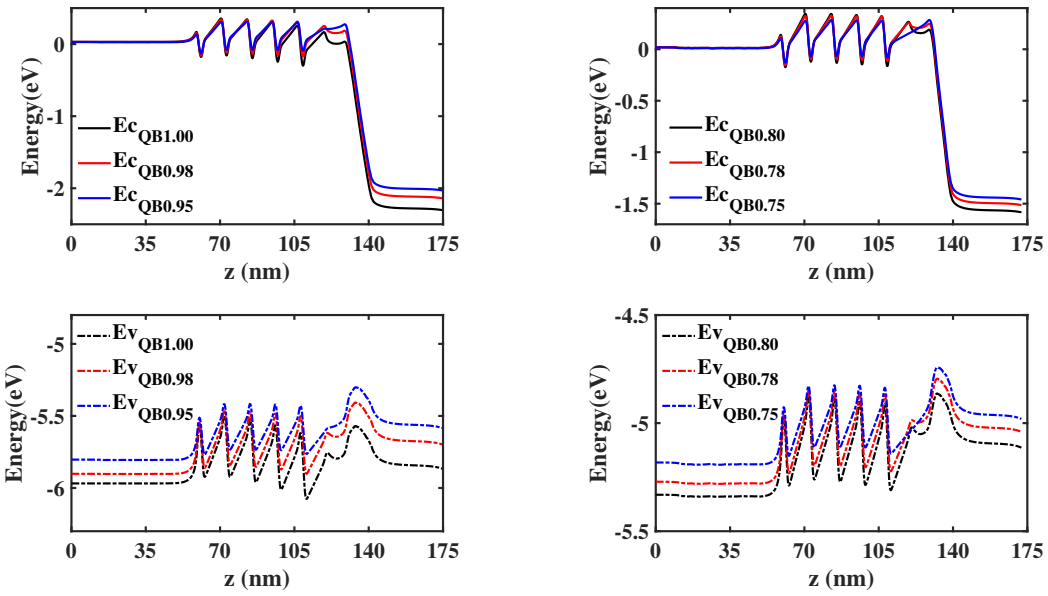

(b) The band structure of 225 nm (c) The band structure of 253 nm

Figure 4.2: (a) is the J−V curve of 225 nm and 253 nm with random alloy fluctuation cases. (b) and (c) are the band structure of 225 nm and 253 nm with random alloy fluctuation cases at the current density ≃ 20 (A / cm^2).

doi:10.6342/NTU202303083

Due to the larger band gap of 225 nm in the active region, in the 225 nm case, the turn-on voltage, which is the operating voltage under the current density around 20 (A/cm^2), is larger than in 253 nm cases, shown in Fig. 4.2(a). When the Al composition difference between QW and QB decreases, the lower potential barrier at the QW and QB interface causes the shallower QW, letting the carrier confinement decrease in the QW region. Therefore, the improvement of the carrier transport will decrease the turn-on voltage.

Moreover, the lower Al composition in the QB region will decrease the spontaneous polarization in the QB region and the piezoelectric polarization induced by lattice mismatch between the QW and QB interface.[65] The lattice mismatch cause the tilted band structure in QW will more flatten. Therefore, the part of the turn-on voltage that needs to increase the current density by flattening the band structure will decrease.

Additionally, the decrease of the turn-on voltage in 225 nm is more significant than 253 nm under the difference of the Al composition change from 0.2 to 0.18 because the slope of the AlGaN band gap to Al compositions percentage in the material is not linear but increases with the larger Al composition.[66] Hence, under the difference of the Al composition change from 0.2 to 0.18, the decrease of the QB height will be more significant at 225 nm than 253 nm.

The higher barrier on the QB layer will make the deeper conduction and valance bands for electrons and holes, as shown in Fig. 4.2(b) and Fig. 4.2(c). Hence, the carrier confinement in the active region will improve with the design of the higher barrier on the QB layer.

doi:10.6342/NTU202303083

4.2.1.2 Internal quantum efficiency

The following analysis of why the Al composition difference between the QW and QB region with 0.2 is the best optimization design of the QB epitaxial layer in this study.

The droop effect is the phenomenon of radiative recombination decreasing with the current density increasing.[61] The droop effect will appear when the current density increase due to the insufficiency of hole carrier injection under the high activation energy in p-dopant AlGaN.[9] Therefore, the electron carriers will not fully recombine with the hole carriers, and the efficiency of the electron carriers overflowing to the p-AlGaN will become severe.

Based on the high activation energy in AlGaN material with high Al will lower hole injection, the influence of three particle interaction caused Auger recombination will decrease because of whether the two electrons with one hols or the two holes with one electron need the hole carrier. Therefore, when the current density increase, the change in the loss of the Auger recombination is small in different cases of 225 nm and 253 nm.[2, 9]

doi:10.6342/NTU202303083

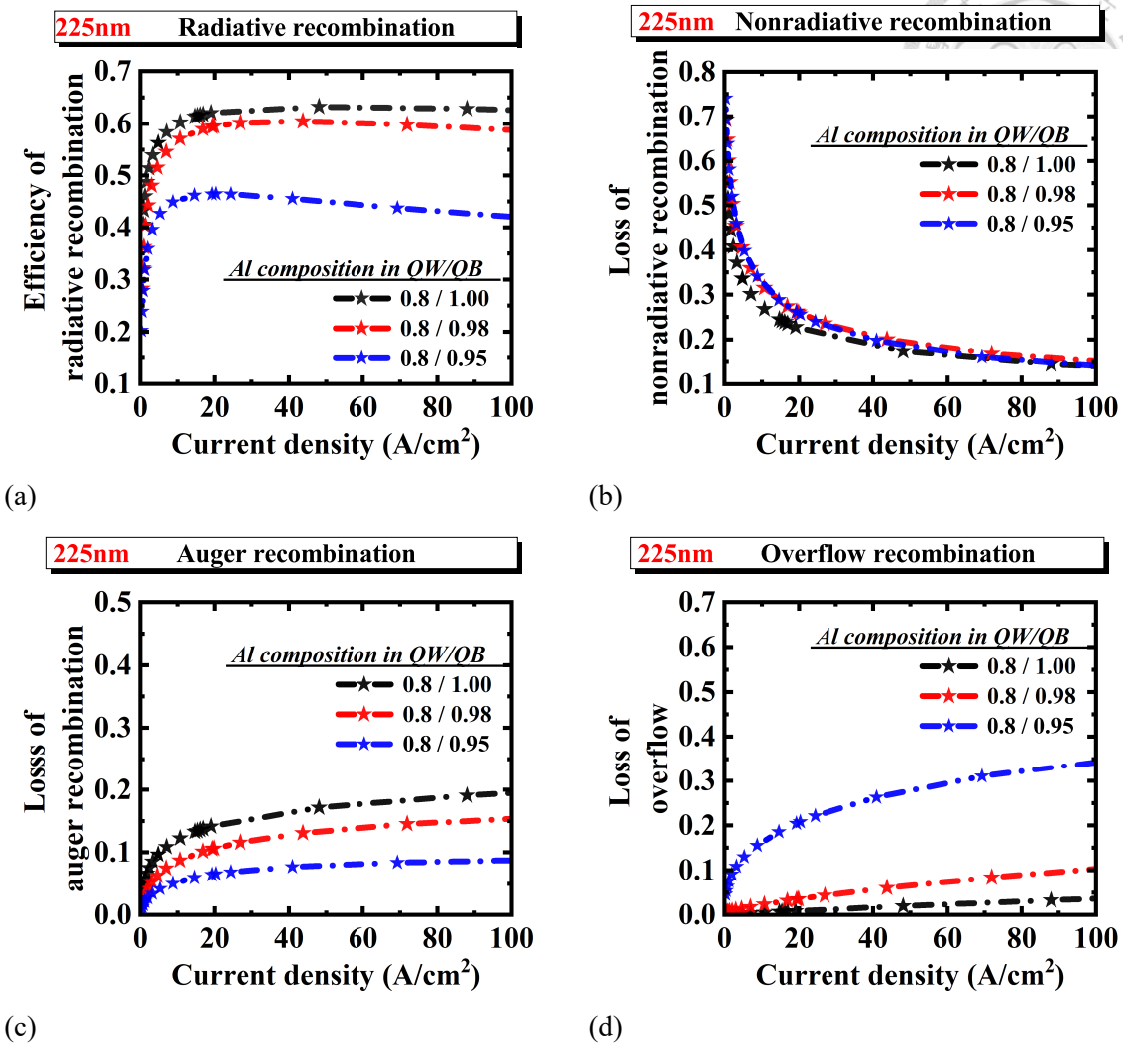

Figure 4.3: The comparison of different QB cases' efficiency of radiative recombination, nonradiative recombination, auger recombination, and overflow at around 225 nm considering random alloy fluctuation.

doi:10.6342/NTU202303083

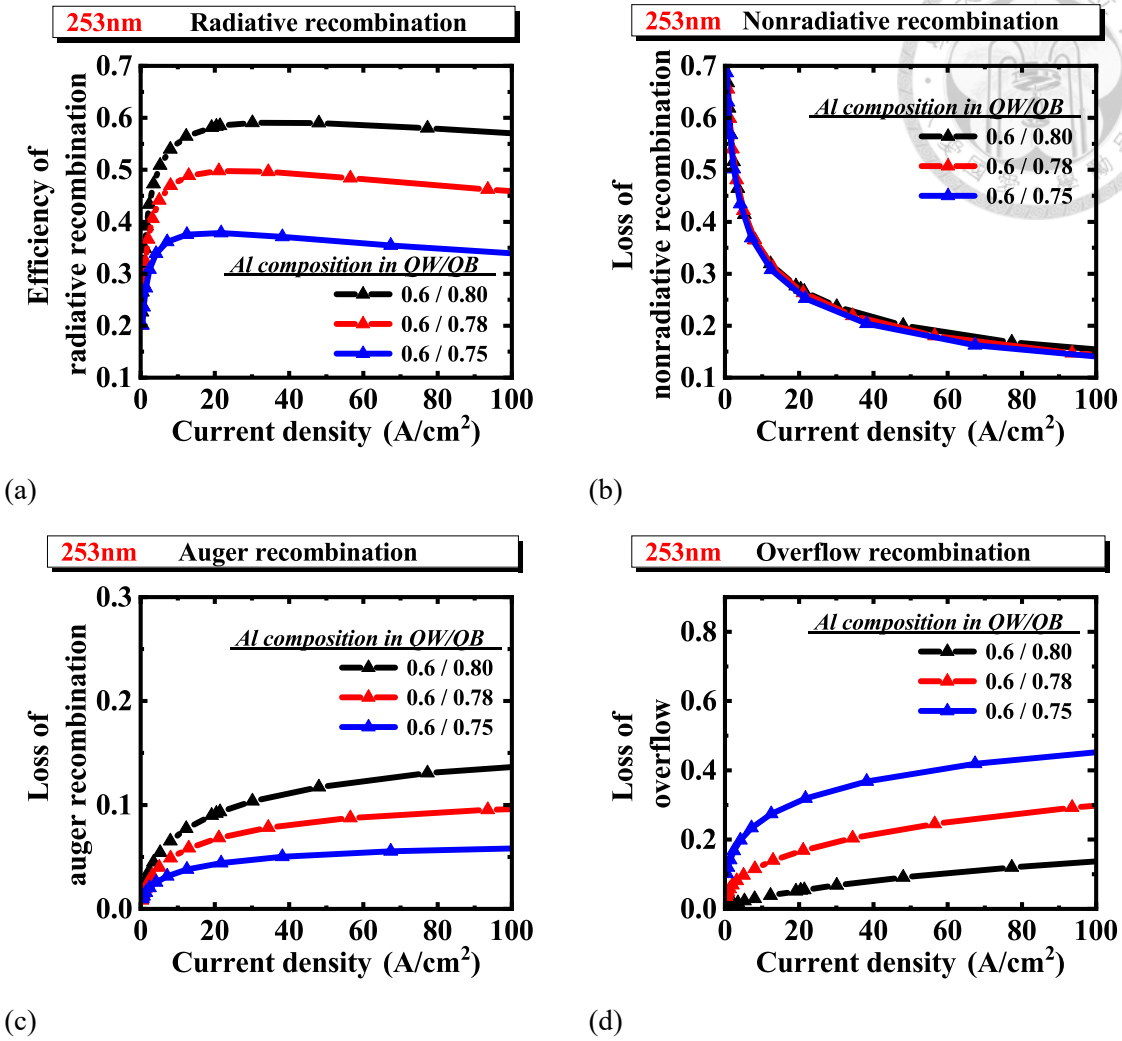

Figure 4.4: The comparison of different QB cases' efficiency of radiative recombination, nonradiative recombination, auger recombination, and overflow at around 253 nm considering random alloy fluctuation.

4.2.1.3 Current density

After seeing that the carrier overflow will be improved by designing the higher barrier on the QB layer, knowing whether the carrier overflow is from electrons or holes is essential. As shown in Fig. 4.5 and Fig. 4.6, for the higher QB cases, the electron carrier overflow can effectively inhibit.[49, 64] Additionally, the higher QB will decrease the hole carrier injection. However, the influence of the improving carrier confinement is more significant in the blocking of hole injection, as shown in Table 4.1. Hence, reducing

doi:10.6342/NTU202303083

electron carrier overflow is the main reason for increased radiative recombination under the higher QB cases.

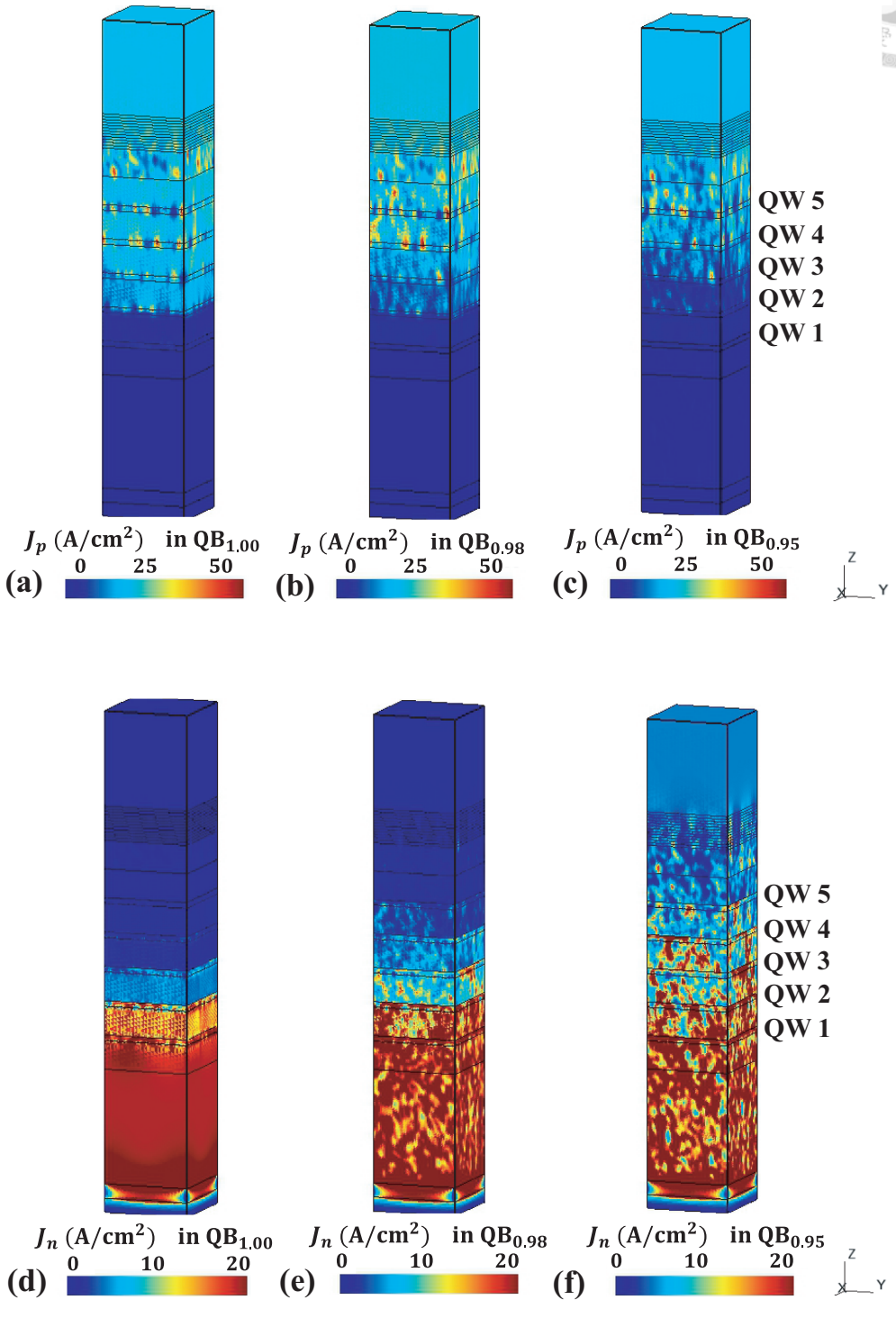

Figure 4.5: (a), (b), and (c) are the hole current density distribution of different QB in 225 nm with random alloy fluctuation cases. (d), (e), and (f) are the electron current density distribution of different QB in 225 nm nm with random alloy fluctuation cases.

doi:10.6342/NTU202303083

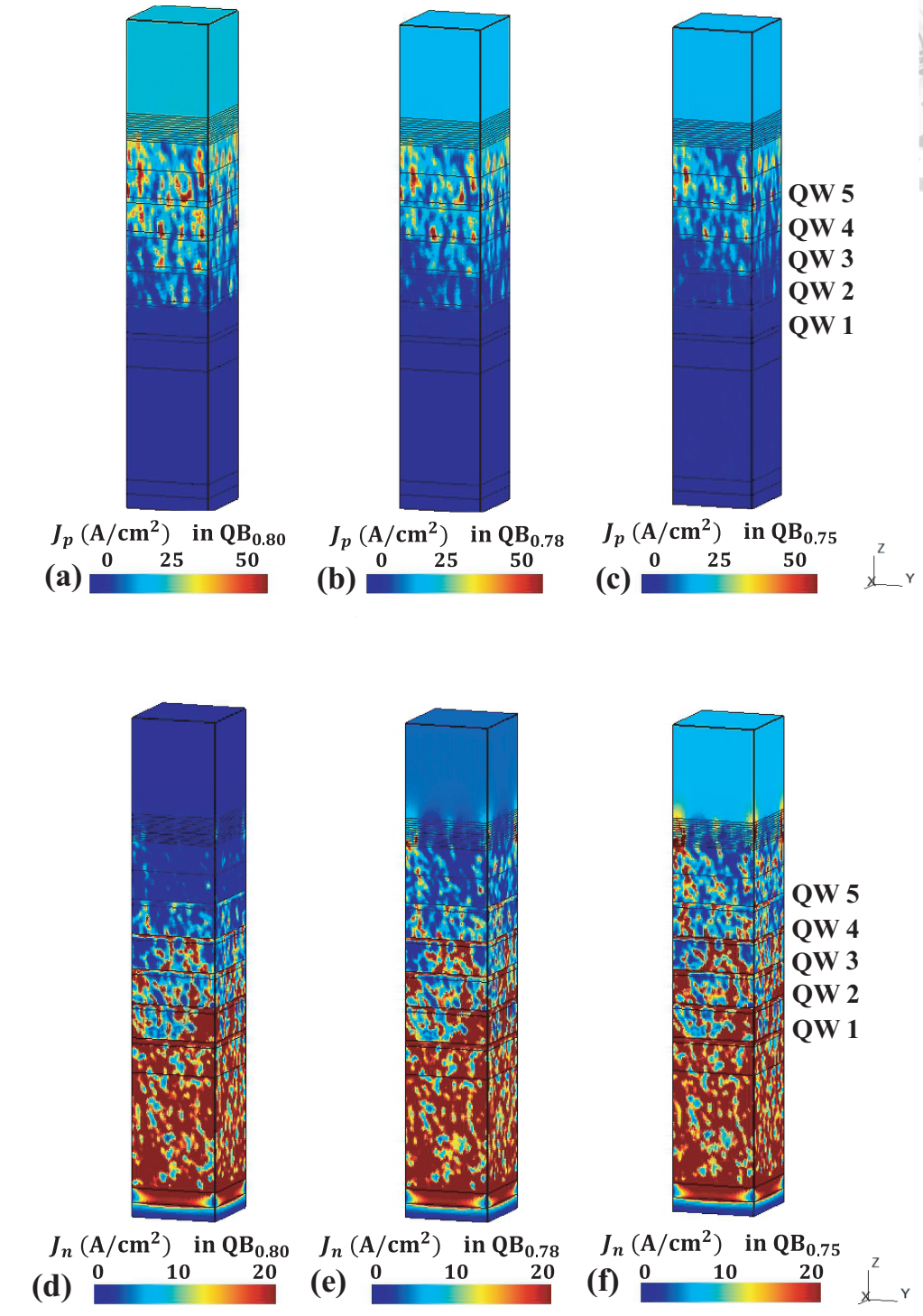

Figure 4.6: (a), (b), and (c) are the hole current density distribution of different QB in 253 nm with random alloy fluctuation cases. (d), (e), and (f) are the electron current density distribution of different QB in 253 nm with random alloy fluctuation cases.

doi:10.6342/NTU202303083

Table 4.1: The loss of the carrier overflow $\simeq$ 20 (A / cm^2) in optimized QB cases.

wavelength	225 nm	226 nm	227 nm	253 nm	253 nm	255 nm
Loss \ Δ Al	0.2	0.18	0.15	0.2	0.18	0.15
Electron overflow	0.009	0.036	0.208	0.054	0.169	0.319
Hole overflow	0.002	0.002	0.005	0.001	0.002	0.006

In Table 4.1, the calculation of the loss by electron and hole carrier overflow is calculated by the below formula,

$$\text{Electron carrier overflow} = \frac{J_{n_{\text{p-contact}}}}{J_{n_{\text{p-contact}}} + J_{p_{\text{p-contact}}}}, \tag{4.1}$$

$$\text{Hole carrier overflow} = \frac{J_{p_{\text{n-contact}}}}{J_{p_{\text{n-contact}}} + J_{n_{\text{n-contact}}}}, \tag{4.2}$$

Additionally, the emission wavelength in different QB cases will shift a little bit by the strain-caused polarization field in QW is different.

In conclusion, the decrease in electron carrier overflow is the main reason for the better radiative recombination efficiency under the higher Al composition difference between the QW and QB[49, 64]. In the simulation structure of this work, the maximum value of radiative recombination has the largest value and the minor droop effect when the Al composition difference between QWs and QBs is 0.2, whether in 225 nm or 253 nm.

4.2.1.4 Wall plug efficiency

The wall plug efficiency (WPE) can evaluate the efficiency from the optical output power of the LED system to the operating input electrical power. The evaluation of the

doi:10.6342/NTU202303083

wall plug efficiency can be divided into three parts. One is the efficiency of each injection carrier from the device to the active region that could generate radiative light by the electron-hole pair spontaneous light emission in the active region (IQE). Another is the loss of the radiative light emission from generating to output the system (light extraction efficiency (LEE)). The other is the efficiency of the electron carrier injected into the device under the operation voltage (electron injection efficiency (EIE)).[4]

$$\text{WPE} = \frac{P_{\text{rad}}/\hbar\omega}{I_{\text{injection}}/e} \times \frac{P_{\text{rad,output}}}{P_{\text{rad}}} \times \frac{\hbar\omega}{eV_{\text{op}}}, \tag{4.3}$$

$$= \text{IQE} \times \text{LEE} \times \text{EIE}, \tag{4.4}$$

where the P_{rad} and $I_{\text{injection}}$ are the power of spontaneous radiative recombination emission in the active region and the current injection to the active area, the ω is the angular frequency of the radiative emission in the active region, the meaning of $P_{\text{rad,output}}$ is the radiative recombination output power of the system, and the V_{op} is the operating voltage.

The light extraction efficiency (LEE) of AlGaN-based UVC-LEDs is less than 10 %[4, 13, 18, 67, 68] due to the sizeable light absorption from the p-GaN contact layer and the propagation direction of the light emission. Furthermore, the p-GaN layer on the top of the structure is the current crowding layer and has contact resistance.[67] Therefore, the light absorption problem in p-GaN will influence the light extraction efficiency (LEE) a lot. This study calculates the Wall plug efficiency (WPE) by setting the light extraction efficiency (LEE) is 10 % to evaluate the efficiency of different cases from the optical output power of the LED system to the operating input electrical power.

doi:10.6342/NTU202303083

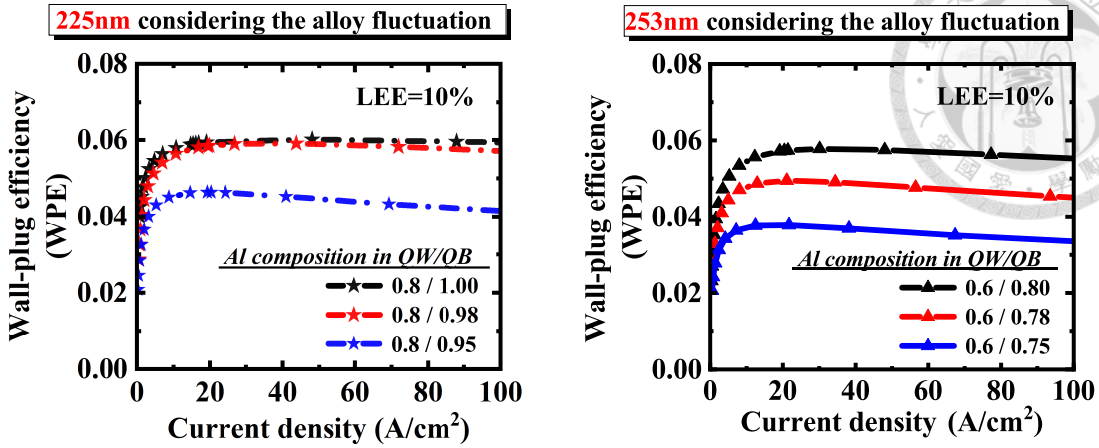

(a) 225 nm (b) 253 nm

Figure 4.7: The wall-plug efficiency (WPE) in different current densities of different QB cases considering random alloy fluctuation.

Table 4.2: The performance of different Al compositions between the QB and QW at the current density $\simeq$ 20 (A / cm^2).

wavelength	225 nm	226 nm	227 nm	253 nm	253 nm	255 nm
Efficiency \ Δ Al	0.2	0.18	0.15	0.2	0.18	0.15
V_{op} (V)	5.755	5.587	5.473	5.003	4.930	4.870
IQE	0.620	0.595	0.464	0.583	0.498	0.378
LEE	0.100	0.100	0.100	0.100	0.100	0.100
WPE	0.059	0.058	0.046	0.057	0.049	0.037

Under the setting of the light extraction efficiency (LEE) is 10 %, in this study, the wall-plug efficiency (WPE) has the maximum value when the Al composition difference between QWs and QBs is 0.2, whether in the 225 nm or 253 nm of Fig. 4.7. The detail information of emission wavelength and the wall-plug efficiency (WPE) performance at the current density at around 20 (A/ cm^2) are listed in Table 4.2

In conclusion, the radiative recombination and wall-plug efficiency (WPE) has the maximum value when the Al composition difference between QW and QB is 0.2 at 225 nm

doi:10.6342/NTU202303083

and 253 nm as the carrier overflow in large current density will better inhibit. Hence, this study's best optimization design of the QB epitaxial layer is the Al composition difference between the QW and QB region with 0.2.

4.2.2 The improvement of the hole carrier injection

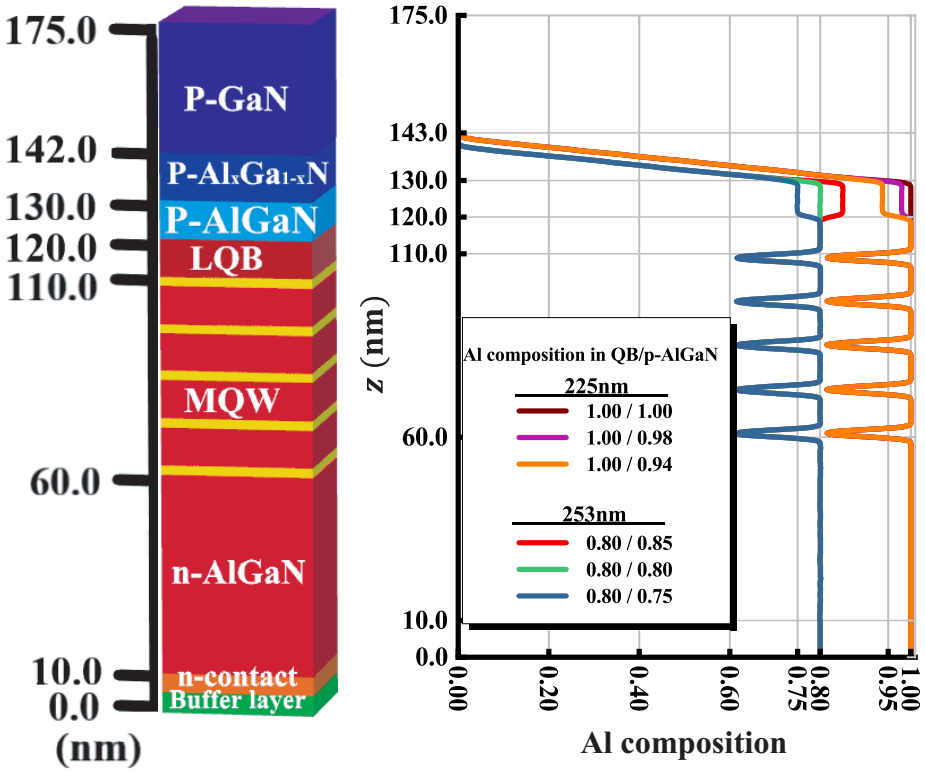

Figure 4.8: Considering the random alloy fluctuation, the Al composition map in 225 nm and 253 nm under different p-AlGaN layer cases.

Since the electron carrier overflow might be the critical factor in decreasing the IQE in UVC-LEDs due to the relatively small effective mass leading to larger mobility and the high activation energy for p-type dopant leading to insufficient hole injection than the electron.[9] Therefore, injecting the hole carriers recombine to electrons can avoid the carrier crossing the active region to the p-AlGaN layer is essential and helpful to the wall

doi:10.6342/NTU202303083

plug efficiency (WPE). In the simulation design, we fix the Al composition in QBs and change the Al composition in the p-AlGaN layer to increase the hole carrier injection.

Reiterate once again, the improvement of the hole carrier injection will be according to the best optimization design of the QB's epitaxial layer, which uses the Al composition difference between QW and QB with 0.2, whether in the 225 nm or 253 nm. In this section, the research does the simulation by designing the Al composition in the p-AlGaN layer with 1.00, 0.98, and 0.94 at 225 nm. For the 253 nm, the simulation design of Al composition in the p-AlGaN layer with 0.85, 0.80, and 0.75. The details of the simulation parameter in 225 nm and 253 nm are in Table 3.1, Table 3.2, and Table 3.3.

Having defined the design of the simulation, the following will analyze the simulation result of the current density to voltage plot, radiative recombination, and their wall-plug efficiency (WPE).

4.2.2.1 Band structure and current density

Fixing the Al composition in the last QB to adjust the p-AlGaN layer is the method that changes the polarization field between two layers. According to the lattice mismatch between the last QB and p-AlGaN layer, the polarization field will bend their band structure. The direction of bend bending induced by strain is related to the crystal orientation in wurtzite III-nitride material. [15–17] Furthermore, the thickness of the last QB and the p-AlGaN layer are the same in this study, as shown in Table 3.2 and Table 3.3.

doi:10.6342/NTU202303083

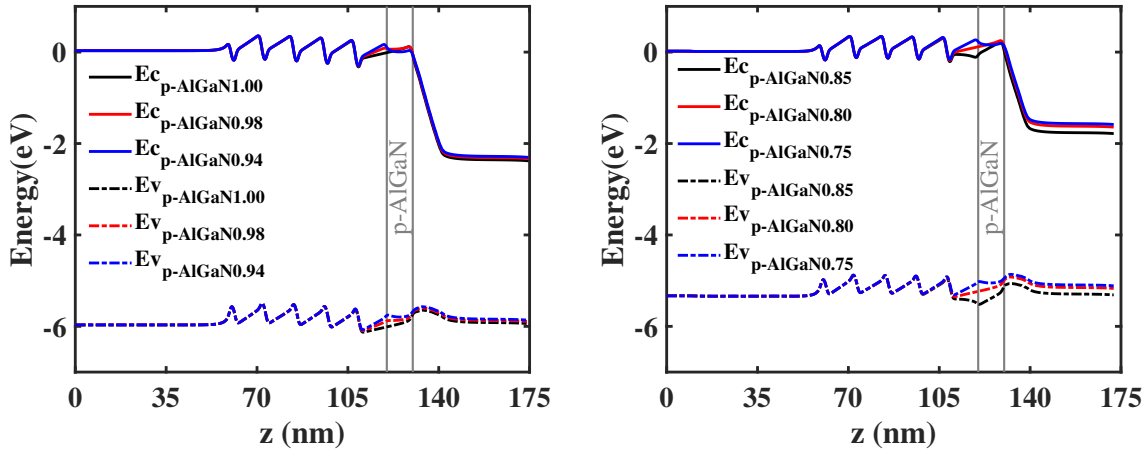

(a) The band structure of 225 nm (b) The band structure of 253 nm

Figure 4.9: (a) and (b) are the band structure distribution in 225 nm and 253 nm with random alloy fluctuation at the current density around 20 (A/cm^2).

However, in the case of the smaller Al composition in the p-AlGaN layer than the last QW, the intrinsic spontaneous polarization will be larger in the last QW than in the p-AlGaN layer. Therefore, the negative polarization charge will exist at the interface of the last QB and p-AlGaN layer, leading to a higher valance band.[24] Hence, the effective thickness of the barrier for holes will decrease, leading to the efficiency of hole carriers injection will increase by the tunneling effect.[4, 11]

To sum up that the higher effective barrier for electrons and holes will decrease the electron carrier overflow and hole carrier injection. However, reducing the barrier height will increase the electron carrier overflow and hole injection by the tunneling effect. Therefore, the following will analyze what mechanism influences the most in this study.

doi:10.6342/NTU202303083

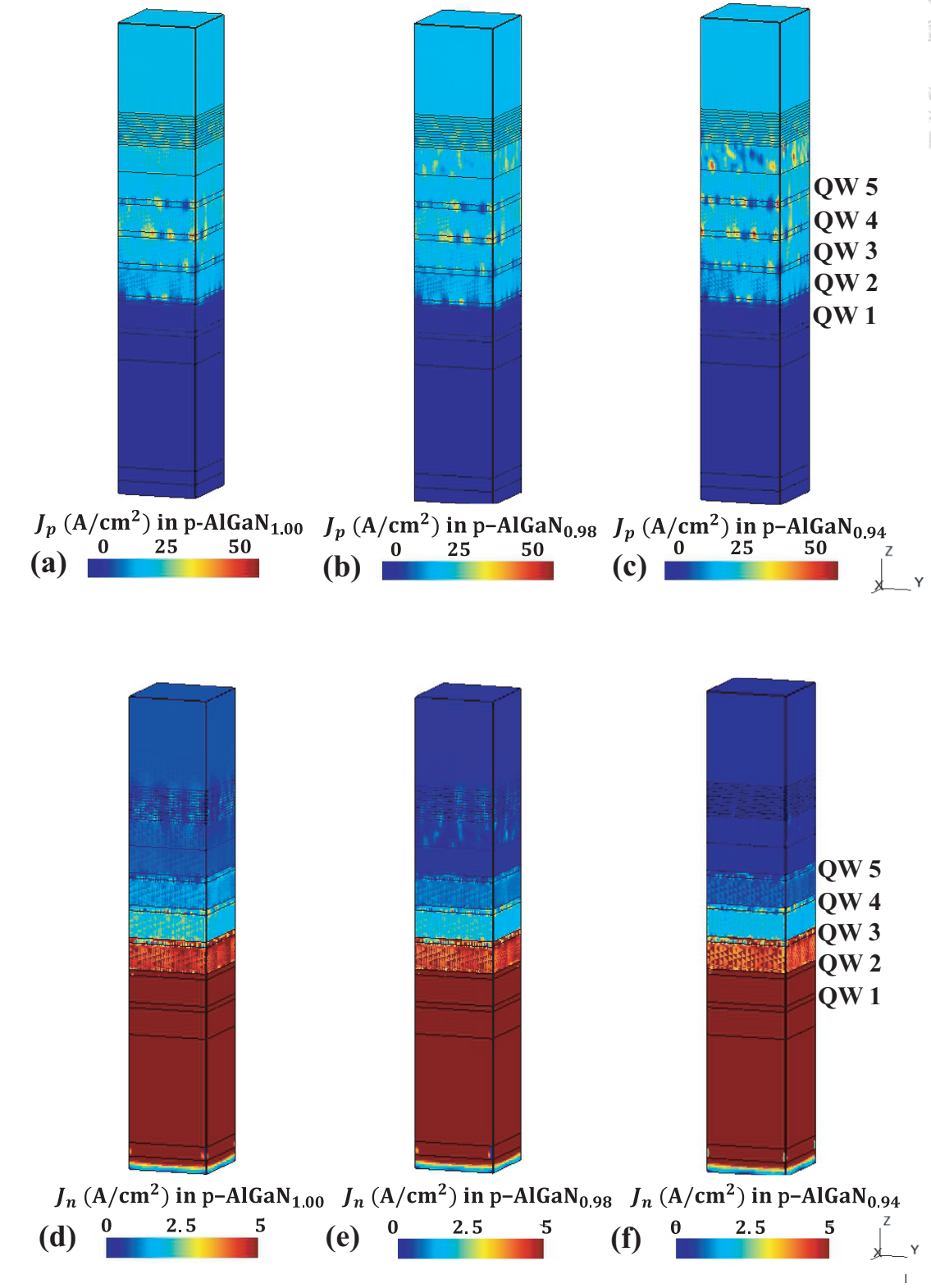

Figure 4.10: (a), (b), and (c) are the hole current density distribution of different p-AlGaN layers in 225 nm with random alloy fluctuation cases. (d), (e), and (f) are the electron current density distribution of different p-AlGaN layers in 225 nm nm with random alloy fluctuation cases.

doi:10.6342/NTU202303083

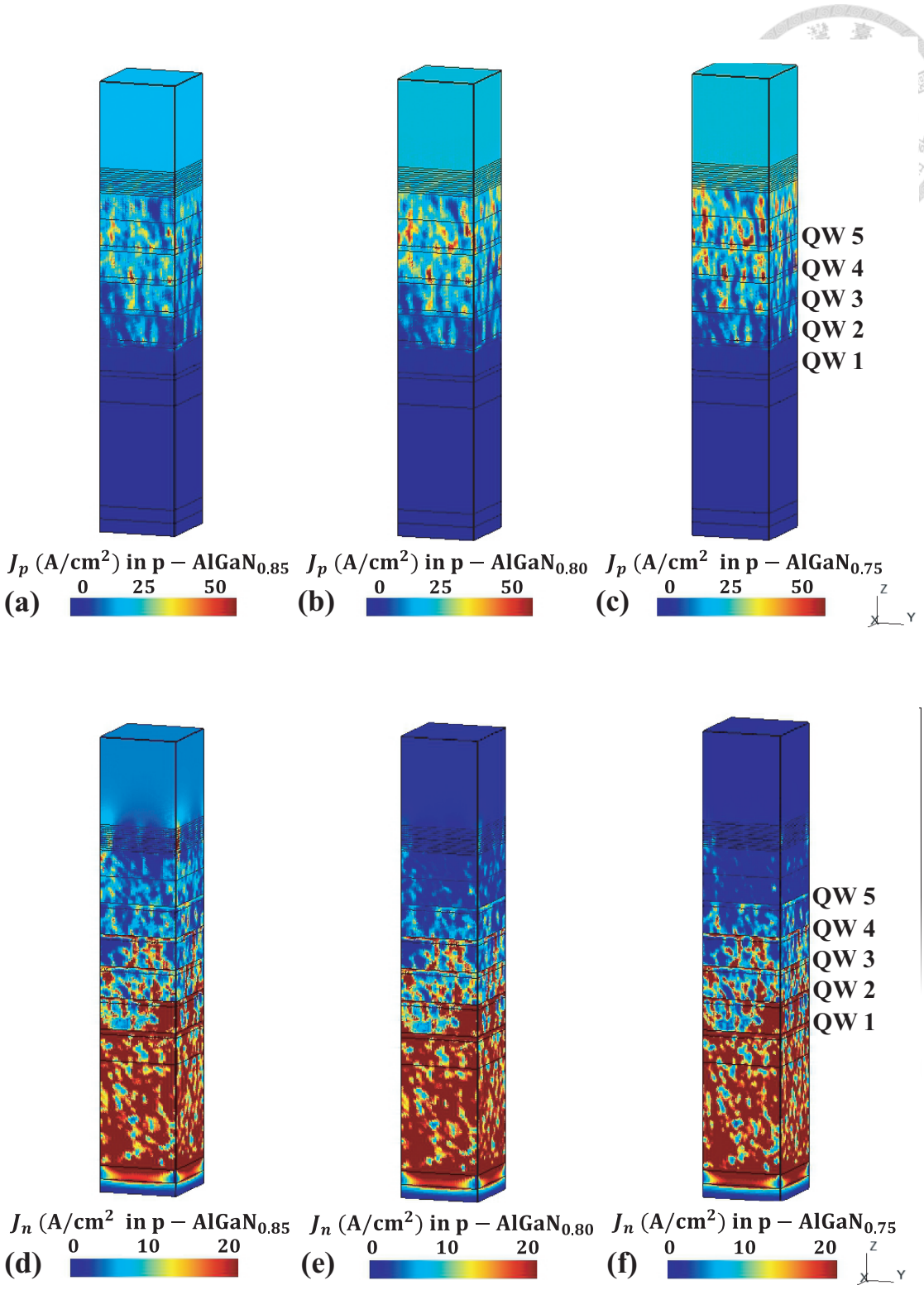

Figure 4.11: (a), (b), and (c) are the hole current density distribution of different p-AlGaN layers in 253 nm with random alloy fluctuation cases. (d), (e), and (f) are the electron current density distribution of different p-AlGaN layers in 253 nm with random alloy fluctuation cases.

doi:10.6342/NTU202303083

Due to the better hole carrier injection in the lower p-AlGaN layer case, the electron carrier will recombine with the increasing hole carrier before it overflows and leave the active region, as shown in Fig. 4.10 and Fig. 4.11.[9] Namely, the lower effective barrier case in the simulation design of this work, the increase of the hole carrier injection will decrease the electron carrier overflow. Therefore, decreasing the electron carrier overflow will improve the IQE and decrease the droop effect. [61]

Generally, people will build the EBL, the higher Al composition layer, in UVC-LEDs design to avoid the electron carrier overflow, leading to better IQE and avoiding the severe droop effect.[7, 24] However, in this work's lower Al composition's p-AlGaN design, the electron carrier overflow can be inhibited by the increasing hole carrier transport from the tunneling effect. In this work, there are two reasons the electron carrier overflow can inhibit by the p-AlGaN layer design. One is the design of QB had improved the electron carrier overflow in the previous work. The other is the hole carrier injection is better than expected due to the shallower QW for holes induced by the strain. The shallower QW for holes caused by the strain will be mainly discussed in Chapter 5.2.2[61]

4.2.2.2 J-V plot

In 225 nm, to flatten the band structure, the turn-on voltage, which is the operating voltage under the current density of around 20 (A/cm^2), must be larger due to the higher band gap and the larger band bending in the system. Additionally, the higher the Al composition in the p-AlGaN layer, the operating voltage will increase to flatten the increased polarization field.

doi:10.6342/NTU202303083

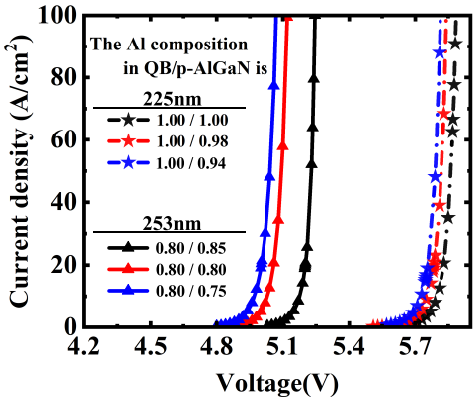

Figure 4.12: Considering the random alloy fluctuation, J−V plot in 225 nm and 253 nm under different p-AlGaN layer cases.

4.2.2.3 Internal quantum efficiency

As mentioned, the p-AlGaN layer with a lower Al composition case has better hole carrier injection, improving the electron carrier overflow. Hence, the radiative recombination efficiency is better, and the carrier overflow is lower when the p-AlGaN layer has a lower Al composition at 225 nm and 253 nm in this study, as shown in Fig. 4.13 and Fig. 4.14.

doi:10.6342/NTU202303083

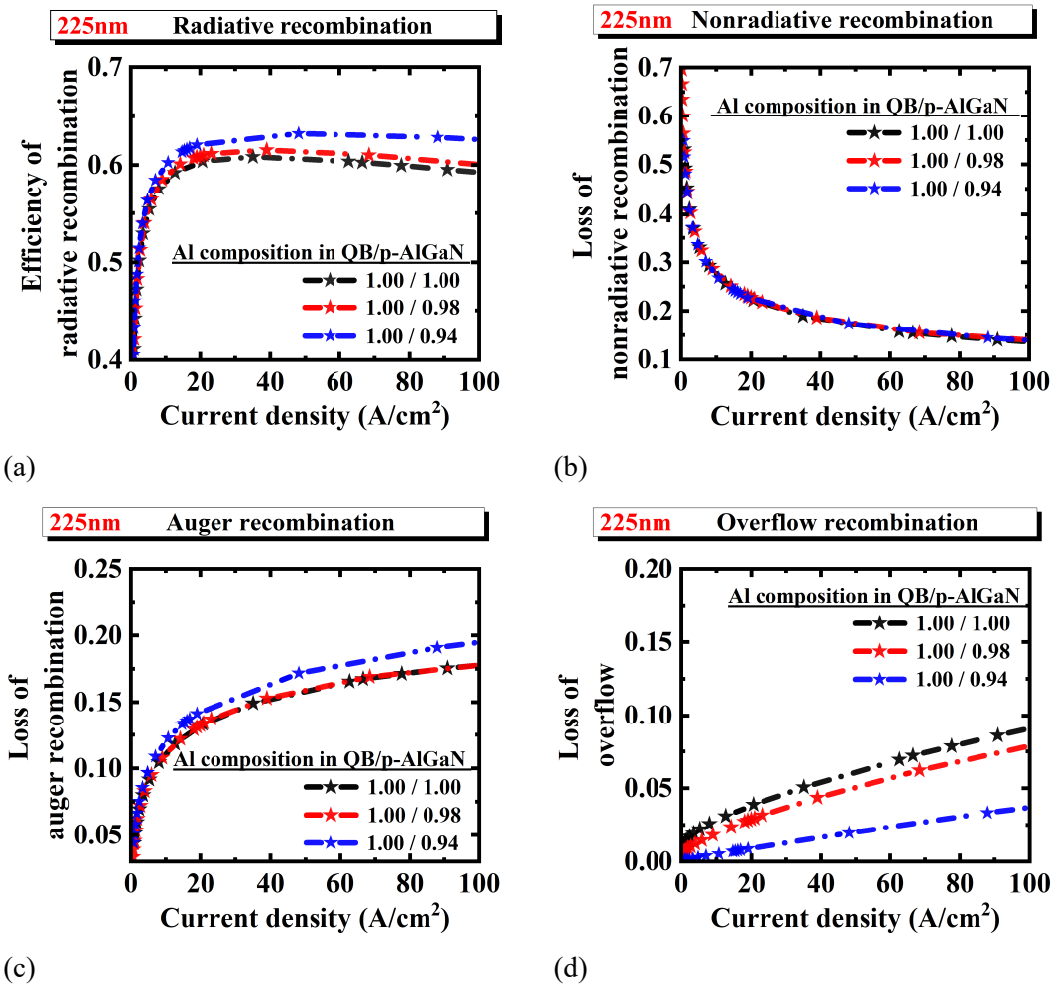

Figure 4.13: The comparison of different p-AlGaN layer cases' efficiency of radiative recombination, nonradiative recombination, auger recombination, and overflow to current density plot in 225 nm considering random alloy fluctuation.

doi:10.6342/NTU202303083

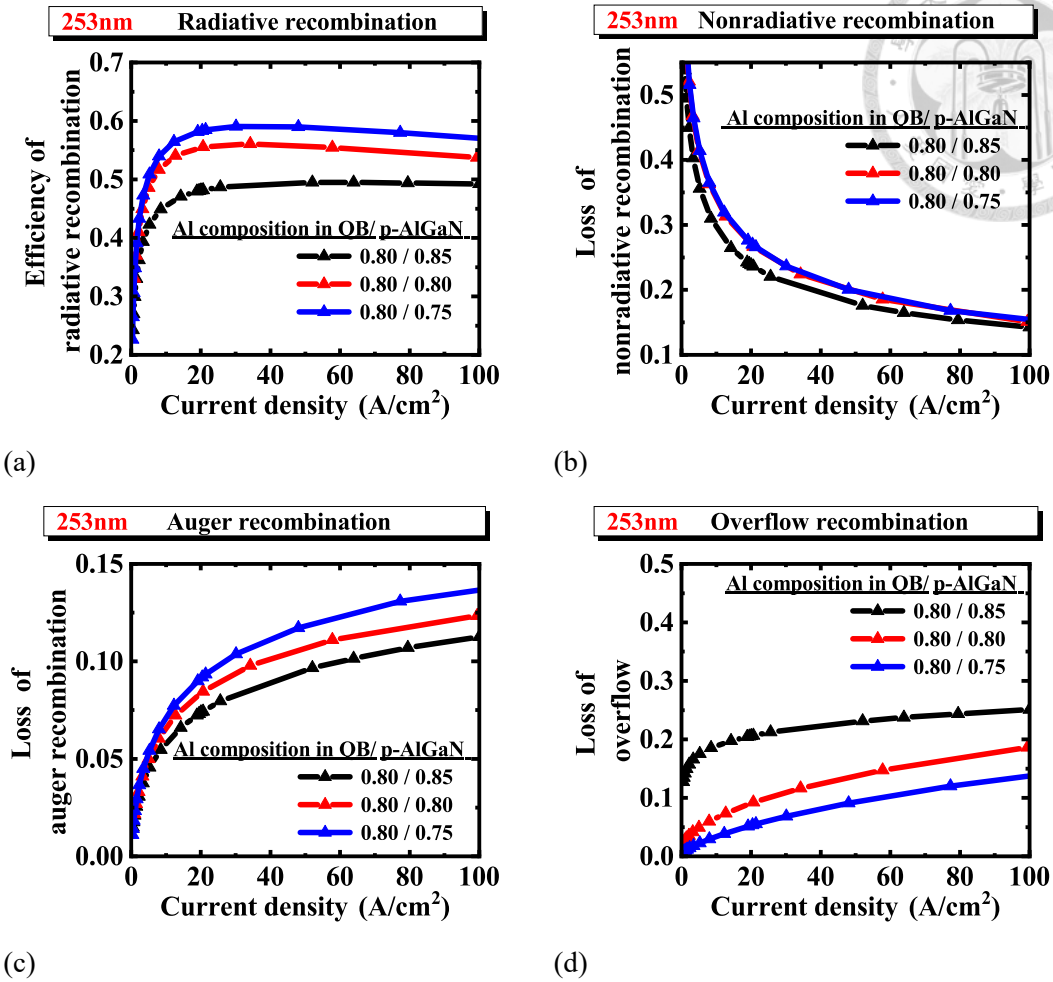

Figure 4.14: The comparison of different p-AlGaN layer cases' efficiency of radiative recombination, nonradiative recombination, auger recombination, and overflow to current density plot in 253 nm considering random alloy fluctuation.

Table 4.3: The loss of the carrier overflow $\simeq$ 20 (A / cm^2) in different p-AlGaN layer cases.

wavelength	225 nm	225 nm	225 nm	253 nm	252 nm	252 nm
Loss \ Δ Al	0.2	0.18	0.15	0.2	0.18	0.15
Electron overflow	0.009	0.029	0.039	0.054	0.092	0.207
Hole overflow	0.002	0.002	0.002	0.001	0.001	0.001

For different p-AlGaN layer cases in this study, the electron carrier overflow can effectively decrease by designing the p-AlGaN layer. Therefore, the radiative recombination and wall-plug efficiency of the p-AlGaN in this study have better performance, as shown

doi:10.6342/NTU202303083

in Table 4.3. In addition, the loss is calculated by Eq. (4.2), and the emission wavelength in different p-AlGaN layer cases will shift slightly by the strain-caused polarization field in QW is different.

4.2.2.4 Wall plug efficiency

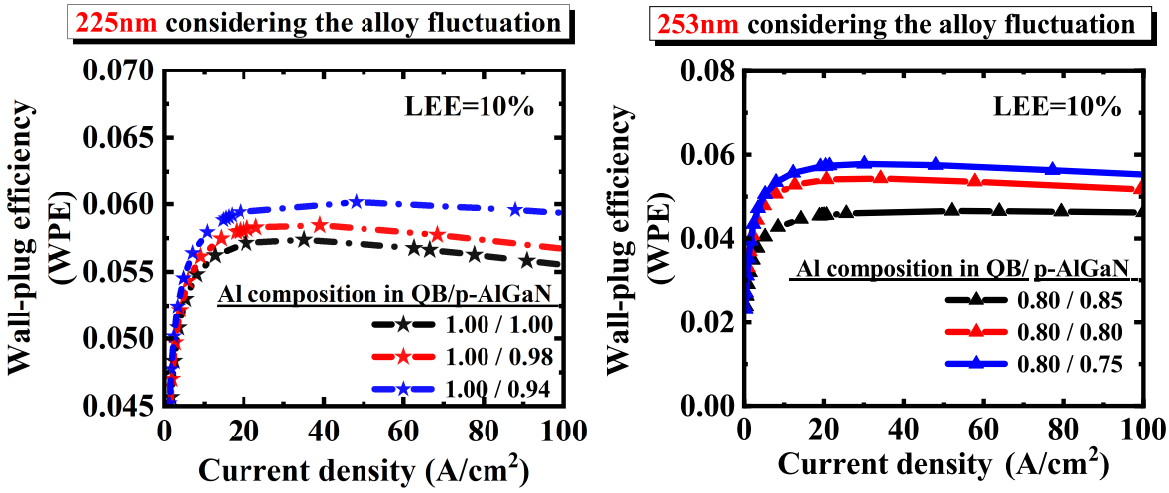

(a) 225 nm (b) 253 nm

Figure 4.15: Considering random alloy fluctuation, the wall-plug efficiency (WPE) to current density plot of different p-AlGaN layers.

According to the wall plug efficiency, under this work's simulation structure and optimization design, the design of the p-AlGaN layer performs better in 225 nm or 253 nm cases. Therefore, the analysis of the simulation result in the following Chapter will use the Al composition design of QW, QB, and p-AlGaN layer in 225 nm with 0.8, 1.0, and 0.94, respectively; The Al composition design of QW, QB, and p-AlGaN layer in 253 nm with 0.6, 0.8, and 0.75, respectively.

doi:10.6342/NTU202303083

4.3 Summary

In optimizing the QBs section, the electron carrier overflow can effectively lower by increasing the potential difference between QWs and QBs. Hence, the difference of the Al composition in 0.2 is the best optimization design of the QB's epitaxial in this study.

In the improvement of the hole carrier injection section, based on two reasons, one is that the optimization of the QB had improved the electron carrier overflow in the previous work, and another is that the shallower QW for holes induced by strain will decrease the electron carrier overflow by the more obvious carrier confinement in QW decrease for holes. Therefore, for the p-AlGaN design with a smaller Al composition than the last QB, the tunneling effect causing hole injection will further reduce the electron carrier overflow, leading to better WPE performance.

doi:10.6342/NTU202303083

Chapter 5 The influence of random alloy fluctuation and strain-induced deformation potential energy shift in 225 nm and 253 nm UVC-LEDs

5.1 Influence of random alloy fluctuation to the polarization ratio

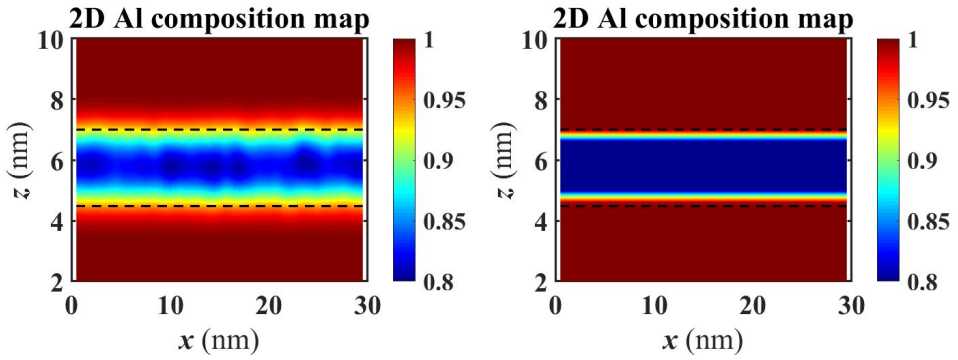

(a) With random alloy fluctuation (b) Without random alloy fluctuation

Figure 5.1: The Al composition distribution of 225 nm in 2 nm QW.

doi:10.6342/NTU202303083

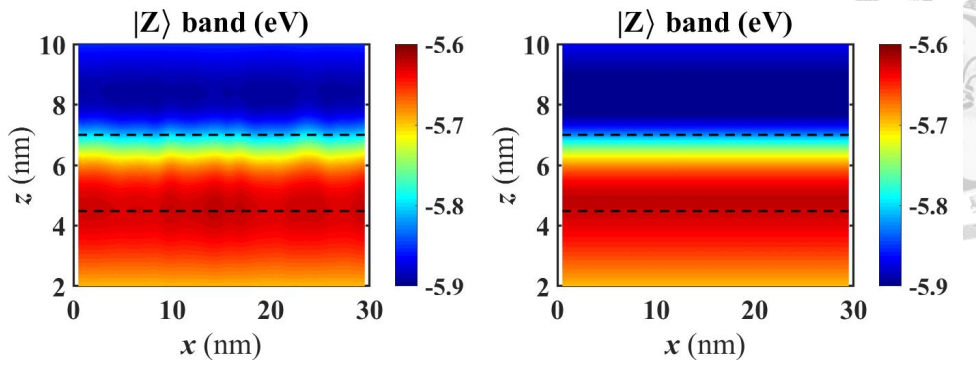

(a) With random alloy fluctuation (b) Without random alloy fluctuation

Figure 5.2: The valance band's effective confinement potential at 225 nm in 2 nm QW.

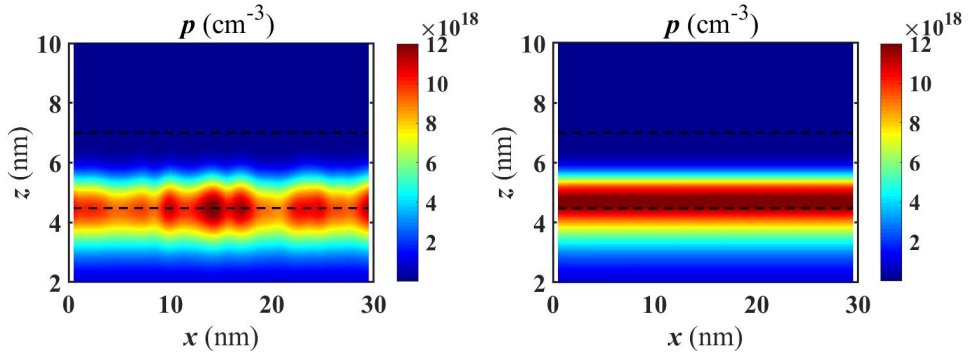

(a) With random alloy fluctuation (b) Without random alloy fluctuation

Figure 5.3: The hole density of 225 nm in 2 nm QW.

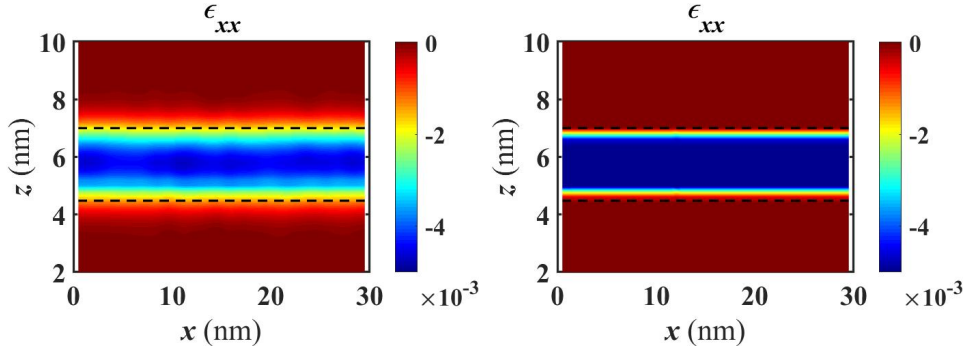

(a) With random alloy fluctuation (b) Without random alloy fluctuation

Figure 5.4: The conduction band distribution of 225 nm in 2 nm QW.

Fig. 5.1 to Fig. 5.4 are shown that the random alloy fluctuations will let the Al composition in the QW edge increase, and the band bending caused by the crystal orientation in wurtzite GaN crystal will let the carrier localized in the QW edge.[15–17]

doi:10.6342/NTU202303083

Note that two mechanisms will influence the polarization ratio under the above situation. One is that the carrier confined in a higher Al composition site will increase the spontaneous radiative recombination by the transition between $|Z\rangle$ state dominant band and the conduction band. The other is the lattice mismatch lead lateral compressive strain in QW will release by the higher Al composition at the QW edge. For AlGaN material with high Al, the domination of the $|Z\rangle$ state dominant band will increase when the lateral compressive strain is released.[23] To put it differently, when the lateral compressive strain is released in high Al's AlGaN material, the spontaneous radiative recombination by the transition between the $|Z\rangle$ state dominant band and the conduction band will increase.

Additionally, the holes in the $|Z\rangle$ state dominant valance band recombination and generation with the electron in the conduction band, the light emission will be TM-polarized and increase the polarization ratio.[15, 22] Therefore, there has an interesting topic of whether the light extraction issue can be improved by the TM polarized light decrease when the compressive strain applies to the QW region.[23] Therefore, when considering the random alloy fluctuation, whether the Al composition increase at the QW edge or the lateral compressive strain release in the QW region will increase the TM polarized light and the polarization ratio. [3]

In conclusion, it is crucial to include random alloy fluctuation in precise simulation because the without random alloy fluctuation calculation will underestimate the TM polarized light.

doi:10.6342/NTU202303083

5.2 The impact factor of carrier blocking ability

This work will discuss the two impact factors that influence the carrier blocking ability. The two impact factors are random alloy fluctuation and strain.

5.2.1 Random alloy fluctuation

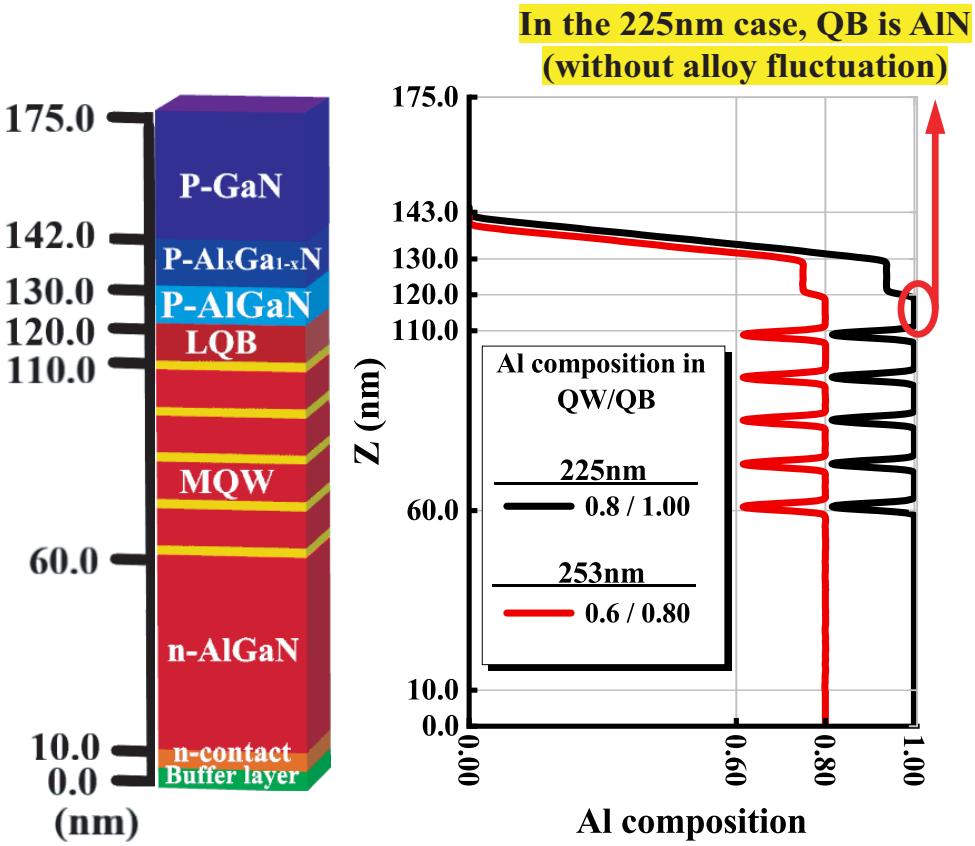

Figure 5.5: The Al composition distribution of 225 nm and 253 nm with random alloy fluctuation in the best optimization design of QB and p-AlGaN layer.

Here is the analysis of what random alloy fluctuation, which is the impact factor of carrier blocking ability, will influence the performance of UVC-LEDs. Fig. 5.5 shows the Al composition distribution in the following discussion and analysis. The epitaxial structure of it had optimized in Chapter 4 with the Al composition difference between

doi:10.6342/NTU202303083

QW and QB is 0.2; The Al composition of the p-AlGaN layer is 0.94 and 0.80 in 225 nm and 253 nm, respectively.

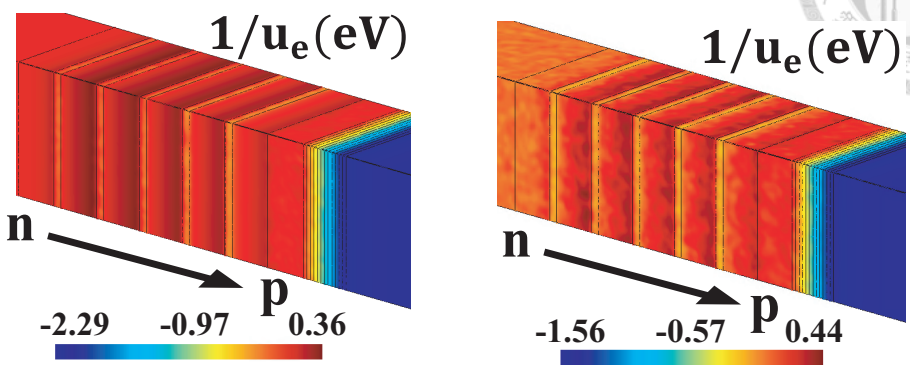

(a) 225 nm with random alloy fluctuation (b) 253 nm with random alloy fluctuation

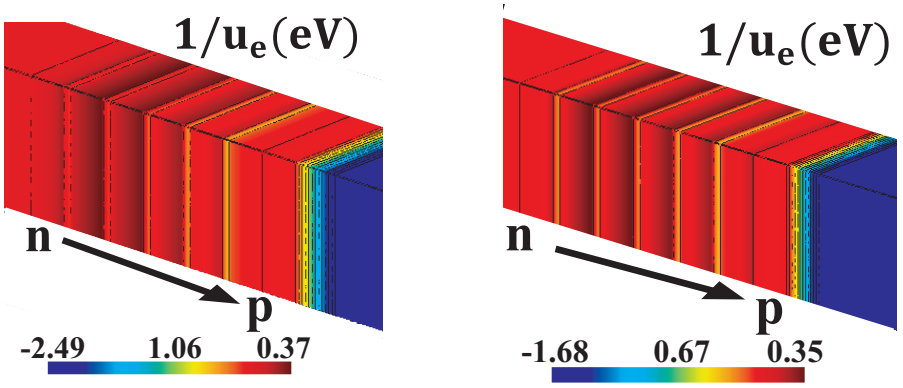

(c) 225 nm without random alloy fluctuation (d) 253 nm without random alloy fluctuation

Figure 5.6: Conduction band distribution at current density $\simeq$ 20 (A/cm^2).

The following talk about the random alloy fluctuation in AlGaN material will influence the carrier transport by the potential fluctuation.

Fig. 5.6 are the effective confinement potential of the conduction band ($W_e \equiv 1/u_e$), which is calculated by the LL model in 225 nm and 253 nm with and without random alloy fluctuation cases. The QB of 225 nm did not have a potential fluctuation due to the AlN QB used in the 225 nm case. The AlN material is not an alloy and has no Al composition fluctuation. In addition, the QW in 225 nm is still the alloy material. That is, random alloy fluctuation will influence the potential in the QW region of 225 nm and the potential

doi:10.6342/NTU202303083

bending in QB.

After considering the fully random alloy fluctuation in the structure caused by the epitaxial growth process, the bend bending from p-type to n-type will decrease at the current density $\simeq 20$ (A/cm^2). Due to the random alloy fluctuation will cause the potential fluctuated, the effective potential barrier for carriers will reduce, and lead to better carrier transport.[29, 30, 61] On the other hand, under a similar band structure banding degree, the random alloy fluctuation will increase the current density in the structure. Namely, without considering the random alloy fluctuation, the turn-on voltage at current density in 20 (A/cm^2) will be overestimated and cause the band bending from the p-AlGaN to n-AlGaN in the system to become more tilted.

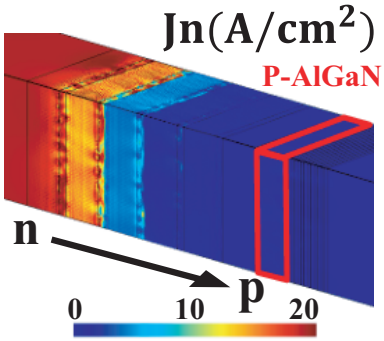

(a) 225 nm with random alloy fluctuation

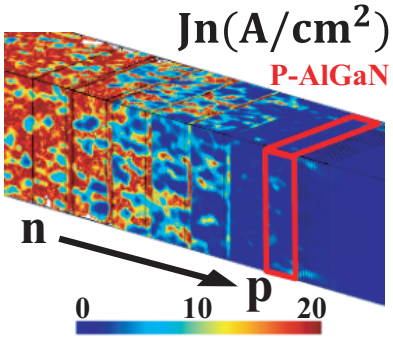

(b) 253 nm with random alloy fluctuation

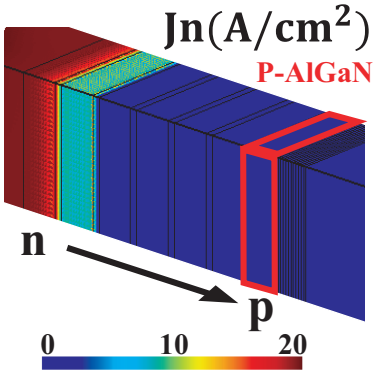

(c) 225 nm without random alloy fluctuation

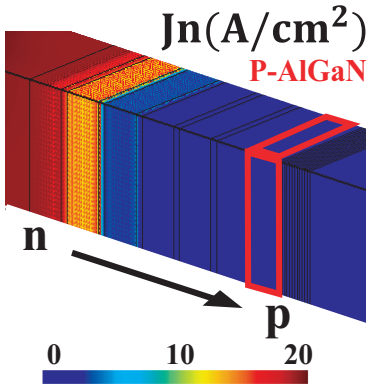

(d) 253 nm without random alloy fluctuation

Figure 5.7: Electron current density at current density $\simeq 20$ (A/cm^2).

doi:10.6342/NTU202303083

Fig. 5.7 are the electron current density at the current density$\simeq$ 20 (A/cm^2) in 225 nm and 253 nm with and without considering the random alloy fluctuation cases.

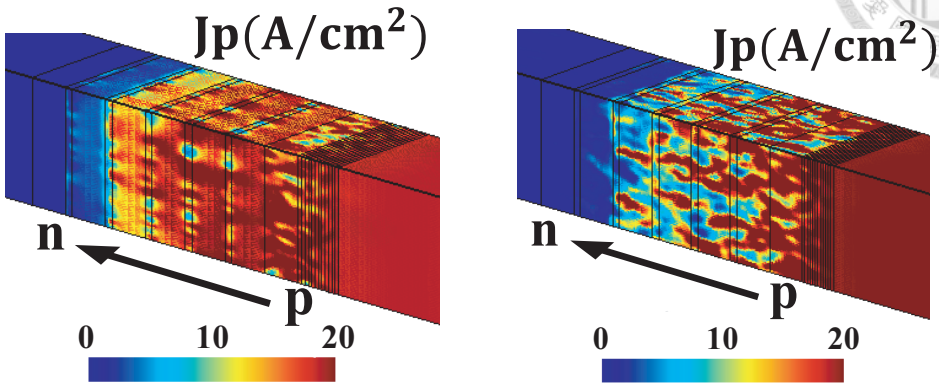

(a) 225 nm with random alloy fluctuation (b) 253 nm with random alloy fluctuation

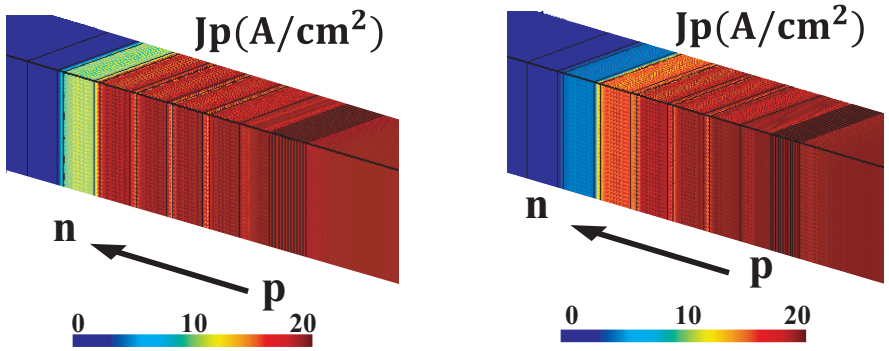

(c) 225 nm without random alloy fluctuation (d) 253 nm without random alloy fluctuation

Figure 5.8: Hole current density at current density $\simeq$ 20 (A/cm^2).

Fig. 5.8 are the hole current density at the current density$\simeq$ 20 (A/cm^2) in 225 nm and 253 nm with and without considering the random alloy fluctuation cases.

After comparing the 225 nm and 253 nm considering the random alloy fluctuation cases, 225 nm has better carrier confinement in QW than the 253 nm case. Owing to the potential of the AlN quantum barrier is uniform and has no fluctuation in 225 nm. On the other hand, for the 253 nm case, due to the potential fluctuation in $Al_xGa_{1-x}N$ quantum barriers, the electron carrier overflow to the p-AlGaN layer is more obvious than 225 nm. In addition, the electron carriers could be better confined in the 225 nm or 253 nm

doi:10.6342/NTU202303083

without random alloy fluctuation cases, especially in 225 nm the electron carrier overflow will further inhibit by the AlN QB. Therefore, the random alloy fluctuation forming in the epitaxial growth process greatly influenced the electron carrier transport and blocking ability.[29, 30, 61]

Furthermore, the band gap to composition relation is nonlinear but increases the slope with Al composition in AlGaN materials.[66] Hence, in this study, the design of 225 nm and 253 nm under the same Al composition difference between the QW and QB, the depth of the QW in 225 nm and 253 nm are not the same. In 253 nm, the shallower depth of the QW will also influence the electron carrier ability.

In this work, the better hole injection leads the hole carrier transport to p-side QW. However, due to the higher potential for holes under the n-type dopant in the first QB, the hole carrier will not overflow to the n-AlGaN layer, as shown in Fig. 4.9 and Fig. 5.8. In addition, in the 225 nm case, as the QW 2 has the highest valance band potential in the QWs region, the hole density distribution is dominated by the QW 2.

After considering the random alloy fluctuation in the 225 nm, the apparent improvement of the electron carrier transport and the severe electron carrier overflow do not happen. The main reason is that the AlN QB in 225 nm is not an alloy and has no random alloy fluctuation. Emphasize that the fluctuation potential in QB might be the critical factor leading to electron carrier overflow.

Additionally, the electron carrier injection is relatively large (low) in 253 nm (225 nm) without considering the random alloy fluctuation case due to the work function of AlGaN (AlN) QB having the larger (smaller) value.

In summary, the electron carrier dominates the carrier overflow because the less hole

doi:10.6342/NTU202303083

carrier overflow can be neglected in the optimized structure.

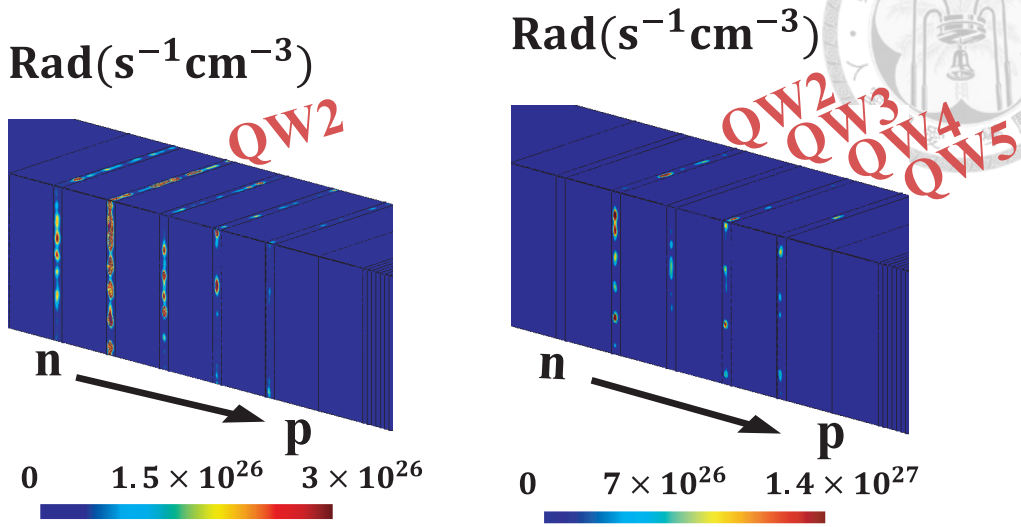

(a) 225 nm with random alloy fluctuation (b) 253 nm with random alloy fluctuation

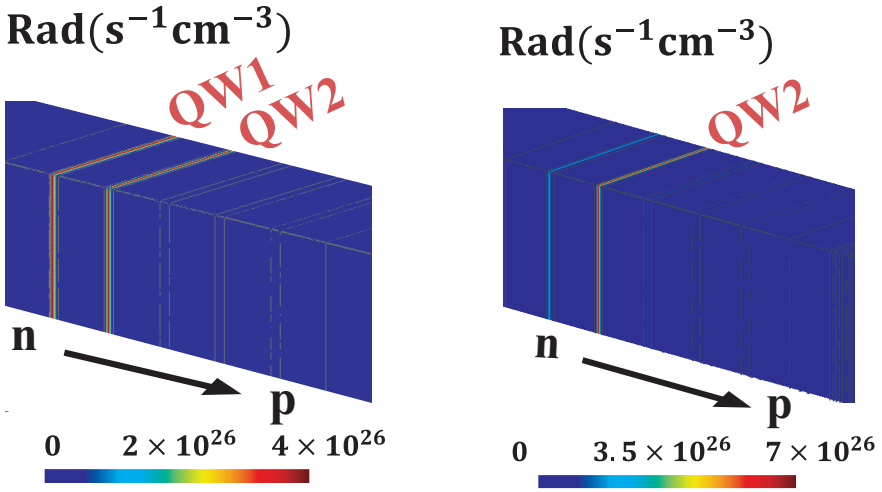

(c) 225 nm without random alloy fluctuation (d) 253 nm without random alloy fluctuation

Figure 5.9: Radiative recombination distribution at current density $\simeq$ 20 (A/cm^2).

Below will analyze the radiative recombination distribution changing by random alloy fluctuation lead carrier blocking ability reduction. As shown in Fig. 5.9, the radiative recombination in the p-side QW will increase when considering the random alloy fluctuation because the potential fluctuation in the barrier will let the carriers may cross the barrier more easily.[29, 30, 61] The improvement of the electron carrier transport will increase the radiative recombination in the p-side QW.

doi:10.6342/NTU202303083

At a small current density, the reason why the n-side QW dominates the radiative recombination distribution and the radiative recombination in the p-side QW did not obvious will analysis in Chapter 5.2.2.3: strain caused shallower quantum well.

5.2.1.1 Internal quantum efficiency

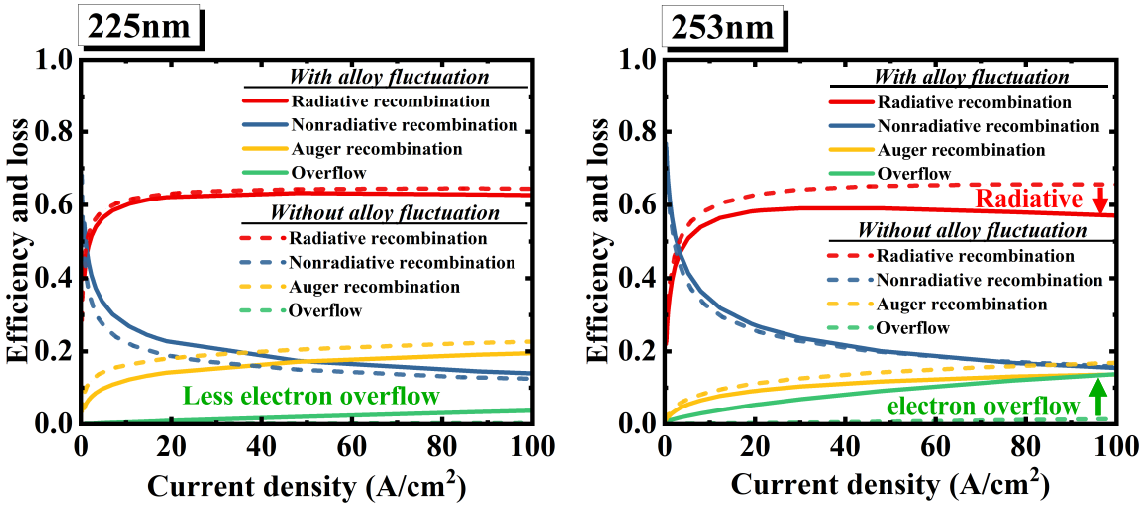

(a) 225 nm (b) 253 nm

Figure 5.10: The efficiency to the current density plot. The solid and dash lines are with and without random alloy fluctuation cases. Different colors in the red, blue, yellow, and green lines represent the efficiency of radiative recombination, non-radiative recombination, auger recombination, and carrier overflow efficiency, respectively.

The following will analyze how the random alloy fluctuation lead carrier blocking ability reduction will influence the efficiency, as shown in Fig. 5.10

After considering the fully random alloy fluctuation, carriers can cross the potential barrier more easily due to the potential fluctuation causing percolation path, which will decrease the carrier confinement of QWs.[29, 30, 61] Therefore, after considering the random alloy fluctuation, the radiative recombination efficiency will decrease, and the carrier overflow efficiency will become severe. In addition, the electron carrier dominates the carrier overflow because the less hole carrier overflow can be neglected in the

doi:10.6342/NTU202303083

optimized structure, as shown in Fig. 5.7 and Fig. 5.8.

The loss of electron carrier overflow in 225 nm and 253 nm shows that after considering the random alloy fluctuation, compared to the 225 nm, the more noticeable increase of electron carrier overflow for 253 nm, due to the AlN QB in 225 nm having a better carrier-blocking ability. Emphasize that fluctuated potential in QBs could be the critical factor leading to electron carrier overflow. Therefore, Chapter 4.1 optimizes the potential barrier by adjusting the Al composition of QB.

5.2.2 Strain

5.2.2.1 The analysis of band structure deformation induced by strain

The mechanism of the band structure deformation induced by strain can roughly divide into valence-band deformation potential ($D_1 \sim D_6$) and hydrostatic deformation potential (a).

Following is the discussion of valence-band deformation potential ($D_1 \sim D_6$).

When applying the strain, the response of different states' interaction and coupling is valence-band deformation potential ($D_1 \sim D_6$). When applying the compressive strain, the valence-band deformation potential will let the valence band move down. As mentioned in Chapter 3.1, under the simulation structure design of this study, the QBs have no strain, and the strain in QWs is compressive. That means the valence-band deformation potential ($D_1 \sim D_6$) applied in the QBs region is zero, but it does in the QWs region. In brief, when considering the compressive strain in a QW, the valence-band deformation potential ($D_1 \sim D_6$) will shallower the QWs for holes and larger an effective conduction

doi:10.6342/NTU202303083

band offset ratio.

Following is the discussion of hydrostatic deformation potential (a).

For anisotropic polarization in GaN-based wurtzite structure caused by the crystal orientation[15–17], the hydrostatic deformation potential will change the band gap when the strain is applied. Due to the hydrostatic energy shift will occur in the presence of strain inhomogeneity.[31] Based on the QB having no strain, the hydrostatic energy shift applied in the QBs region is zero. When the compressive strain in the QW is applied, the hydrostatic deformation potential (a) will cause the shallow QW for holes and electrons by hydrostatic energy shift. In conclusion, when applying the compressive strain, the QWs will be shallower for electrons and holes due to the hydrostatic deformation potential (a).

Additionally, in this study, the ratio of hydrostatic energy shift applied to the conduction and valance band is 0.63, which is the setting of the conduction band offset ratio in this study.[47, 49] Namely, in this study, the hydrostatic deformation potential (a) will not change the conduction band offset ratio when the strain is applied.

doi:10.6342/NTU202303083

Table 5.1: The dedication of strain-related terms on the band structure in 225 nm and 253 nm without random alloy fluctuation cases.

	225 nm		253 nm	
hydrostatic deformation potential (a)	QW	QB	QW	QB
$\Delta E_{c,\text{hydrostatic}}$ (eV)	0.020	0	0.020	0
$\Delta E_{v,\text{hydrostatic}}$ (eV)	-0.012	0	-0.012	0

	225 nm		253 nm	
valence-band deformation potential ($D_1 \sim D_6$)	QW	QB	QW	QB
$\Delta E_{c,\text{deform}}$ (eV)	0	0	0	0
$\Delta E_{v,\text{deform},CH1}$ (eV)	-0.062	0	-0.062	0
$\Delta E_{v,\text{deform},CH2}$ (eV)	-0.062	0	-0.062	0
$\Delta E_{v,\text{deform},CH3}$ (eV)	**-0.125**	0	**-0.124**	0

In the QW region, the decrease of the total strain-induced deformation potential in the valance band is much more significant than the increase of the total strain-induced deformation potential in the conduction band; see Table 5.1 The calculation of Table 5.1 is according to Eq. (2.57) to Eq. (2.61). Therefore, the valance band deformation might dominate the influence of strain-caused deformation potential in the system. In addition, the dedication of the valance band deformation is mainly led by the valence-band deformation potential ($D_1 \sim D_6$). Therefore, the following analysis of carrier clocking ability influenced by strain will focus on the deformation potential in the valance band and the shallower QW for holes. In addition, this study also considers the crystal field split-off energy (Δ_1 and Δ_2), as shown in Eq. (2.49) to Eq. (2.52)

doi:10.6342/NTU202303083

5.2.2.2 The comparison of strain-related parameters

Before discussing the influence of the carrier-blocking ability by strain, it is essential to confirm that the strain-related parameter used in this work is appropriate. To prove that, below will compare the simulation result of radiative distribution in different papers' parameters.

Table 5.2: The strain-related parameters in different research

	a_c (eV)	D_1 (eV)	D_2 (eV)	D_3 (eV)	D_4 (eV)	D_5 (eV)	D_6 (eV)
Source \ material	GaN						
This work	-4.5	-1.7	6.3	8	-4	-4	-5.5
Reference 1[a]	−4.6	-1.7	6.3	8	-4	-4	-5.5
Reference 2[b]	−4.6	-1.7	6.3	8	-4	-4	-5.5
Reference 3[c]	−4.6	-1.7	6.3	8	-4	-4	-5.5
Reference 4[d]	−3.45	-1.7	3.6	8.82	−4.41	−4	−5.1
Reference 5[e]	−4.08	0.7	2.1	1.4	0.7	-4	-5.5
Reference 6[f]	4.9	−3.7	4.5	8.2	4.1	-4	-5.5
Reference 7[g]	-4.5	3	3.6	6.6	3.3	-4	-5.5
Source \ material	AlN						
This work	-4.5	-17.1	7.9	8.8	-3.9	-3.4	-3.4
Reference 1[a]	-4.5	-17.1	7.9	8.8	-3.9	-3.4	-3.4
Reference 2[b]	-4.5	-17.1	7.9	8.8	-3.9	-3.4	-3.4
Reference 3[c]	-4.5	2.89	4.89	7.78	−3.89	−3.44	−3.95
Reference 4[d]	-4.5	3	3.6	9.6	−4.8	−4	−5.1
Reference 5[e]	-4.5	-17.1	7.9	8.8	-3.9	-3.4	-3.4
Reference 6[f]	−3.4	-17.1	7.9	8.8	-3.9	-3.4	-3.4
Reference 7[g]	-4.5	-17.1	7.9	8.8	-3.9	-3.4	-3.4
	[a]Ref[35]	[b]Ref [38]	[c]Ref [22]	[d]Ref [17]	[e]Ref [39]	[f]Ref [37]	[g]Ref [36]

In Table 5.2, the parameter a_c is the related parameter of the hydrostatic deformation potential, and $D_1 \sim D_6$ are the valence-band deformation potential. The font with the red

doi:10.6342/NTU202303083

color represents the parameter that is different from this work.

As Table 5.2 shows that the value of the related parameter of hydrostatic deformation potential (a_c) is fluctuated due to the hydrostatic potential being an-isotropic by the symmetry reduction in wurtzite crystal.[37] Furthermore, in experimental measurement, the output of the band gap is just the total band gap shifting (ΔE_g), which will not tell the dedication of it from the changing of the conduction band (ΔE_c) and valance band (ΔE_v). Therefore, the related parameter of hydrostatic deformation potential in different papers has fluctuated.

As the parameters of research 3 to 7 have more differ from those used in this work. The following will compare their results.

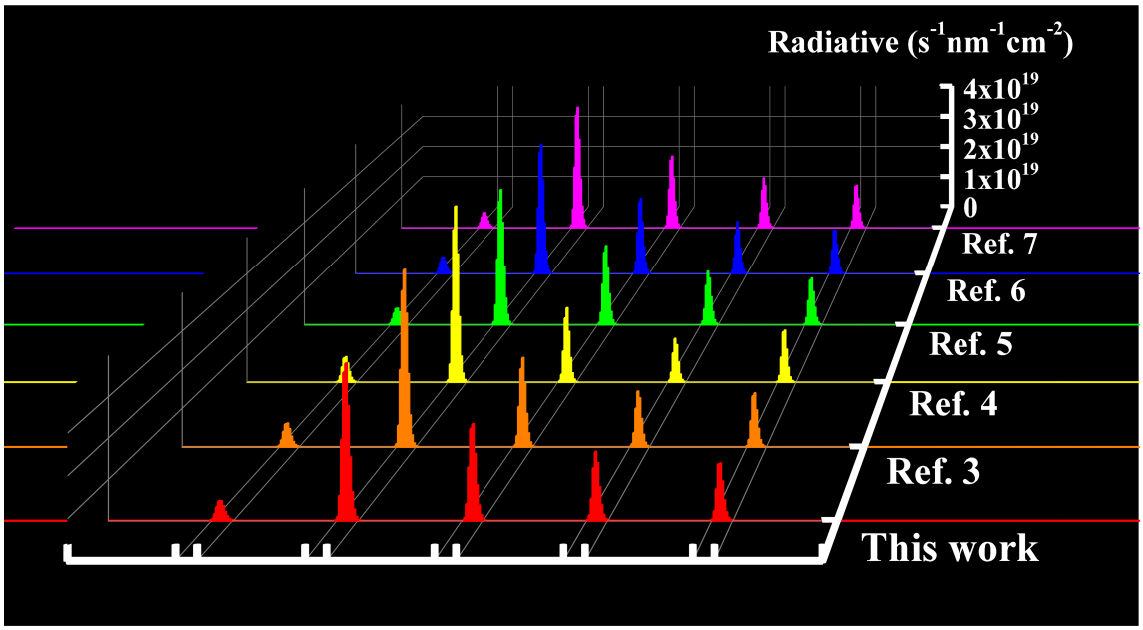

Figure 5.11: The simulation result of 253 nm radiative distribution in the MQW region under different research's strain-related parameters.

Under the simulation solver of 3D Poisson drift-diffusion continuity equation with the strain-induced deformation potential LL model in 253 nm with the random alloy fluctuation cases, the radiative result has a similar distribution in MQW regions, whether the

doi:10.6342/NTU202303083

strain-related parameter of this work or other research, as shown in Fig. 5.11. Therefore, the similarity tendency in radiative distribution confirms that the strain-related parameter in this work is reliable. After that, the discussion of the band structure deformation by the strain-related term will continue.

5.2.2.3 Strain caused shallower QW for holes

The previous section has a detailed analysis of what is the CB, CH1, CH1, and CH3 bands' deformation and the cause of formation, see Table 5.1. Differently, this section will focuses on the strain-induced deformation potential on the valance band and does not analyze what strain-related terms caused its deformation.

As we mentioned in Chapter 3.1, for the structural design of this study, the bottom layer, which is the AlGaN transition buffer layer, assigns the same Al composition as the QB layer. Hence, in the QBs region, there has no strain, but with the compressive strain in the QWs region.

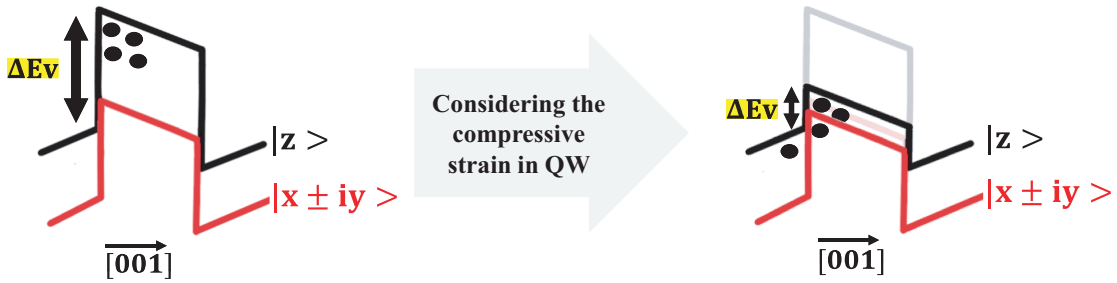

Figure 5.12: The mechanism of strain-induced deformation potential in high Al composition AlGaN QW region.

In AlGaN materials with high Al, the valance band of $|X \pm iY\rangle$ and $|Z\rangle$ state dominant band will decrease the energy in the electron voltage after considering the compressive strain of the structure. Therefore, the valance band lowering induced by compressive

doi:10.6342/NTU202303083

strain in the QWs region will reduce the difference of the dominant valance band (ΔE_v). Furthermore, for AlGaN materials with high Al, the splitting of the $|X \pm iY\rangle$ and $|Z\rangle$ state dominant valance band will decrease simultaneously.[23]

1D Band structure in QW 2 Whether in 225 nm or 253 nm, the dominant valance band is the $|Z\rangle$ state dominant band due to the field split-off energy in AlN material (Δ_1=-0.169).[18] Therefore, this study uses the $|Z\rangle$ state dominant band to analyze the influence of the band structure deformation induced by strain in Fig. 5.13. The figure shows that the QW for holes will be shallower due to the reduced of the ΔE_v induced by the compressive strain, as shown in Fig. 5.13(a). Furthermore, as mentioned above, compared to AlN QB in 225 nm, the QB in 253 nm is the alloy material, and the alloy will fluctuate on potential. Therefore, the potential has fluctuated on the 253 nm QB in Fig. 5.13(b). As shown in the Fig. 5.13, after considering the strain in the QW region, the operation voltage for the same current density will decrease at 223 nm and 253 nm due to the shallower QW for the carrier.

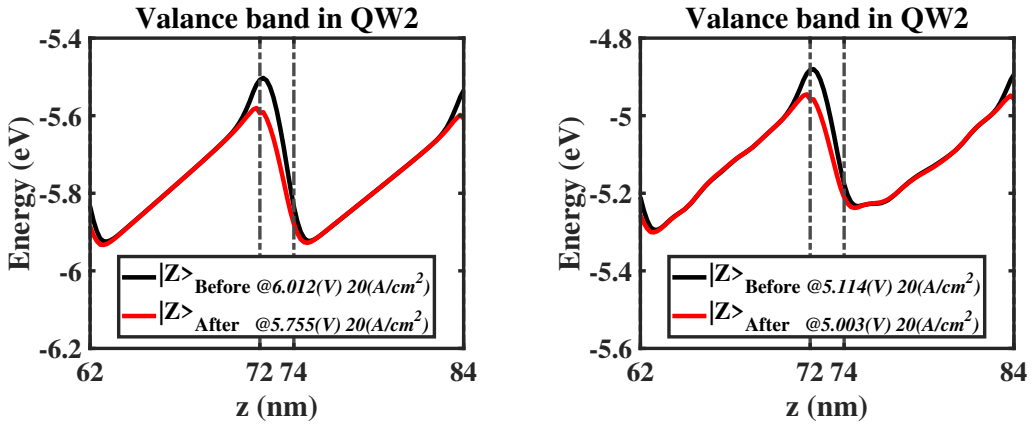

(a) 225 nm (b) 253 nm

Figure 5.13: (a) and (b) are the $|Z\rangle$ state dominant band distribution of 225 nm and 253 nm with random alloy fluctuation cases in the second QW region under the 2 nm QW sandwich by QWs. The black and red lines are the cases of before and after considering the strain in QW under current density $\simeq$ 20 (A/cm^2). For additional information, the first QW is closer to n-AlGaN.

doi:10.6342/NTU202303083

2D hole carrier density in QW 2 Due to the shallower QW for holes, the holes will more easily cross the barrier of the QWs.[64] The confinement of the QW region for holes will reduce at the same time. Therefore, the hole carrier distribution in the QB region will increase after considering the compressive strain in the QW region. Then, we set the hole density ratio formula in the QB region to evaluate the hole carrier density in the QB region in Eq. (5.1).

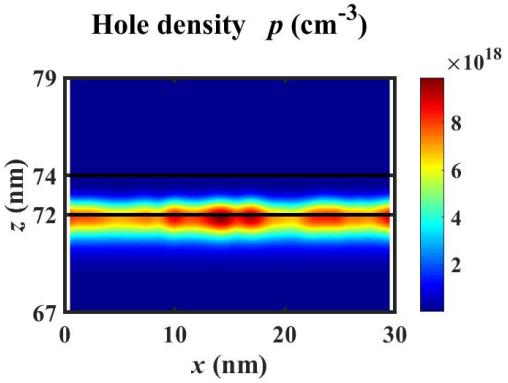

(a) 225 nm before considering the compressive strain in QW.

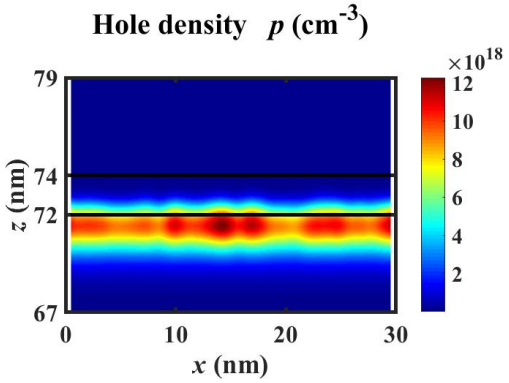

(b) 225 nm after considering the compressive strain in QW.

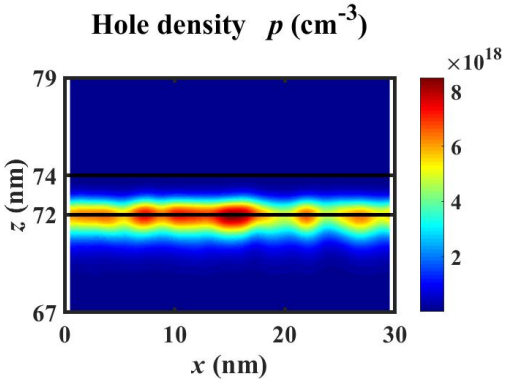

(c) 253 nm before considering the compressive strain in QW.

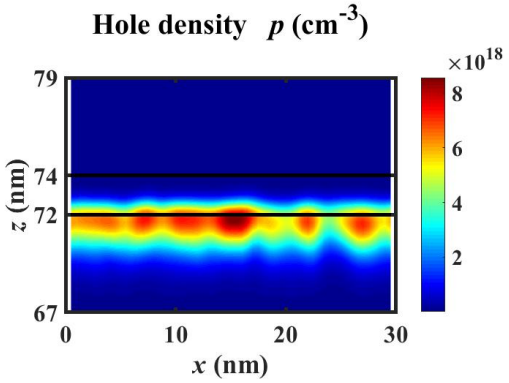

(d) 253 nm after considering the compressive strain in QW.

Figure 5.14: (a), (b), (c) and (d) are the 2D hole density of 225 nm and 253 nm considering the random alloy fluctuation cases at the current density $\simeq$ 20 (A/cm^2) in the second QW region under the 2 nm QW sandwich by QWs. For additional information, the first QW is closer to n-AlGaN.

$$\text{hole density ratio in QB} = \frac{p_{QB}}{p_{QB} + p_{QW}} \times 100\%, \tag{5.1}$$

doi:10.6342/NTU202303083

where p_{QB} is the hole carrier density of the QB closer to the n-contact, and p_{QW} is the hole carrier density of the QW.

Have detailed information on the hole density ratio formula in the QB region in the following.

Because the crystal orientation lead to GaN in the wurtzite structure having in-homogeneous polarization[15–17], the intrinsic spontaneous polarization and the external force-induced piezoelectric polarization will tilt the band structure. In the QW region, the compressive strain caused by piezoelectric polarization is more considerable than the intrinsic spontaneous polarization in the material, and the signs of them are different. If the material is grown in the direction of the c-axis [001], a relative maximum of the tilted band structure in the QW is closer to the n-contact. In the structure of the QW sandwiched by the QBs, based on the hole carrier will accumulate at the related maximum of the valance band structure, and with shallower QW for holes induced by the compressive strain, the hole carriers will increase in the QB, which is the one that is closer to the n-contact.[4] To sum up, in Eq. (5.1), the QB of p_{QB} is the one that is closer to the n-contact under the sandwich structure of QW and QBs.

The result is that, in this study, after considering the compressive strain in the QW, the hole density ratio in the QB region will change from 66% to 81% in 225 nm; the hole density ratio in the QB region will vary from 62% to 77% in 253 nm, as shown in the hole density plot in Fig. 5.14.

doi:10.6342/NTU202303083

5.2.3 The influence of carrier blocking ability on UVC-LED's performance

5.2.3.1 Carrier density

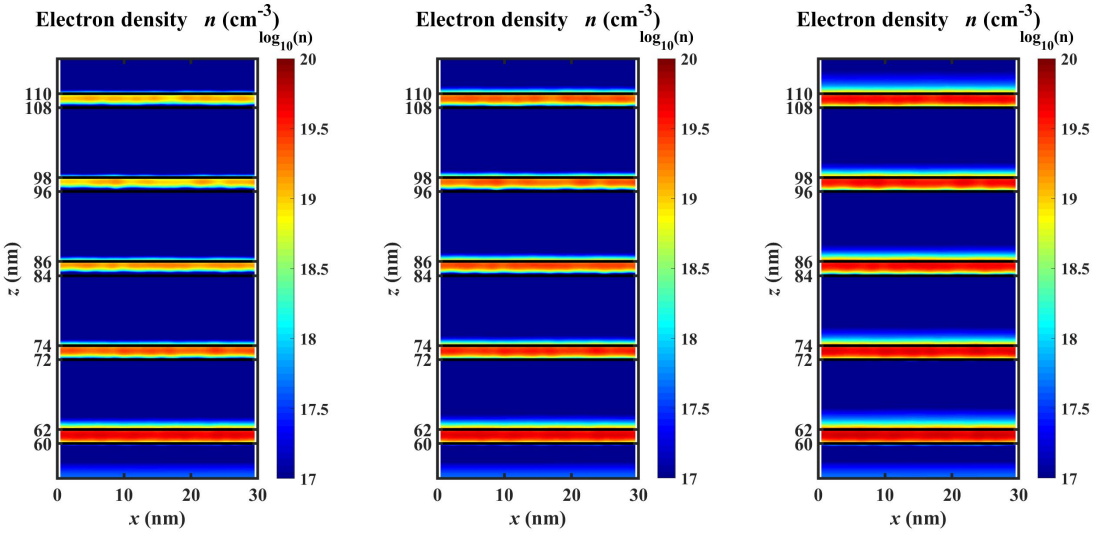

(a) J ≃ 20 (A/cm^2) (b) J ≃ 100 (A/cm^2) (c) J ≃ 900 (A/cm^2)

(d) J ≃ 20 (A/cm^2) (e) J ≃ 100 (A/cm^2) (f) J ≃ 900 (A/cm^2)

Figure 5.15: (a), (b), and (c) are electron density (cm^{-3}) of 225 nm with random alloy fluctuation cases in the MQW region from current densities ≃ 20 to 900 (A/cm^2). (d), (e), and (f) are hole density (cm^{-3}) of 225 nm with random alloy fluctuation cases in the MQW region from current densities ≃ 20 to 900 (A/cm^2).

doi:10.6342/NTU202303083

5.2.3.2 Current density

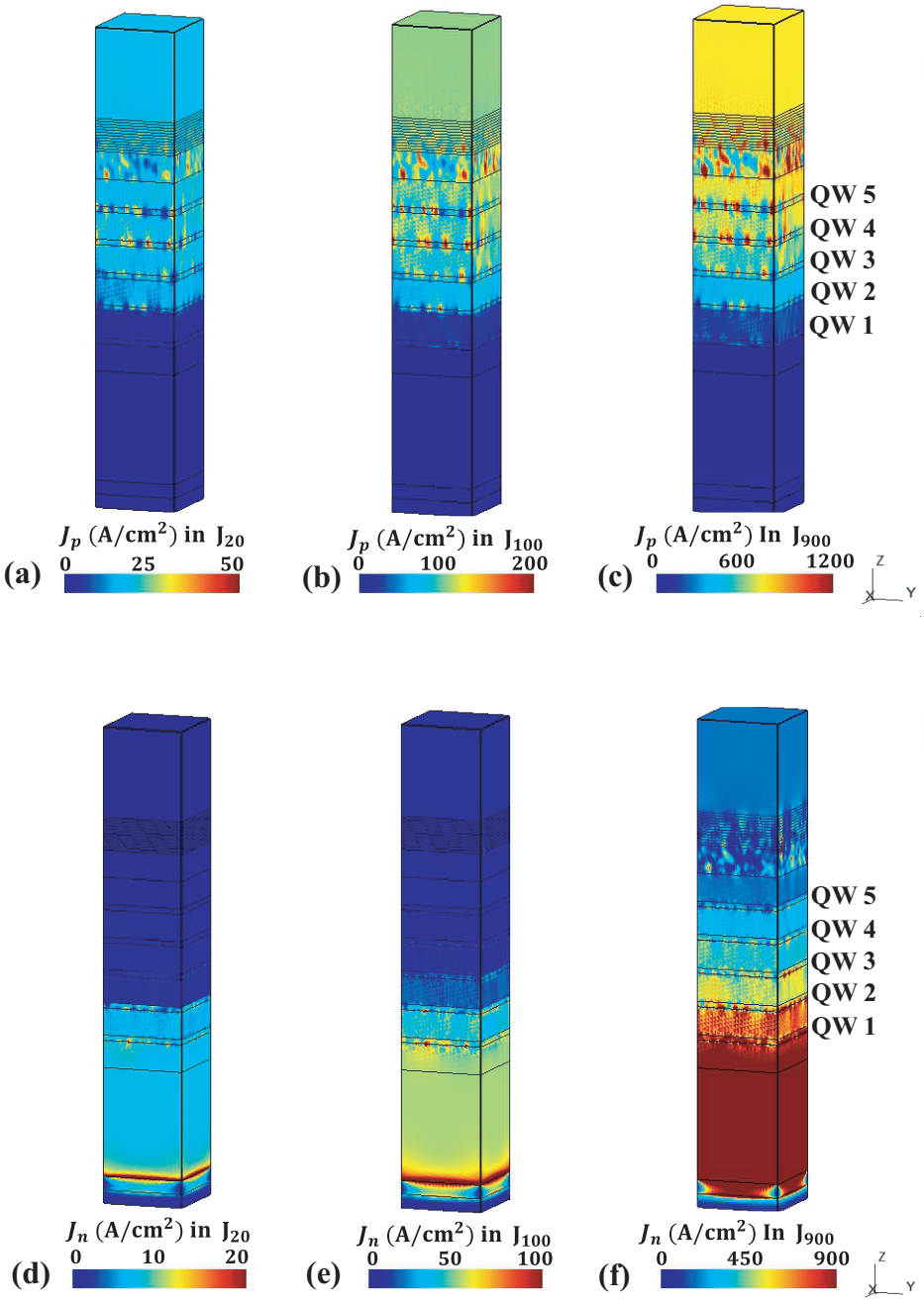

Figure 5.16: (a), (b), and (c) are the hole current density distribution of 225 nm with random alloy fluctuation under different current densities cases. (d), (e), and (f) are the electron current density distribution of 225 nm nm with random alloy fluctuation under different current densities cases.

doi:10.6342/NTU202303083

The discussion will be how carrier transport improves by the shallower QW afterward. In other words, the shallower QW will decrease the carrier-blocking ability of the QB region (active region). [49]

As mentioned above, the quantum well for electrons or holes will be shallower under the strain-induced band structure deformation. However, the valance band lowering is larger than the increase of the conduction band under the strain-induced deformation.

The effective conduction band offset ratio is 0.63 without the strain-induced deformation potential case.[47, 49] Namely, the difference of the dominant valance band (dE_v) is smaller than the difference of the conduction band (dE_c) before the band structure deformation. Also, the valence-band deformation potential ($D_1 \sim D_6$) did not apply to the conduction band. Therefore, after considering the strain-induced deformation potential, the influence of shallower QW for holes is more significant than that of electrons as shown in Fig. 5.15 In brief, the more obvious hole carriers distribution in QB region than electron carriers due to the more significant influence of shallower QW for holes than electrons.

Furthermore, the shallower QW for holes improves the hole carrier transport and leads the hole carrier density mainly distributed in n-side QW. The direction of the tilted band by in-homogeneous polarization determines the hole density will increase in the QB closer to n-type when the strain-induced shallower QW for holes. In addition, in the 225 nm case at current densities $\simeq$ 20 (A/cm^2), as the QW 2 has the highest valance band potential in the QWs region, the hole density distribution is dominated by the QW 2, as shown in Fig. 4.9 and Fig. 5.15.

In conclusion, at the small current density case in 223 nm, due to the shallower QW for holes induced by strain and the QW 2 having the highest valance band potential in the

doi:10.6342/NTU202303083

QWs region, hole carriers will mainly dominate by the QW 2. Additionally, as mentioned above, due to the higher potential for holes under the n-type dopant in the first QB, the hole carrier will not overflow to the n-AlGaN layer, as shown in Fig. 4.9 and Fig. 5.16. At the small current density case in 223 nm, for the electrons, due to the shallower QW for electrons induced by strain and the potential barrier of the last QB is not high enough to inhibit the carrier overflow, the electron carrier will overflow, as shown in Fig. 4.9 and Fig. 5.16.

5.2.3.3 Radiative recombination

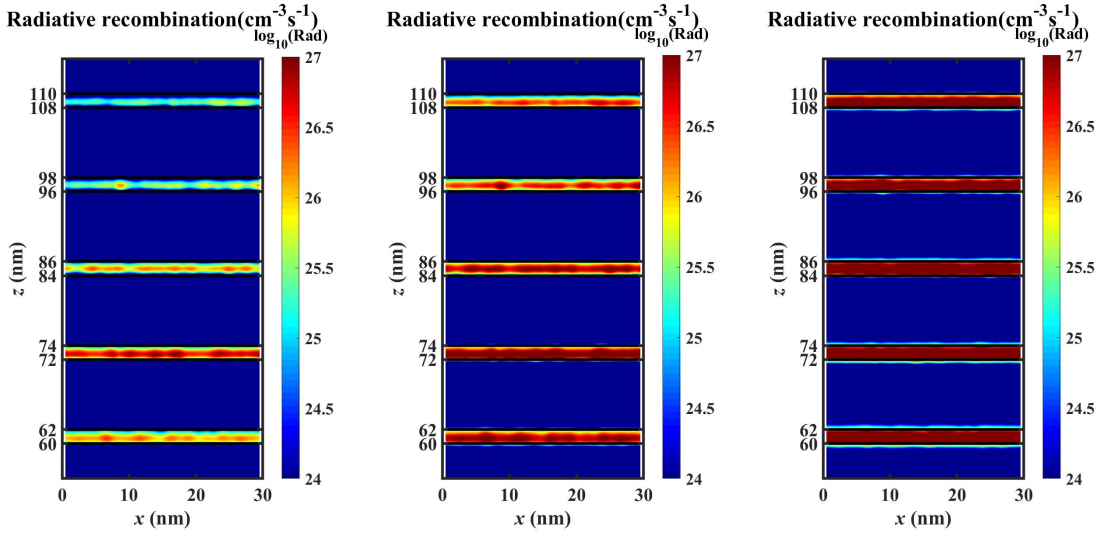

(a) J ≃ 20 (A/cm^2) (b) J ≃ 100 (A/cm^2) (c) J ≃ 900 (A/cm^2)

Figure 5.17: (a), (b), and (c) are radiative recombination (cm^{-3}s^{-1}) under 225 nm random alloy fluctuation cases in the MQW region from current densities 20 to 900 (A/cm^2).

The carrier distribution and their electron and hole wave function overlap will influence the radiative recombination distribution.[9] To put it another way, the radiative recombination in different QW will affect by the carrier-blocking ability of carriers in the active region.

Due to the shallower QWs for holes induced by strain, the carrier confinement of the

doi:10.6342/NTU202303083

hole carriers in QW will reduce. In addition, with the higher potential for holes under the n-type dopant in the first QB, the hole carrier will not overflow to the n-AlGaN layer. The maximum valance band potential in QWs is at QW 2 in the small current density case of 225 nm. Therefore, radiative recombination distribution of 225 nm with case random alloy fluctuation will dominate by the second QW (QW 2), which is closer to the n-side, at the small current density ($J \simeq 20$ (A/cm^2)) as shown in Fig. 5.17(a). By the way, because the QW 2 dominates the light emission, in the above section, the analysis of the shallower QW for holes induced by strain, we mainly discuss the valance band and the hole carrier distribution in the second QW (QW 2) to research its influence, as shown in Fig.5.13 and Fig.5.14.

At the small current density case of 225 nm, even though the hole density distribution have dominated by the n-side QW, the radiative recombination in p-side QW is still less than the n-side QW. The reason is that when considering the strain-induced deform potential, the shallower QW induced by strain will decrease the electron and hole carrier confinement in QW. Moreover, the hole density distribution dominant in QW 2, led by the maximum valance band potential in QWs at QW 2, will also influence the radiative recombination distribution.

Additionally, the radiative recombination in the p-side QW will increase at the sizeable current density ($J \simeq 900$ (A/cm^2)). The reason is that the shallower QW for holes will decrease the hole carrier-blocking ability in the quantum well region.[49, 64] The holes in QW are insufficient for the electron to recombine. The excess of the electrons will overflow and then increase the radiative recombination in the p-side QW, as shown in Fig.5.17(c). [9]

doi:10.6342/NTU202303083

5.2.3.4 EL intensity

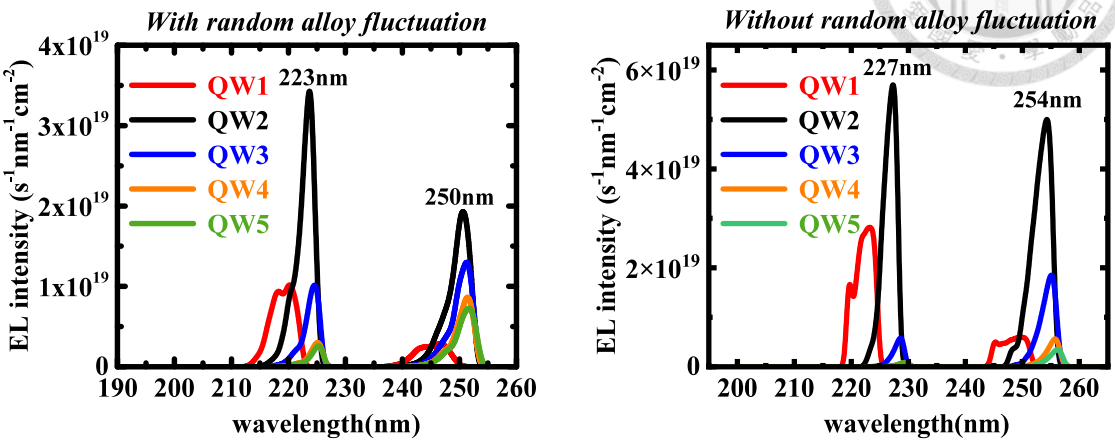

(a) with random alloy fluctuation (b) without random alloy fluctuation

Figure 5.18: (a) and (b) are the Electroluminescence (EL) intensity in different QW at current density $\simeq$ 20 (A/cm^2) under with and without random alloy fluctuation cases.

This section will analyze the EL intensity results from the k·p method influenced by the carrier carrier-blocking ability. The calculation of EL intensity includes the electron and hole wave function overlap in space and the integration of their eigenvalue, as shown in Eq. (2.96) Namely, EL intensity will influence by the carrier carrier-blocking ability. Based on the carrier distribution will be influenced by the carrier-blocking ability in the system.

Due to the difference in potential output between the strain-induced deformation potential LL model and the k·p method, their emission wavelength will also shift slightly, as shown in Fig. 3.4. Such as, for the random alloy fluctuation cases, the emission wavelength of 225 nm and 253 nm in the strain-induced deformation potential LL model will change to 223 nm and 250 nm in the k·p method.

The analysis of the EL intensity dedication by different QW in Fig. 5.18 will be afterward.

doi:10.6342/NTU202303083

Due to the shallower QWs for holes induced by the strain, the holes could cross the barrier between the quantum and the QW more easily.[49, 64] In 223 nm with random alloy fluctuation case, the improving hole carriers transport will lead to the radiative recombination dominate by the second QW (QW 2) at the current density around 20 (A/cm^2), see Fig. 5.17. Therefore the EL intensity in the second QW (QW 2) is the largest.

For III-nitride in the wurtzite structure, the crystal orientation cause in-homogeneous polarization will let the band bending.[15, 22] The strong polarization field in QW will lead to the carrier screening effect by decreasing the wave function overlap and increasing the emission wavelength. In brief, the emission wavelength will red shift by quantum Stark effect (QCSE) in the AlGaN-based UVC-LEDs.[2, 4, 16, 69] As stated above, to improve the carrier injection in this study, the p-type dopant in the first QB will distort the band structure of the first QW (QW 1). In addition, QW 1 is the one closer to the n-contact. Because the dopant in the first QB will increase the carrier density in QW 1 and screen the strong polarization field in the QW, the emission wavelength will decrease by the more flattening band structure in QW. Therefore, the spectrum of EL intensity, dedicated by MQW, would be broadened by the dedication of the QW 1 radiative recombination under the n-type dopant in the first QB.[2, 4, 16, 69]

The result shows that the emission wavelength at intensity peak from the fifth to second QW (QW 5$\sim$QW 2) will blue shift. Fig. 5.15 show that as a result of the shallower QW for holes induced by strain, the hole carrier distribution will increase from QW 5 $\sim$ QW 2 at current density $\simeq$ 20 (A/cm^2). In addition, at current density $\simeq$ 20 (A/cm^2), the electron distribution will also increase from QW 5 $\sim$ QW 2 caused by the relatively better carrier confinement efficiency for electrons in QWs. Therefore, the increased carriers in QW will screen the polarization field and decrease the emission wavelength at the intensity

doi:10.6342/NTU202303083

peak from QW 5∼QW 2.

The following is the analysis of EL intensity in QW 1. After considering the random alloy fluctuation, an EL intensity decreased obviously in the QW 1 compared to other QWs (QW 5∼QW 2) in 223 nm and 250 nm cases. Because of the n-type dopant in QB1, the depth of the QW 1 for holes is shallower than other QWs, which means that compared to other QWs, the ability of carrier confinement for holes in QW 1 is poor. Additionally, after considering the random alloy fluctuation, the ability of carrier confinement in QW 1 will further reduce due to the fluctuation potential. Consequently, the decreased EL intensity in QW 1 is significant after considering the random alloy fluctuation.

5.3 Summary

Including random alloy fluctuation in precise simulation is crucial because the without random alloy fluctuation calculation will underestimate the TM polarized light.

Random alloy fluctuation is the impact factor of carrier blocking ability due to the fluctuation potential will severe the carrier overflow and decrease the radiative recombination efficiency in the active region. In this work, due to the AlN QBs in 225 nm are not an alloy and have not fluctuated in Al composition, the carrier blocking ability is better in 225 nm. Put another way, fluctuated potential in QBs could be the critical factor leading to carrier overflow.

Strain is the impact factor of carrier blocking ability as the band structure will deform by strain. Before starting to simulate and analyze the influence of strain, this work confirms that the strain-related parameters we use are reliable first.

doi:10.6342/NTU202303083

There have two mechanisms that will deform the band structure by strain, one is the valence-band deformation potential ($D_1 \sim D_6$) that will shallower the QW for holes and larger the effective conduction band offset ratio when considering the compressive strain in a QW. The other is that the hydrostatic deformation potential (a) will change the band gap and lead to the shallower QW for electrons and holes when considering the compressive strain in a QW.

The valance band deformation might dominate the influence of strain-caused deformation potential in the system because the decrease in the valance band is larger than the increase in the conduction band when the compressive strain is in QW. Furthermore, the effective conduction band offset ratio is 0.63 without the strain-induced deformation potential case.[47, 49] Namely, the energy difference of the dominant valance band (ΔE_v) is smaller than the energy difference of the conduction band (ΔE_c) before the band structure deformation. To sum up, after considering the strain-induced deformation potential, the influence of shallower QW for holes is more severe than that of electrons.

doi:10.6342/NTU202303083

Chapter 6 Conclusion

In conclusion, Chapter 2 shows that on account of the off-diagonal terms in the k·p method, which are the response of different state interactions, and mainly dedicated by being proportional to the k square. Namely, the influence of the off-diagonal term can be seen just when the wave vector k is far away from the band gap. Hence, under the assumption of the effective mass theory, the off-diagonal terms in the k·p method can ignore and build the strain-induced deformation potential LL model.

Including the information of the strain-induced deformation potential in three bands to the traditional LL model, the calculation can transfer from the dominant band formula and its effective mass to the three formulas for CH1, CH2, and CH3 bands and their effective masses. The main difference is that the three-band formula could include more detailed information about different bands. Furthermore, the effective potential with the quantum confinement effect in the LL mode could calculate the carrier density more precisely.

In Chapter 3, this study analyzes the polarization ratio in strain-induced deformation potential LL model with and without k·p method calculation. Due to the three-band position that can be output from the strain-induced deformation potential LL model. The question will be whether the k·p method, which is used to calculate the three-band posi-

doi:10.6342/NTU202303083

tion, can remove. This work makes a comparison of the polarization trends by them. The result shows that the trend of polarization ratio is similar in the strain-induced deformation potential LL model with and without the k·p method. Hence, the simulation result of removing the k·p method is credible. Further, the calculation time can save around 47 hours per step under the simulation structure in this work.

Additionally, due to the splitting of $|Z\rangle$ and $|X \pm iY\rangle$ band in the QW regions is not the constant value, the performance of the polarization ratio value in the LL model will be average. To put it another way, the slope of the polarization ratio to wavelength is sharper in calculating the k·p method than the LL model. Moreover, in this study, because the polarization value is equal to zero at 280 nm, the light emission will change from TE to TM polarized light at 280 nm.

In Chapter 4, this work optimizes the QB and p-AlGaN layer epitaxial layer to decrease the electron carrier overflow. In optimizing the QB section, the electron carrier overflow can effectively lower by increasing the potential difference between the QW and the QB. Namely, the potential barrier will closely influence the carrier overflow. Hence, the difference of the Al composition in 0.2 is the best optimization design of the QB in this study. In the improvement hole carrier injection section, based on two reasons, one is that optimizing QB layers had improved the electron carrier overflow by increasing the carrier blocking ability of the QW in the previous work, and the other is that the shallower QW induced by strain will decrease the electron carrier overflow by improving the hole carrier transport. Due to the improvement of the hole carriers' transport, the recombination of the electron and hole carrier will increase, leading to the number of electron carriers overflowing and leaving the active region will decrease. Therefore, the p-AlGaN design with the smaller Al composition will further reduce the electron carrier overflow by the enhance

doi:10.6342/NTU202303083

the hole carrier injection from the tunneling effect, leading to better WPE performance.

In Chapter 5, this work analysis the influence of random alloy fluctuation and the strain-induced band structure deformation in UVC-LEDs. The influence of the random alloy fluctuation in the simulation show that including random alloy fluctuation in precise simulation is crucial because the calculation without considering the random alloy fluctuation will underestimate the TM polarized light by the compressive strain release in the QW region and the increase of the Al composition at the QW edge. Further, the random alloy fluctuation is the impact factor of carrier blocking ability due to the fluctuation potential will severe the carrier overflow and decrease the radiative recombination efficiency. In this work, in the simulation structure of 225 nm, the AlN QB is not an alloy and has not fluctuated in Al composition. In addition, the QW in 225 nm is still the alloy material. That is, random alloy fluctuation will influence the potential in the QW region of 225 nm. The simulation result shows that under the design of AlN QB in 225 nm, the electron current density overflow to the p-AlGaN layer is smaller than the 253 nm case due to the better carrier-blocking ability. Put another way, fluctuated potential in QB could be the critical factor leading to carrier overflow.

The strain-induced deformation potential in the simulation shows that strain is the impact factor of carrier blocking ability as the band structure will deform by strain. Before starting to simulate and analyze the influence of strain, this work confirms that the strain-related parameters we used were reliable first.

The valence-band deformation potential ($D_1 \sim D_6$) and the hydrostatic deformation potentials (a) will deform the band structure by strain. They will change the depth of the QW and the conduction band offset ratio. For the valence-band deformation potential

doi:10.6342/NTU202303083

($D_1 \sim D_6$), when considering the strain in the QW and QB is compressive and no strain, respectively, the QW for the hole will become shallower. Additionally, due to the conduction band will not influence by the valence-band deformation potential, the effective conduction band offset ratio for the band gap will become larger. For the hydrostatic deformation potentials (a), the band gap will shift and lead to the shallower QW for electrons and holes when considering the compressive strain in a QW region, but QB has no strain. However, the valance band deformation might dominate the influence of the strain-caused deformation potential in the system because the decrease in the valance band is larger and more significant than the increase in the conduction band when the compressive strain is in QW. Moreover, without the strain-induced deformation potential cases, the effective conduction band offset ratio is 0.63 .[47, 49] Namely, the energy difference of the dominant valance band (ΔE_v) is smaller than the energy difference of the conduction band (ΔE_c) before considering the band structure deformation induced by the strain. In conclusion, after considering the strain-induced deformation potential, the influence of shallower QW for holes is more severe than electrons. Therefore the carrier overflow to the QB region for holes is larger than electrons. In addition, this study evaluates the degree of the increasing hole carriers in the QB region when the strain causes shallower QW for holes. After considering the compressive strain in the QW, the hole density ratio in the QB region will change from 66% to 81% in 225 nm; the hole density ratio in the QB region will vary from 62% to 77% in 253 nm.

Due to the shallower QW for holes and the QW 2 having the highest valance band potential in the QWs region, hole carriers will mainly dominate by the QW 2. Additionally, as mentioned above, due to the higher potential for holes under the n-type dopant in the first QB, the hole carrier will not overflow to the n-AlGaN layer. Therefore, the radiative

doi:10.6342/NTU202303083

recombination of 225 nm with random alloy fluctuation case will dominate by the second QW (QW2), which is closer to the n-side, at the small current density ($J \simeq 20$ (A/cm^2)). At the sizeable current density ($J \simeq 900$ (A/cm^2)), The radiative recombination in the p-side QW will increase because the shallower QW for carriers induced by strain will decrease the carrier-blocking ability in the quantum well region. In addition, the potential barrier of the last QB is not high enough to inhibit the electron carrier overflow will also influence the radiative recombination distribution. As mentioned above, the influence of shallower QW for holes is more severe than electrons. To sum up, the holes in QW are insufficient for the electron to recombine at the large current density. The excess of the electrons will overflow the p-AlGaN layer and increase the radiative recombination in the p-side QW simultaneously.

doi:10.6342/NTU202303083

doi:10.6342/NTU202303083

References

[1] Chia-Yen Huang, Chia-Lung Tsai, Cheng-Yao Huang, Rong-Yu Yang, YewChung Sermon Wu, Hung-Wei Yen, and Yi-Keng Fu. Efficiency improvement analysis of nano-patterned sapphire substrates and semi-transparent superlattice contact layer in UVC light-emitting diodes. Applied Physics Letters, 117(26):261102, 2020.

[2] Huan-Ting Shen, Claude Weisbuch, James S. Speck, and Yuh-Renn Wu. Three-Dimensional Modeling of Minority-Carrier Lateral Diffusion Length Including Random Alloy Fluctuations in (In,Ga)N and (Al,Ga)N Single Quantum Wells. Phys. Rev. Appl., 16:024054, 2021.

[3] Hiroshi Amano et al. The 2020 UV emitter roadmap. Journal of Physics D: Applied Physics, 53(50), 2020.

[4] Kneissl M and Rass J. III-Nitride Ultraviolet Emitters—Technology and Applications. Springer Series in Materials Science, Berlin: Springer, 2016.

[5] Monika Schreiner, Javier Martínez-Abaigar, Johannes Glaab, and Marcel Jansen. UV-B Induced Secondary Plant Metabolites. Optik & Photonik, 9(2):34–37, 2014.

[6] M. Ajmal Khan, Noritoshi Maeda, Masafumi Jo, Yuki Akamatsu, Ryohei Tanabe, Yoichi Yamada, and H. Hirayama. 13 mW operation of a 295–310 nm AlGaN UV-B

doi:10.6342/NTU202303083

LED with a p-AlGaN transparent contact layer for real world applications. Journal of Materials Chemistry C, 7:143–152, 2018.

[7] Hideki Hirayama, Noritoshi Maeda, Sachie Fujikawa, Shiro Toyoda, and Norihiko Kamata. Recent progress and future prospects of AlGaN-based high-efficiency deep-ultraviolet light-emitting diodes. Japanese Journal of Applied Physics, 53(10):100209, 2014.

[8] M Hessling, R Haag, N Sieber, and P Vatter. The impact of far-UVC radiation (200–230 nm) on pathogens, cells, skin, and eyes –a collection and analysis of a hundred years of data. MS Hygiene and Infection Control, 16, 2021.

[9] Hung-Hsiang Chen, James S. Speck, Claude Weisbuch, and Yuh-Renn Wu. Three dimensional simulation on the transport and quantum efficiency of UVC-LEDs with random alloy fluctuations. Applied Physics Letters, 113(15):153504, 2018.

[10] Yongfei Chen, Jiamang Che, Chunshuang Chu, Hua Shao, Yonghui Zhang, and Zi-Hui Zhang. Balanced Resistivity in n-AlGaN Layer to Increase the Current Uniformity for AlGaN-Based DUV LEDs. IEEE Photonics Technology Letters, 34(20):1065–1068, 2022.

[11] Christian Kuhn, Luca Sulmoni, Martin Guttmann, Johannes Glaab, Norman Susilo, Tim Wernicke, Markus Weyers, and Michael Kneissl. MOVPE-grown AlGaN-based tunnel heterojunctions enabling fully transparent UVC LEDs. Photonics Research, 7(5):B7–B11, 2019.

[12] Tien-Yu Wang, Wei-Chi Lai, Syuan-Yu Sie, Sheng-Po Chang, Yuh-Renn Wu, Yu-Zung Chiou, Cheng-Huang Kuo, and Jinn-Kong Sheu. AlGaN-based deep ultravi-

doi:10.6342/NTU202303083

olet light emitting diodes with magnesium delta-doped AlGaN last barrier. Applied Physics Letters, 117:251101, 2020.

[13] Dong Liu, Sang June Cho, Jeongpil Park, Jiarui Gong, Jung-Hun Seo, Rafael Dalmau, Deyin Zhao, Kwangeun Kim, Munho Kim, Akhil R. K. Kalapala, John D. Albrecht, Weidong Zhou, Baxter Moody, and Zhenqiang Ma. 226 nm AlGaN/AlN UV LEDs using p-type Si for hole injection and UV reflection. Applied Physics Letters, 113(1), 2018.

[14] Yuanwen Zhang, Lei Yu, Kai Li, Hui Pi, Jiasheng Diao, Xingfu Wang, Yue Shen, Chongzhen Zhang, Wenxiao Hu, Weidong Song, and Shuti Li. The improvement of deep-ultraviolet light-emitting diodes with gradually decreasing Al content in AlGaN electron blocking layers. Superlattices and Microstructures, 82:151–157, 2015.

[15] Seoung-Hwan Park and Shun-Lien Chuang. Crystal-orientation effects on the piezoelectric field and electronic properties of strained wurtzite semiconductors. Phys. Rev. B, 59:4725–4737, 1999.

[16] Seoung-Hwan Park and Shun-Lien Chuang. Piezoelectric effects on electrical and optical properties of wurtzite GaN/AlGaN quantum well lasers. Applied Physics Letters, 72(24):3103–3105, 1998.

[17] Seoung-Hwan Park and Shun-Lien Chuang. Comparison of zinc-blende and wurtzite GaN semiconductors with spontaneous polarization and piezoelectric field effects. Journal of Applied Physics, 87(1):353–364, 2000.

[18] Dong Yeong Kim, Jun Hyuk Park, Jong Won Lee, Sunyong Hwang, Seung Jae Oh, Jungsub Kim, Cheolsoo Sone, E Fred Schubert, and Jong Kyu Kim. Overcoming the fundamental light-extraction efficiency limitations of deep ultraviolet light-

doi:10.6342/NTU202303083

emitting diodes by utilizing transverse-magnetic-dominant emission. Light: Science & Applications, 4(4):e263–e263, 2015.

[19] Weiying Wang, Huimin Lu, Lei Fu, Chenguang He, Mingxing Wang, Ning Tang, Fujun Xu, Tongjun Yu, Weikun Ge, and Bo Shen. Enhancement of optical polarization degree of AlGaN quantum wells by using staggered structure. Opt. Express, 24(16):18176–18183, 2016.

[20] Hideo Kawanishi, Masanori Senuma, Mao Yamamoto, Eiichiro Niikura, and Takeaki Nukui. Extremely weak surface emission from (0001) c-plane AlGaN multiple quantum well structure in deep-ultraviolet spectral region. Applied Physics Letters, 89(8):081121, 2006.

[21] X. J. Chen, T. J. Yu, H. M. Lu, G. C. Yuan, B. Shen, and G. Y. Zhang. Modulating optical polarization properties of Al-rich AlGaN/AlN quantum well by controlling wavefunction overlap. Applied Physics Letters, 103(18):181117, 2013.

[22] M. Kumagai, S. L. Chuang, and H. Ando. Analytical solutions of the block-diagonalized Hamiltonian for strained wurtzite semiconductors. Phys. Rev. B, 57:15303–15314, 1998.

[23] Huan-Ting Shen, Yu-Chieh Chang, and Yuh-Renn Wu. Analysis of Light-Emission Polarization Ratio in Deep-Ultraviolet Light-Emitting Diodes by Considering Random Alloy Fluctuations with the 3D k·p Method. physica status solidi (RRL) –Rapid Research Letters, 16(2):2100498, 2022.

[24] Frank Mehnke, Christian Kuhn, Martin Guttmann, Christoph Reich, Tim Kolbe, Viola Kueller, Arne Knauer, Mickael Lapeyrade, Sven Einfeldt, Jens Rass, Tim Wernicke, Markus Weyers, and Michael Kneissl. Efficient charge carrier injection into

doi:10.6342/NTU202303083

sub-250 nm AlGaN multiple quantum well light emitting diodes. Applied Physics Letters, 105(5):051113, 2014.

[25] Akira Yoshikawa, Ryosuke Hasegawa, Tomohiro Morishita, Kazuhiro Nagase, Satoshi Yamada, James Grandusky, Jonathan Mann, Amy Miller, and Leo J. Schowalter. Improve efficiency and long lifetime UVC LEDs with wavelengths between 230 and 237 nm. Applied Physics Express, 13(2):022001, 2020.

[26] Craig G. Moe, Sho Sugiyama, Jumpei Kasai, James R. Grandusky, and Leo J. Schowalter. AlGaN Light-Emitting Diodes on AlN Substrates Emitting at 230 nm. physica status solidi (a), 215(10):1700660, 2018.

[27] A. Bhattacharyya, T. D. Moustakas, Lin Zhou, David. J. Smith, and W. Hug. Deep ultraviolet emitting AlGaN quantum wells with high internal quantum efficiency. Applied Physics Letters, 94(18):181907, 2009.

[28] Emanuele Francesco Pecora, Wei Zhang, A. Yu. Nikiforov, Lin Zhou, David J. Smith, Jian Yin, Roberto Paiella, Luca Dal Negro, and T. D. Moustakas. Sub-250 nm room-temperature optical gain from AlGaN/AlN multiple quantum wells with strong band-structure potential fluctuations. Applied Physics Letters, 100(6):061111, 2012.

[29] Tsung-Jui Yang, Ravi Shivaraman, James S. Speck, and Yuh-Renn Wu. The influence of random indium alloy fluctuations in indium gallium nitride quantum wells on the device behavior. Journal of Applied Physics, 116(11):113104, 2014.

[30] Chen-Kuo Wu, Chi-Kang Li, and Yuh-Renn Wu. Percolation transport study in nitride based LED by considering the random alloy fluctuation. Journal of Computational Electronics, 14(2):416–424, 2015.

doi:10.6342/NTU202303083

[31] D. D. Nolte, W. Walukiewicz, and E. E. Haller. Band-edge hydrostatic deformation potentials in III-V semiconductors. Phys. Rev. Lett., 59:501–504, 1987.

[32] Zhigang Shuai, Linjun Wang, and Chenchen Song. Deformation Potential Theory, pages 67–88. Springer Berlin Heidelberg, Berlin, Heidelberg, 2012.

[33] Christophe Geuzaine and Jean-François Remacle. Gmsh: A 3-D Finite Element Mesh Generator with built-in Pre- and Post-Processing Facilities. International Journal for Numerical Methods in Engineering, 79(11):1309–1331, 2009.

[34] M. Sabathil, A. Laubsch, and N. Linder. Self-consistent modeling of resonant PL in InGaN SQW LED-structure. In Klaus P. Streubel and Heonsu Jeon, editors, Light-Emitting Diodes: Research, Manufacturing, and Applications XI, volume 6486, page 64860V. International Society for Optics and Photonics, SPIE, 2007.

[35] S. L. Chuang and C. S. Chang. k.p method for strained wurtzite semiconductors. Physical Review B, 54(4):2491–2504, 1996. PRB.

[36] Seoung-Hwan Park, Doyeol Ahn, and Shun-Lien Chuang. Electronic and Optical Properties of a- and m-Plane Wurtzite InGaN–GaN Quantum Wells. IEEE Journal of Quantum Electronics, 43(12):1175–1182, 2007.

[37] I. Vurgaftman and J. R. Meyer. Band parameters for nitrogen-containing semiconductors. Journal of Applied Physics, 94(6):3675–3696, 2003.

[38] Tsukuru Ohtoshi, Atsuko Niwa Atsuko Niwa, and Takao Kuroda Takao Kuroda. Crystal Orientation Effect on Valence-Subband Structures in Wurtzite-GaN Strained Quantum Wells. Japanese Journal of Applied Physics, 35(12A):L1566, 1996.

doi:10.6342/NTU202303083

[39] I. Vurgaftman, J. R. Meyer, and L. R. Ram-Mohan. Band parameters for III–V compound semiconductors and their alloys. Journal of Applied Physics, 89(11):5815–5875, 2001.

[40] Marco Piccardo, Chi-Kang Li, Yuh-Renn Wu, James S. Speck, Bastien Bonef, Robert M. Farrell, Marcel Filoche, Lucio Martinelli, Jacques Peretti, and Claude Weisbuch. Localization landscape theory of disorder in semiconductors. II. Urbach tails of disordered quantum well layers. Physical Review B, 95(14), 2017.

[41] Chi-Kang Li, Marco Piccardo, Li-Shuo Lu, Svitlana Mayboroda, Lucio Martinelli, Jacques Peretti, James S. Speck, Claude Weisbuch, Marcel Filoche, and Yuh-Renn Wu. Localization landscape theory of disorder in semiconductors. III. Application to carrier transport and recombination in light emitting diodes. Physical Review B, 95(14), 2017.

[42] Miguel A. Caro, Stefan Schulz, and Eoin P. O'Reilly. Theory of local electric polarization and its relation to internal strain: Impact on polarization potential and electronic properties of group-III nitrides. Phys. Rev. B, 88:214103, 2013.

[43] Emanuele Francesco Pecora, Wei Zhang, A. Yu. Nikiforov, Lin Zhou, David J. Smith, Jian Yin, Roberto Paiella, Luca Dal Negro, and T. D. Moustakas. Sub-250 nm room-temperature optical gain from AlGaN/AlN multiple quantum wells with strong band-structure potential fluctuations. Applied Physics Letters, 100(6):061111, 2012.

[44] Claude Weisbuch, Shuji Nakamura, Yuh-Renn Wu, and James S. Speck. Disorder effects in nitride semiconductors: impact on fundamental and device properties. Nanophotonics, 10(1):3–21, 2020.

[45] A. E. Romanov, T. J. Baker, S. Nakamura, J. S. Speck, and ERATO/JST UCSB

doi:10.6342/NTU202303083

Group. Strain-induced polarization in wurtzite III-nitride semipolar layers. Journal of Applied Physics, 100(2):023522, 2006.

[46] D. N. Arnold, G. David, D. Jerison, S. Mayboroda, and M. Filoche. Effective Confining Potential of Quantum States in Disordered Media. Phys Rev Lett, 116(5):056602, 2016.

[47] Marcel Filoche, Marco Piccardo, Yuh-Renn Wu, Chi-Kang Li, Claude Weisbuch, and Svitlana Mayboroda. Localization landscape theory of disorder in semiconductors. I. Theory and modeling. Physical Review B, 95(14), 2017.

[48] Sh Park, D. Ahn, and Shun-Lien Chuang. Electronic and Optical Properties of a- and m-Plane Wurtzite InGaN–GaN Quantum Wells. Quantum Electronics, IEEE Journal of, 43:1175 – 1182, 2008.

[49] Jih-Yuan Chang, Hui-Tzu Chang, Ya-Hsuan Shih, Fang-Ming Chen, Man-Fang Huang, and Yen-Kuang Kuo. Efficient Carrier Confinement in Deep-Ultraviolet Light-Emitting Diodes With Composition-Graded Configuration. IEEE Transactions on Electron Devices, 64(12):4980–4984, 2017.

[50] A.P. Kirk. Solar Photovoltaic Cells: Photons to Electricity. Elsevier Science, 2014.

[51] Thierry Goudon, Vera Miljanović, and Christian Schmeiser. On the Shockley–Read–Hall Model: Generation-Recombination in Semiconductors. SIAM Journal on Applied Mathematics, 67(4):1183–1201, 2007.

[52] Jasprit Singh. Electronic and Optoelectronic Properties of Semiconductor Structures. Electronic and Optoelectronic Properties of Semiconductor Structures, by Jasprit Singh, pp. 554. ISBN 052182379X. Cambridge, UK: Cambridge University Press, February 2003., 2003.

doi:10.6342/NTU202303083

[53] Lin Guan-Bo, Kim Dong-Yeong, Shan Qifeng, Cho Jaehee, E. Fred Schubert, Shim Hyunwook, Sone Cheolsoo, and Kim Jong Kyu. Effect of Quantum Barrier Thickness in the Multiple-Quantum-Well Active Region of GaInN/GaN Light-Emitting Diodes. IEEE Photonics Journal, 5(4):1600207–1600207, 2013.

[54] C. J. Sun, P. Kung, A. Saxler, H. Ohsato, K. Haritos, and M. Razeghi. A crystallographic model of (00·1) aluminum nitride epitaxial thin film growth on (00·1) sapphire substrate. Journal of Applied Physics, 75(8):3964–3967, 1994.

[55] Hideki Hirayama, Norimichi Noguchi, Tohru Yatabe, and Norihiko Kamata. 227 nm AlGaN Light-Emitting Diode with 0.15 mW Output Power Realized using a Thin Quantum Well and AlN Buffer with Reduced Threading Dislocation Density. Applied Physics Express, 1(5):051101, 2008.

[56] Jan Ruschel, Johannes Glaab, Norman Susilo, Sylvia Hagedorn, Sebastian Walde, Eviathar Ziffer, Hyun Kyong Cho, Neysha Lobo Ploch, Tim Wernicke, Markus Weyers, Sven Einfeldt, and Michael Kneissl. Reliability of UVC LEDs fabricated on AlN/sapphire templates with different threading dislocation densities. Applied Physics Letters, 117(24):241104, 2020.

[57] Norman Susilo, Eviathar Ziffer, Sylvia Hagedorn, Leonardo Cancellara, Carsten Netzel, Neysha Lobo Ploch, Shaojun Wu, Jens Rass, Sebastian Walde, Luca Sulmoni, Martin Guttmann, Tim Wernicke, Martin Albrecht, Markus Weyers, and Michael Kneissl. Improved performance of UVC-LEDs by combination of high-temperature annealing and epitaxially laterally overgrown AlN/sapphire. Photon. Res., 8(4):589–594, 2020.

[58] M. L. Nakarmi, N. Nepal, C. Ugolini, T. M. Altahtamouni, J. Y. Lin, and H. X. Jiang.

doi:10.6342/NTU202303083

Correlation between optical and electrical properties of Mg-doped AlN epilayers. Applied Physics Letters, 89(15):152120, 2006.

[59] Toru Kinoshita, Toshiyuki Obata, Hiroyuki Yanagi, Shin Inoue, and ichiro. High p-type conduction in high-Al content Mg-doped AlGaN. Applied Physics Letters, 102(1):012105, 2013.

[60] M. L. Nakarmi, N. Nepal, J. Y. Lin, and H. X. Jiang. Photoluminescence studies of impurity transitions in Mg-doped AlGaN alloys. Applied Physics Letters, 94(9):091903, 2009.

[61] Yuh-Renn Wu, Ravi Shivaraman, Kuang-Chung Wang, and James S. Speck. Analyzing the physical properties of InGaN multiple quantum well light emitting diodes from nano scale structure. Applied Physics Letters, 101(8):083505, 2012.

[62] Asif Khan, Krishnan Balakrishnan, and Tom Katona. Ultraviolet light-emitting diodes based on group three nitrides. Nature Photonics, 2(2):77–84, 2008.

[63] A Fujioka, K Asada, H Yamada, T Ohtsuka, T Ogawa, T Kosugi, D Kishikawa, and T Mukai. High-output-power 255/280/310 nm deep ultraviolet light-emitting diodes and their lifetime characteristics. Semiconductor Science and Technology, 29(8):084005, 2014.

[64] Jih-Yuan Chang, Bo-Ting Liou, Man-Fang Huang, Ya-Hsuan Shih, Fang-Ming Chen, and Yen-Kuang Kuo. High-Efficiency Deep-Ultraviolet Light-Emitting Diodes With Efficient Carrier Confinement and High Light Extraction. IEEE Transactions on Electron Devices, 66(2):976–982, 2019.

[65] O. Ambacher, J. Smart, J. R. Shealy, N. G. Weimann, K. Chu, M. Murphy, W. J. Schaff, L. F. Eastman, R. Dimitrov, L. Wittmer, M. Stutzmann, W. Rieger, and

doi:10.6342/NTU202303083

J. Hilsenbeck. Two-dimensional electron gases induced by spontaneous and piezo-electric polarization charges in N- and Ga-face AlGaN/GaN heterostructures. Journal of Applied Physics, 85(6):3222–3233, 1999.

[66] Jeonghyun Hwang, William Schaff, Lester Eastman, Shawn Bradley, Leonard Brillson, David Look, Jiong Wu, Wladek Walukiewicz, M. Furis, and Alexander Cartwright. Si doping of high-Al-mole fraction AlxGa1−xN alloys with rf plasma-induced molecular-beam-epitaxy. Applied Physics Letters, 81:5192–5194, 2002.

[67] Xinhui Chen, Kuan-Ying Ho, and Yuh-Renn Wu. Modeling and optimization of p-AlGaN super lattice structure as the p-contact and transparent layer in AlGaN UVLEDs. Opt. Express, 23(25):32367–32376, 2015.

[68] Shin-ichiro Inoue, Tamari Naoki, Toru Kinoshita, Toshiyuki Obata, and Hiroyuki Yanagi. Light extraction enhancement of 265 nm deep-ultraviolet light-emitting diodes with over 90 mW output power via an AlN hybrid nanostructure. Applied Physics Letters, 106(13):131104, 2015.

[69] Yuh-Renn Wu, Yih-Yin Lin, Hung-Hsun Huang, and Jasprit Singh. Electronic and optical properties of InGaN quantum dot based light emitters for solid state lighting. Journal of Applied Physics, 105(1):013117, 2009.

doi:10.6342/NTU202303083